6-2023

Thermal, Magnetic, and Electrical Properties of Thin Films and Nanostructures: From Magnetic Insulators to Organic Thermoelectrics

Michael J. M. Roos

Thermal, Magnetic, and Electrical Properties of Thin Films and Nanostructures: From Magnetic Insulators to Organic Thermoelectrics

Abstract

Modern fabrication and growth techniques allow for the development of increasingly smaller and more complex solid state structures, the characterization of which require highly specialized measurement platforms. In this dissertation I present the development of techniques and instrumentation used in magnetic, thermal, and electrical property measurements of thin films and nanostructures. The understanding of trapped-flux induced artifacts in SQUID magnetometry of large paramagnetic substrates allows for the resolution of increasingly small moments. Using these methods, the antiferromagnetic coupling of the interface between a $Y_3Fe_5O_{12}$ film and $Gd_3Ga_5O_{12}$substrate is quantitatively characterized, along with a number of other thin films. The use of custom fabricated silicon-nitride membrane thermal isolation platforms for temperature-dependent measurements is then presented for in-plane thermal conductivity, electrical conductivity, and thermopower of thin films. The size- and temperature-dependent properties of two types of semiconducting single-walled carbon nanotube thin films deposited and measured on these platforms reveal differing phonon contributions to thermal conductivity, and the interaction of dopant molecules and phonon transport in the disordered nanotube networks is explored. Experimental techniques for studying freestanding nanotube films is then presented, revealing a largely phonon-driven thermal conductivity that is greatly decreased by the introduction of phonon scattering sites. Next, time-dependent measurements on the suspended micromachined platforms was developed to allow for thermal detection of tiny depositions of energy from chemical reactions or physical processes in nanoscale systems. These experiments show our platforms have promise for open-chamber calorimetry of viral detection, and were expanded to include heat capacity into our suite of precision in-situ thermal measurements. Finally, copper thin films fabricated for heat capacity calibration are characterized and show a sharp reduction in thermal conductivity that 'violates' the Wiedemann-Franz law.

Document Type

Dissertation

Degree Name

Ph.D.

First Advisor

Barry L. Zink

Second Advisor

Brian W. Michel

Third Advisor

Mark E. Siemens

Keywords

Carbon nanotube, Characterization, Magnetic materials, Magnetism, Microcalorimetry, Wiedemann-Franz violation

Subject Categories

Condensed Matter Physics | Materials Science and Engineering | Physical Sciences and Mathematics |

Physics | Semiconductor and Optical Materials

Thermal, Magnetic, and Electrical Properties of Thin Films and Nanostructures: From Magnetic Insulators to Organic Thermoelectrics

A Dissertation

Presented to

the Faculty of the College of Natural Sciences and Mathematics

University of Denver

In Partial Fulfillment

of the Requirements for the Degree

Doctor of Philosophy

by

Michael J. M. Roos

June 2023

Advisor: Barry L. Zink

Author: Michael J. M. Roos
Title: Thermal, Magnetic, and Electrical Properties of Thin Films and Nanostructures: From Magnetic Insulators to Organic Thermoelectrics
Advisor: Barry L. Zink
Degree Date: June 2023

Abstract

Modern fabrication and growth techniques allow for the development of increasingly smaller and more complex solid state structures, the characterization of which require highly specialized measurement platforms. In this dissertation I present the development of techniques and instrumentation used in magnetic, thermal, and electrical property measurements of thin films and nanostructures. The understanding of trapped-flux induced artifacts in SQUID magnetometry of large paramagnetic substrates allows for the resolution of increasingly small moments. Using these methods, the antiferromagnetic coupling of the interface between a $Y_3Fe_5O_{12}$ film and $Gd_3Ga_5O_{12}$ substrate is quantitatively characterized, along with a number of other thin films. The use of custom fabricated silicon-nitride membrane thermal isolation platforms for temperature-dependent measurements is then presented for in-plane thermal conductivity, electrical conductivity, and thermopower of thin films. The size- and temperature-dependent properties of two types of semiconducting single-walled carbon nanotube thin films deposited and measured on these platforms reveal differing phonon contributions to thermal conductivity, and the interaction of dopant molecules and phonon transport in the disordered nanotube networks is explored. Experimental techniques for studying freestanding nanotube films is then presented, revealing a largely phonon-driven thermal conductivity that is greatly decreased by the introduction of phonon scattering sites. Next, time-

dependent measurements on the suspended micromachined platforms was developed to allow for thermal detection of tiny depositions of energy from chemical reactions or physical processes in nanoscale systems. These experiments show our platforms have promise for open-chamber calorimetry of viral detection, and were expanded to include heat capacity into our suite of precision *in-situ* thermal measurements. Finally, copper thin films fabricated for heat capacity calibration are characterized and show a sharp reduction in thermal conductivity that 'violates' the Wiedemann-Franz law.

Acknowledgements

Just under ten years and two months ago, at age 26, I received my GED. Today I submit my dissertation for Doctor of Philosophy in Physics. You can't make a journey like that alone. The giants whose shoulders I stand upon in order to be where I am today are innumerable to count. In no particular order, I want acknowledge a few such giants, to whom I am forever grateful. Jim Dove and Martin Huber are two of many professors during my undergrad that solidified my passion for physics. Azure Avery inspired me to dream bigger, and Jeffrey Blackburn and Andrew Ferguson showed me a world I didn't know existed. Devin Wesenberg took me under his wing when I started at DU, and Matt Natale, Sam Bleser, and Leo Hernandez helped keep me sane, put up with me hogging instruments, and kept me curious and inspired. To every professor at DU that guided me along the way, Mark Siemens, Davor Balzar, Xin Fan, Brian Michel, Gareth and Sandra Eaton, and so many more, thank you. Jasmine Andersen and Noah de Leeuw, I don't know if I could have done it without you. Faun Lee, I absolutely know I couldn't have done it without you. Jacaranda Palmateer and everyone in Health and Counseling, I learned more about myself these past years with your help than I could have ever imagined. And to my advisor, Barry Zink, who brought me into a tinkerer's dream lab and let me stretch my instrumentalist wings. I cannot express enough how thankful I am for your support, understanding, and knowledge. Finally, to all of my friends and family, whose unyielding support truly was the scaffolding allowing me to build the life I now have, I am so thankful for you. I can hardly believe all that I have accomplished, and I know I only could have done it because you were at my side.

Table of Contents

List of Figures

Chapter 1

Introduction

The most challenging part of my doctoral work turned out to be limiting the number of things I attempted to study. This dissertation includes a series of chapters, each containing its own introduction, experimental section, and discussion of results. I have done my best to arrange them in the most sensible manner; however, if you were to only read the first and last chapters, you might think that you had read two entirely different dissertations.

Current technology allows us to fabricate increasingly complex and amazing orientations of what are essentially just a few building blocks. At a basic level, there are electrons bound or unbound to nuclear potential wells consisting of protons and neutrons of varying amounts. These all have quantum mechanical properties called charge and spin, among others. Simply put, the interactions and movement of these particles in systems classically thought of as stationary is the foundation of modern society. However, there are an infinite number of ways to arrange these simple building blocks. Most of these arrangements are quite unspectacular, but over the years researchers have found some that do incredible things in surprising ways. While mankind has always looked up at the stars with curiosity, our species has only recently become fascinated with looking down and uncovering the possibilities of these special arrangements. And as fabrication techniques improve and our

tools become more advanced, our understanding of the physical universe expands and creates exciting opportunities to reveal new ways interactions can occur. The chapters of this dissertation are a series of experiments that explore just few of these possible arrangements.

A large component of what was studied involved the magnetic structure of unique materials. Using powerful characterization techniques, hundreds of samples and thousands of measurements were taken to reveal how these special arrangements interact to produce the amazing effects that drive our curiosity as scientists. The first chapter covers the use of commercial magnetometry tools to explore some of the smallest collections of magnetic moments. The second chapter highlights an extremely detailed quantitative exploration of the interface between one of these thin films and the substrate it was grown on. Additional magnetic materials characterized are highlighted in Chapter 4. However, they represent only the more conclusive results that were able to be tied up with a nice bow. Not represented here are the hundreds of measurements on numerous samples from simple cotton-filled capsules to superconducting cuprates.

A pivot follows in chapter five as I explored another side of my research in thermal, electric, and thermoelectric transport in thin films. This chapter is a detailed exploration into transport properties in one of the most exciting recent arrangements of carbon, one the most important atoms to organic life. Specialized thermal isolation platforms for measurements of thin film transport properties were used to probe systems of highly enriched semiconducting single-walled carbon nanotubes. These highly-specialized measurement techniques were adapted for measurements of these nanotube films in thicknesses slightly above 'thin,' where they can be independently freestanding. Unique experimental methods are highlighted and open

the door to a promising collaborative investigation. Then, temporal measurements on these thermal platforms show their exceptional sensitivity and adaptability via experiments in open environmental conditions. These results show promise for adapting these suspended membrane nanocalorimeters in biological reaction experiments. The foray into time-resolution continues in the following chapter in an in-depth exploration of incorporating specific heat nanocalorimetry to our current suite of *in-situ* precision thermal and electrical measurements. Finally, the last chapter reveals intriguing results on unique transport properties in thin copper films.

Chapter 2

Trapped-Flux Induced Artifacts in SQUID Magnetometry of Large Paramagnetic Substrates

2.1 Introduction

Modern fabrication and growth techniques allow for condensed matter physics and material science research to develop increasingly smaller and complex solid state structures. Advances in manufacturing techniques for quantum heterostructures, ultra-thin films, and nanoparticles have increased the need for quality characterization techniques. Sensitive magnetometry is one such tool used to reveal magnetic order and dynamics in samples of increasingly smaller dimensions. Superconducting quantum interference device (SQUID) magnetometers have become ubiquitous in sensitive magnetic characterization due to high sensitivity and general user friendliness. Commercial SQUID magnetometers are often the instruments used in magnetic property studies claiming novel and remarkable results. It is therefore of great importance that the individual components that produce a SQUID magnetometer's final output signal are properly understood.

The most commonly used commercial SQUID magnetometers, capable of fields up to 7 T, do not directly measure magnetic fields produced by the instrument, nor the magnetic moment of measured samples [1]. Instead, they measure the current

in the superconducting coils by comparing a voltage drop across shunt resistors in the power supply. A sample's magnetic moment is calculated by moving it through the superconducting coils and measuring the induced current in a second order gradiometer, creating a position dependent voltage. The resulting SQUID response voltage is fit to an ideal dipole model to produce the reported magnetic moment value. Deviations from an ideal dipole due to sample geometry [2], positioning in the gradiometer, demagnetizing factors [3], and the accuracy of the magnetic field impact the accuracy of the reported moment.

The material of the SQUID magnetometer's solenoid winding is a type-2 superconductor that, when sufficiently large magnetic fields are applied, trap magnetic flux in the form of pinned vortices localized along defect states in the winding material. The density of these pinned magnetic flux lines is proportional to the field strength induced by current in the stacked solenoid, and persists when the current is removed. This leads to magnetic remanence and flux creep [4] that can escape into the solenoid bore causing an induced current in the windings. Due to the nature of how the SQUID magnetometer measures field values, this trapped flux can cause significant deviations between the field value reported by the magnetometer software and the magnetic field actually present at the position of the sample. Heating the coils above their critical temperature is a standard practice for removing this trapped flux in the magnet, but we show that any applied current in superconducting windings will cause some amount of trapped flux during a measurement.

Current is controlled by comparing the amplified voltage produced by dropping the magnet current across a shunt resistor to the electronics control board voltage. The difference in these voltages drives the power supply output to set the intended field values via a precise voltage-to-field calibration. When current in the mag-

net is driven by the power supply a persistent switch is heated to a resistive state, that when cooled to superconducting allows the persistent current in the magnet. The power supply providing the current must be well-calibrated, as discrepancies in its amplifier or current reversal offset cause deviations in the current driven by the power supply from the actual current present in the superconducting solenoid. These issues can compound with the self-correcting routines meant to maintain accuracy in the current supplied to the magnet, and can instead lead to larger deviations over time and must also be corrected by resetting the power supply [5].

As SQUID magnetometry is a measurement of the entire volume surrounded by the gradiometer coils, any impurities or defects introduced either in the sample manufacturing process or during any subsequent handling can create non-insignificant contributions to the final signal if not accounted for. Proper handling, mounting, and sample geometry are important considerations for maximizing signal fidelity, and are well documented elsewhere. [5–8] In field-dependent measurements, determining correct field values is of the highest importance. Being an indirect measurement which reports the total aggregate of signals produced within the entire sample space the resulting data is a superposition of numerous magnetic states. For ultrathin magnetic materials on proportionally massive paramagnetic or diamagnetic substrates deviations in correct field values can cause a range of artifacts when attempting to isolate small individual components from large backgrounds.

One such magnetic material, yttrium iron garnet, $Y_3Fe_5O_{12}$ (YIG), is a wide band-gap (2.8 eV) ferrimagnet, although for most temperatures and fields YIG looks like a simple ferromagnet up to a Curie temperature of 560 K. With exceptionally low Gilbert damping, high microwave quality factor, and optical and infared transparency, it has important technological applications in RF and microwave en-

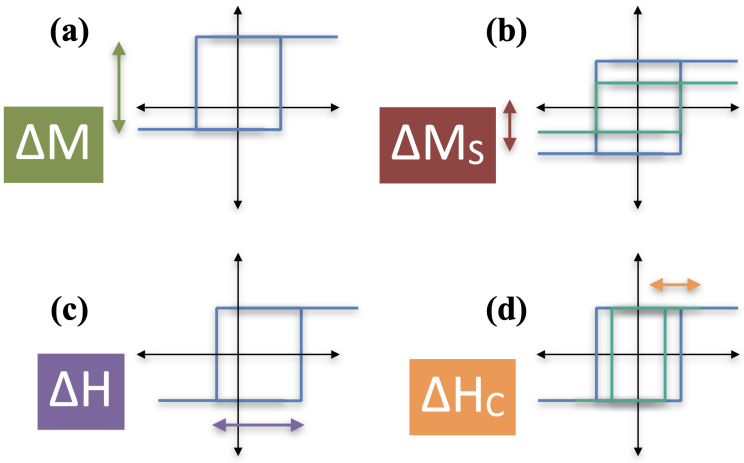

Figure 2.1: **a)** Vertical shifting can be caused by either linear or direct subtractions with differing field histories. **b)** Horizontal shifts from larger remnant fields than are produced in the measurement. **c)** Saturation magnetization shifting from both trapped flux and signal aberrations. **d)** Coercivity shift due to not correcting the field with a palladium reference standard.

gineering [9, 10]. In recent years YIG has become nearly ubiquitous in spintronics, where it is commonly used as a spin source (via spin pumping [11–16] and/or the longitudinal spin Seebeck effects [17–21]), or as a magnon spin current channel [22–28]. Though some applications and investigations use bulk YIG in very high-quality single crystals, many focus on films of various thickness grown by liquid phase epitaxy, pulsed laser deposition, or sputtering [29]. These include microwave delay lines, auto-oscillators, and magnonic crystals [30–34].

The best available substrate for YIG thin film growth is gadolinium gallium garnet, $Gd_3Ga_5O_{12}$ (GGG), due to exceptional lattice matching ($a_{YIG} = 1.2373$ nm and $a_{GGG} = 1.2383$ nm) and expected disordered magnetic structure. GGG is a geometrically frustrated Heiseneberg magnet with a Curie-Weiss temperature near -2 K. With a spin glass transition below 0.4 K, GGG has no magnetic ordering

at higher temperatures and is often considered a simple paramagnet with linear susceptibility in most laboratory-used sizes and magnetic field strengths [35].

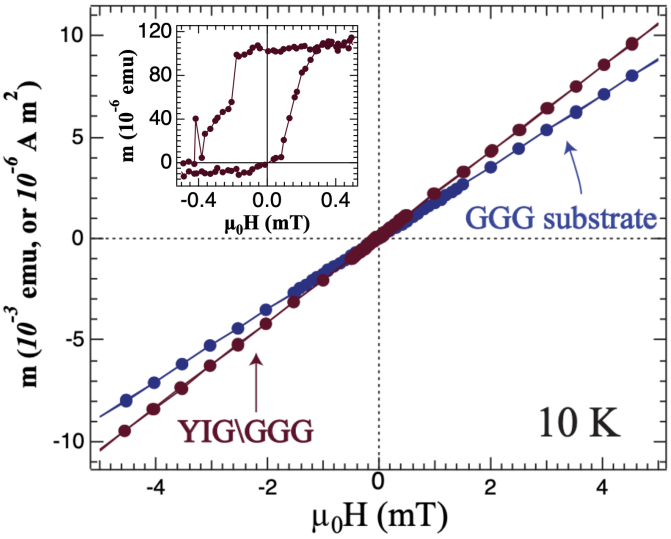

Figure 2.2: Comparison of a GGG substrate (blue) to 20nm YIG thin film grown on GGG (red). The YIG signal is only resolvable by removing the dominating GGG signal. (inset) The bare GGG substrate's slightly smaller mass causes the difference in slope, which must be accounted for in a direct background subtraction.

When measuring small samples grown on comparatively massive paramagnetic or diamagnetic substrates, the sensitivity of the SQUID magnetometer and design restrictions can introduce artifacts. To isolate the sample's magnetic moment the dominating substrate signal must carefully be subtracted off. A common assumption is that such substrates have a perfectly linear background which can be removed by subtracting a linear fit to data above saturation. Subtracting this linear component in these situations does not account for the artifacts, and may be mistaken for novel or exciting results. For an ultra-thin YIG film grown on GGG, the YIG the hysteretic YIG magnetization is tiny compared to the background (Figure 2.2). Assuming the GGG background is linear does not account for deviations

due to trapped flux that causes a vertical shift (Fig. 2.2 inset) or remnant field. In Figure 2.3 the raw GGG moment appears linear, but at low fields (inset) trapped flux causes a splitting that is magnified by a subtraction of a linear fit (Fig. 2.3b). This results in an artifact appearing as large negative remanence in the paramagnetic GGG substrate. Isolating thin films via a linear subtraction causes significant hysteresis modification when this apparent remanence is comparable to the small sample's moment. In this way, trapped flux can have disproportional impact on the resulting signal in a way that is proportional to the susceptibility and size of the substrate. Other artifacts manifest as vertical or horizontal exchange bias, and increases or decreases in saturation and coercivity (Fig. 2.1).

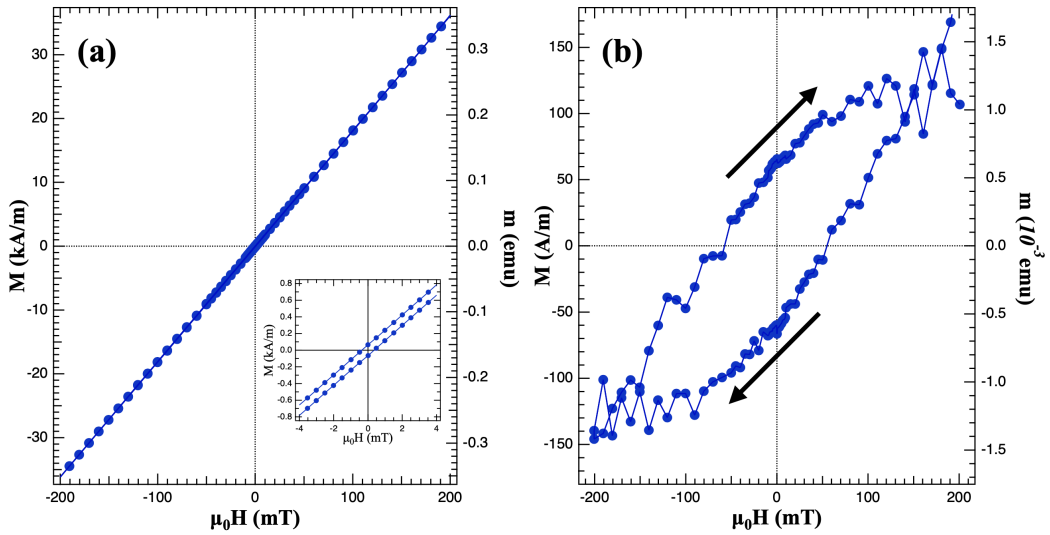

Figure 2.3: Magnetization vs field on a GGG substrate. A large paramagnetic susceptibility **(a)** shows significant deviation from linearity at low field (inset). **b** Removing the linear component reveals an apparent negative remanence, an artifact produced by a deviation in the reported field value from the actual field acting on the sample.

Temperature dependent hysteresis loops taken with differing field conditions illustrate the importance of directly measuring the substrate background for proper

subtraction from the bulk aggregate signal. Further details are then shown on how improperly subtracting a solely linear component of the substrate background induces artificial artifacts including negative remanence, vertical exchange bias, horizontal shifting along the field axis, and incorrect values of the saturation magnetization and coercivity.

2.2 Experiment

Comparative SQUID magnetometer measurements were taken using a Quantum Design MPMS XL [1] to detail the impact of trapped flux on sensitive thin film measurements. The sample environment in the presence of trapped flux due to applying different magnetic fields was profiled via fluxgate magnetometer optimized for ultra-low field measurements in the SQUID magnetometer. True zero-field condictions are attained through a residual field nulling function that, after the magnet coils are quenched to dissipate trapped flux, any remnant field detected by the fluxgate is nulled by a compensation field opposing the direction of the remnent field. The compensation field is provided by current in a set of secondary windings in the magnet. Field conditions are compared for two GGG substrates from different manufacturers, a nominally 20 nm thick sputtered YIG thin film grown on a GGG, and a palladium (Pd) reference standard. The trapped flux induced in the MPMS XL magnetometer is then compared to that of a brand new MPMS 3.

Samples were mounted in research-grade low-susceptibility polymer measurement cylinders in out-of-plane and in-plane orientations. In-plane was mounted vertically and sandwiched between the ends of a secondary measurement cylinder inserted such that sample movement during oscillations was minimized, and out-of-plane mounted in the same fashion with the addition of slicing a section of cylinder

out and inserting the sample horizontally. Samples were cleaned with isopropyl alcohol, and mounting was performed in a custom built clean room with nonmetalic tweezers on a grounded anti-static pad to reduce the accidental inclusion of environmental magnetic particles.

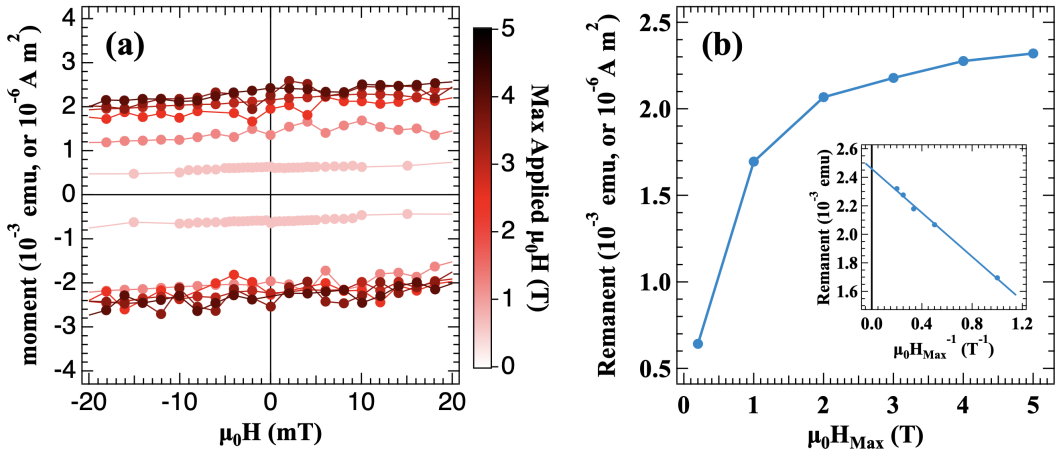

Figure 2.4: Field dependence of artifacts in GGG caused by trapped flux. **(a)** Low field hysteresis loops were taken after ramping the magnet to higher fields, from $\mu_0 H = 0.2$ T - 5 T. **(b)** Subtracting off the linear component, the field shift appears as a saturating negative remanence with a $1/H$ dependence.

2.3 Results and Discussion

To help encourage a reproducible initial state in the sample space environment, we performed a a degaussing of the permalloy shield and magnet reset function. We show in Figure 2.5 that this dissipates any remanent field due to trapped flux in the superconducting coils. We set the field using typical software commands to 2000 Oe, held this field for 5 minutes, then reduced the field to nominal zero using a no-overshoot field ramping method. We then directly measured the magnetic field in the sample space using a calibrated fluxgate magnetometer. The resulting

field profile (green) of the entire sample range shows a remnant field from $2.6 - 11$ Oe and minimizes in the center of the superconducting coils. Secondary windings in the magnet allow for low field correction of the field profile (black, inset) after quenching the magnet. Compensation of the remnant field shows a reduction in field strength at the sample location to less than 0.6% the initial state. Non-uniformity of the trapped flux across the sample space is due to geometry of the solenoid.

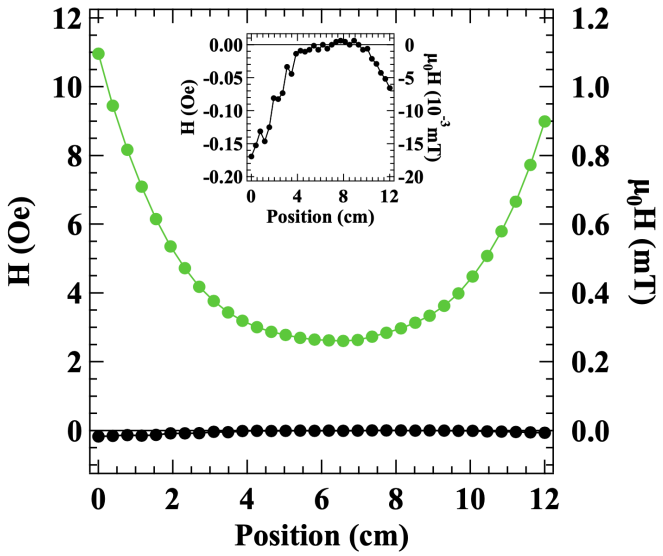

Figure 2.5: Fluxgate H vs position. Remnant field due to trapped flux from setting the magnet to 2000 Oe (green). *Inset:* Magnification of near-zero field conditions (black) achieved by compensation of the remnant field.

Another assumption often made is that removal of trapped flux by quenching the magnet before measurements is sufficient for achieving accurate field values. It is therefor important to understand how remnant fields develop within a measurement itself. Fig. 2.6 shows low-field values of room temperature hysteresis up to 2000 Oe field strength on a bare GGG substrate. Resetting the magnet superconducting coils (red) and zeroing the field using the secondary windings and fluxgate

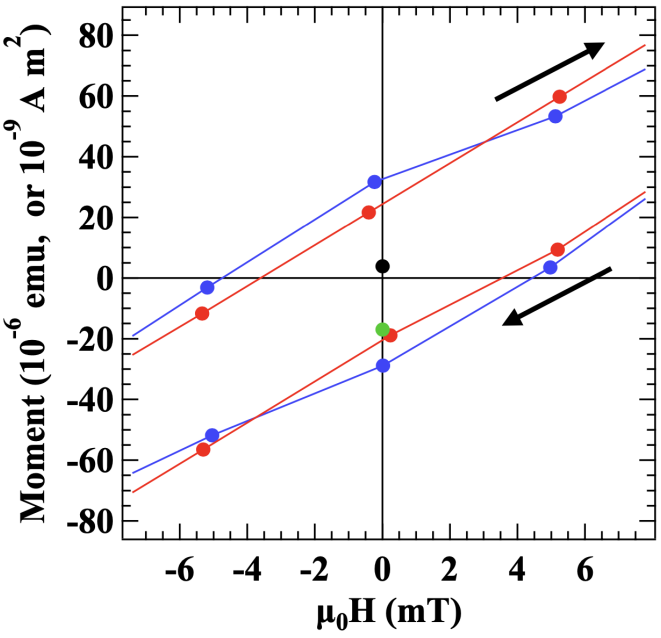

Figure 2.6: Before 2000 Oe hysteresis, a quench of the magnet superconducting coils (red) and zeroing the field using secondary windings and fluxgate magnetometer (blue) shows this is insufficient to account for artifacts induced during the measurement itself. A post-hysteresis measurement at 'zero' field before (green) and after (black) a magnet quench reveals the true zero GGG moment.

magnetometer (blue) are commonly used to reduce the effective true field to zero before the measurement. However, the field applied during the measurement itself causes a similar amount of remnant field due to trapped flux. Setting the field to an expected zero and taking an independent measurement of the sample shows what could be perceived as a negative remanence in the GGG (green). Properly zeroing of the sample space field profile (black) reveals an expected near zero moment with a small positive moment. This is most likely caused by defect or impurity-related ferromagnetism, as often observed in small-moment samples by other authors [36].

As the trapped flux induced by a given field is mostly dependent on pinned flux lines localizing on defects in the superconducting magnet, it is generally repeatable

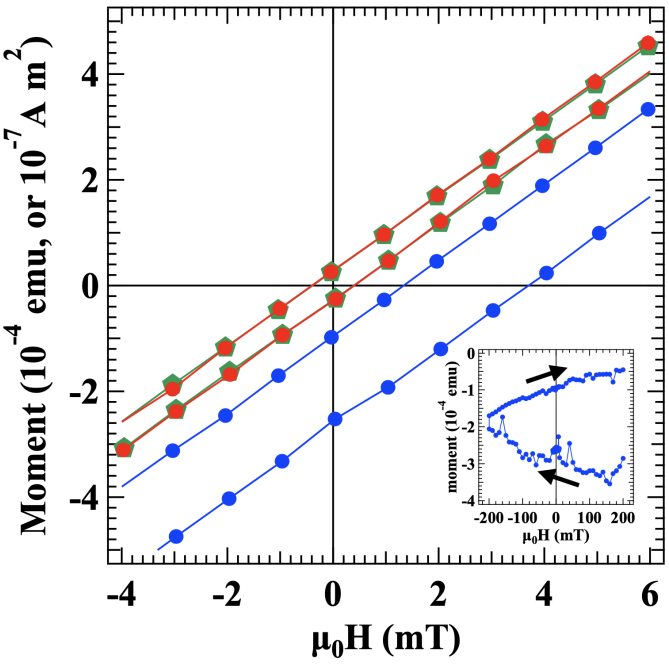

Figure 2.7: Repeatability of trapped flux and high field flux decay. Three identical 200 mT hysteresis loops measured in sequence after a magnet reset (green), ramping the magnet to 5 T (blue), then a magnet reset (red). *Inset:* Subtraction of the linear component of the post-5 T loop reveals flux decay.

and can be characterized for particular instruments. Fig. 2.7 highlights the field history-dependent characterization of the trapped flux for our SQUID magnetometer. An initial hysteresis loop of a GGG substrate at 300 K was performed after resetting the magnet (green) and displays an amount of remnant field consistent with trapped flux from setting the magnet to 2000 Oe. After ramping the magnet up to $50,000$ Oe ($\mu_0 H = 5$ T), the field was reduced down to 2000 Oe and the same hysteresis loop procedure was repeated (blue). The subsequent curve has an near identical paramagnetic slope but is shifted along the positive field axis from zero by roughly $15-40$ Oe. Subtracting the linear component of this 5 T curve reveals a moment profile indicative of a large decaying remnant field (inset). Resetting

the magnet immediately afterwards and running the same 2000 Oe hysteresis loop returns the trapped flux to its original state (red).

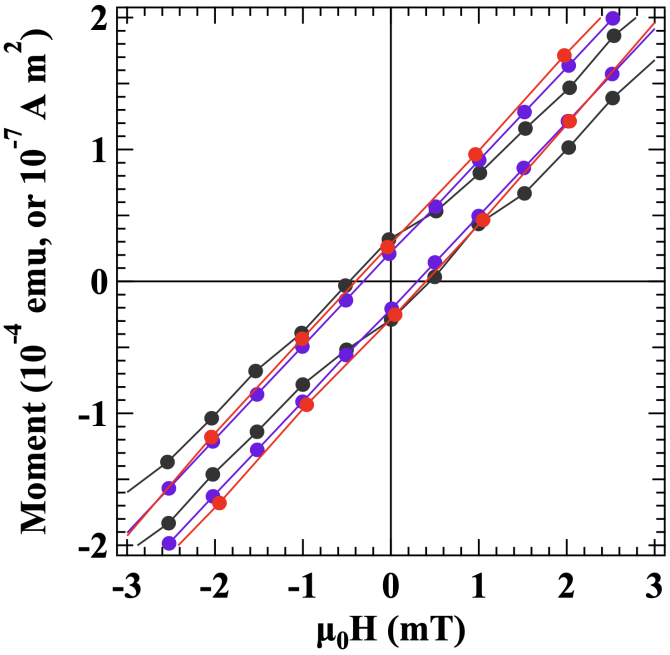

Figure 2.8: Comparison of GGG suppliers and magnetometers. Identical magnetometry sequences were performed on GGG 'A' using a MPMS XL (purple) and MPMS 3 (red), and on GGG 'B' (black) using the MPMS XL.

The density of pinned flux lines between magnetometers is compared by performing measurements on GGG from two commercially available suppliers and on two MPMS models in Fig. 2.8. The first GGG substrate sample, labeled here for simplicity as 'A', is the substrate for YIG/GGG growth [37], and GGG 'B' was procured from another manufacturer [38] for comparison. GGG 'A' was measured using identical hysteresis sequences following a magnet reset on a model MPMS XL (purple) and new MPMS 3 (red) SQUID magnetometers. The superconducting coils show matching remnant field values due to trapped flux. The second GGG sample 'B' (black) with very similar paramagnetic susceptibility was measured on

the MPMS XL with an identical sequence after carefully zeroing the remnant field, showing a near identical remnant field. The difference in slope is due to small differences in the volume. Artifacts being repeatable on different magnetometers and on GGG from different suppliers suggests this is consistent for the superconducting magnet material utilized in these instruments, and reinforces these are not due to manufacturing defects in the substrates.

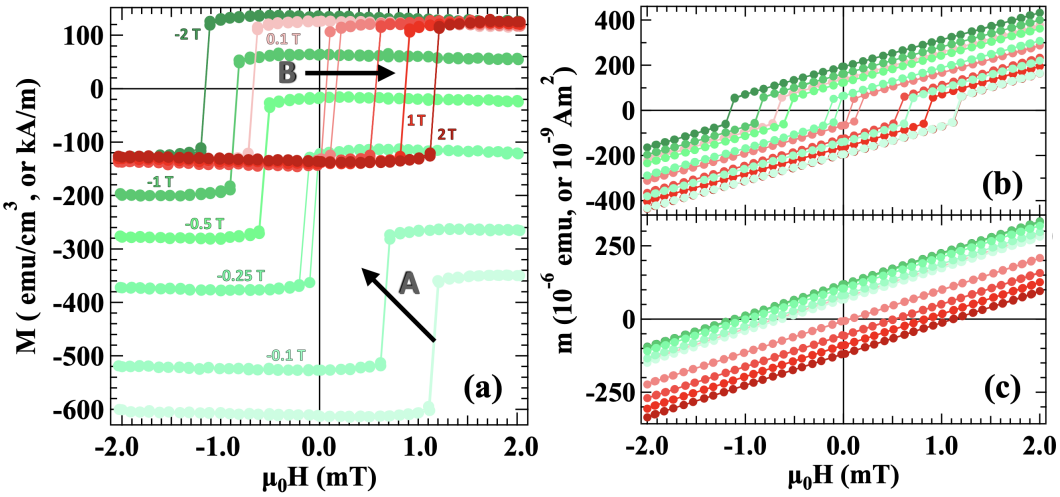

Figure 2.9: Hysteresis loops of YIG with changing magnetic field histories and induced trapped flux for both it and the directly measured and subtracted GGG background. **a)** Direct subtraction of GGG taken with a different field history as the YIG causes vertical shifts (labeled **A**). A 2 T field was initially applied to the YIG, then the trapped flux was shifted by applying the labeled field before each loop. Direct subtract of GGG with an identical field history (labeled **B**) shows the horizontal shift due to the trapped flux. Coercivities at this temperature are much less than 1 Oe. Raw moments for both **b)** YIG/GGG and **c)** GGG substrate.

Taking direct measurements of sample substrates to account for background artifacts is the ideal mechanism for isolating small signals. It still is important to be careful when seeing exciting results via superconducting magnets, even when using direct background subtraction, and understanding how previous field conditions

influence these subtractions is necessary for identifying real interactions. Fig. 2.9 shows the effects of induced trapped flux on direct background subtractions. Small hysteresis loops were taken on YIG/GGG and GGG at 200 K with a range of large magnetic field histories (Fig. 2.9a,b). The green loops have different field histories, and the red have identical field histories. An initial 2 T field was initially applied to the YIG/GGG, then trapped flux conditions modified by applying the a number of decreasing field values before each loop. Direct mass-weighted subtraction of the GGG taken with different field histories as the YIG/GGG causes vertical and horizontal shifts due to differing trapped flux conditions. Direct subtraction with identical field history (labeled **B**) corrects for vertical shifts, while the horizontal shift due to the trapped flux remains. These vertical shifts are caused by applying a linear background subtraction or direct background subtraction with different field history. Horizontal shifts are due to trapped flux from a previous fields larger than the current measurement's maximum field. Trapped flux can cause changes in saturation and coercivity, which can be mitigated by careful direct subtraction or identifying the true field values by measuring a Pd reference standard.

2.4 Conclusions

Extra care is needed for sensitive SQUID magnetometry, particularly for small or complex samples with large backgrounds. Deviations from real and reported values, due to trapped flux, zero current offset, impurities, and more, can cause a range of artifacts. Vertical shifting can be caused by either linear or direct subtractions with differing field histories, horizontal shifts from larger remnant fields than are produced by the current measurement, saturation shifting from both trapped flux and signal aberrations, and a shifting of coercivity. Direct measurement and sub-

traction of appropriate backgrounds, repeatable field conditions, and Pd reference field corrections are necessary to mediate these well understood instrumentation artifacts. Finally, GGG from multiple suppliers has shown to be paramagnetic with a slight ferromagnetic signal.

Chapter 3

Magnetization and Antiferromagnetic Coupling of the Interface Between a 20 nm $Y_3Fe_5O_{12}$ film and $Gd_3Ga_5O_{12}$ substrate

We present evidence for and characterization of an approximately 4 nm thick $(Y_{1-x}Gd_x)_3Fe_5O_{12}$ layer with $x \geq 0.4$ formed at the interface between a gadolinium gallium garnet (GGG) substrate and a sputtered $Y_3Fe_5O_{12}$ (YIG) epitaxial film with nominal thickness of 20 nm. Temperature-dependent polarized neutron reflectometry (PNR) and superconducting quantum interference device (SQUID) magnetometry show antiferromagnetic alignment of this interfacial layer with the bulk of the YIG film at low T that persists to at least 3 tesla. These experiments also show that this interfacial alignment switches from antiparallel to parallel between 100 and 200 K in small applied magnetic fields. Simple modeling suggests correlation of this crossover with the ferrimagnetic compensation point of the mixed garnet that forms this interfacial layer.

3.1 Introduction

As all forms of YIG thin film growth on GGG typically relies on reaching temperatures near 700° C either during growth or in a post-growth annealing step, and considering the similar chemical properties of Y and Gd, interdiffusion at the

YIG/GGG interface is not surprising. This is one explanation put forward for recent observations of an interfacial layer and/or antiferromagnetic coupling that forms between the YIG and the GGG [39–47]. Modification of magnetic properties at an interface is, of course, common for a variety of reasons [48]. Some form of modified magnetic order, with an awareness of the likely role of interdiffusion of atomic species at the film/substrate interface has been discussed for YIG for some decades. LeCraw, *et al.* [49] argued, based on magnetic domain imaging, that garnet films grown by liquid phase epitaxy (LPE) and annealed at 1100° C experienced diffusion of Ga.

More recent reports using more powerful experimental probes have refined this view. Studies using the magneto-optical Kerr effect (MOKE) and spectral ellipsometry on 6 nm -30 nm thick YIG films sputtered at ambient temperatures onto GGG substrates and post annealed at 800° C provided evidence for a layer at the YIG/GGG interface with magnetization aligned antiparallel to that of the YIG [39]. Further evidence of modified magnetism at the YIG/GGG interface came from polarized neutron reflectometry (PNR) [42], though that study argued for a non-magnetic interfacial layer. Suturin *et al.* also reported a magnetically “dead" interfacial layer based on PNR, x-ray reflectometry and spectroscopy and secondary ion mass spectrometry on YIG/GGG grown via laser molecular beam epitaxy at 700° growth temperature [44]. This group also suggests Ga interdiffusion is responsible. Gomez-Perez *et al.* used spin Hall magnetoresistance and x-ray circular dichroism to again argue for an antiferromagnetically-coupled interface layer in a 13 nm film grown on a GGG substrate via pulsed laser deposition [43].

As reported in that work, scanning tunneling electron microscopy with energy dispersive x-ray spectroscopy argued that the interface layer is formed from

gadolinium iron garnet (GdIG), where Gd entirely replaces Y in the synthetic garnet structure. This replacement can occur with little energy cost since Y and Gd are chemically similar, though the addition of the Gd 4f shell magnetic moment causes large magnetization at low temperature and the interaction between the Gd and Fe moments introduces a lower ferrimagnetic compensation temperature. In bulk, mixed rare-earth garnets, $(Y_{1-x}Gd_x)_3Fe_5O_{12}$, have been shown to have a composition-dependent ferrimagnetic compensation temperature, which decreases from near 300 K for pure GdIG to < 50 K for $x = 0.1$ [50]. All compositions maintain the much higher temperature (near 550 K) magnetic transition seen in pure YIG. Ferromagnetic resonance (FMR) studies also indicate modified or antiferromagnetically coupled interfacial layers in various YIG thin films on GGG [46, 51]. Though most of these reports detail a modified magnetic structure in these heteroepitaxial YIG/GGG samples, this interface is not completely understood. This is partly due to the challenges already discussed for traditional magnetometry on the very large paramagnetic background from the GGG substrate.

The large paramagnetic susceptibility of GGG presents obvious challenges for magnetometry of nm-scale thin films grown on GGG substrates [40, 41, 52, 53]. For this reason, quantitative magnetometry of YIG films on GGG substrates is rare, especially exploration of the temperature ($T-$)dependence at low T where the GGG background magnetization grows very large. Mitra, *et al.* did present SQUID magnetometry of YIG films with thickness 40 nm and greater grown on GGG substrates via RF reactive sputtering [41]. These show reduced magnetization from bulk YIG values at all temperatures, though the model the authors present considers an antiferromagnetically coupled layer at the YIG-GGG interface that contributes only below 100 K. At low temperatures, a reduction in moment was seen that grew largest

for the thinnest reported sample, and with support of PNR and electron microscopy, Mitra, *et al.* suggested an interdiffusion of Y and Gd in a 4 nm -6 nm thick layer at the interface.

Presented here are results of polarized neutron reflectometry (PNR) done by collaborators at NIST and SQUID magnetometry vs. T, with careful consideration of the background GGG substrate subtraction, on a nominally 20 nm thick sputtered YIG thin film. PNR confirms not only the presence of an antiferromagnetically coupled $(Gd_xY_{1-x})_3Fe_5O_{12}$, or (Gd-Y)IG, layer, but also that this layer retains its moment and antiferromagnetic alignment to the YIG at low T even in very large applied field. PNR also shows a cross-over from antiferromagnetic to ferromagnetic alignment of the interfacial and YIG films between $100-200$ K. To perform SQUID magnetometry the background contributions determined by performing exactly the same field sweeps on a companion GGG substrate with no YIG are subtracted to isolate the magnetic contribution of the interface layer and YIG film. These measurements again confirm the presence of a magnetic (Gd-Y)IG interface layer, that shows antiferromagnetic alignment with respect to the YIG at low T, with a crossover near that seen in PNR. Estimated modeling of the magnetization argues that the ~ 4.1 nm thick interfacial layer has a fairly high concentration of Gd, and suggests that the change in interfacial coupling could be tied to the ferrimagnetic compensation point of the mixed garnet interfacial layer.

3.2 Experiment

We grew a nominally 20 nm thick YIG layer on a GGG substrate via RF sputtering at ambient temperature. After sputtering, the film was annealed at 800° C in 1.1 Torr (147 Pa) partial O_2 pressure for 240 min. Further details of the growth tech-

nique and typical resulting damping parameter and other properties are discussed elsewhere [52,54]. The GGG was purchased commercially [37] as a 0.5-mm-thick, 10 mm by 10 mm square, and cleaved to ≈ 5 mm $\times$ 5 mm for use as substrates.

Model fitting of specular PNR data allows us to infer the depth profiles of the complex nuclear scattering length density; ρ_{N}, indicative of the nuclear composition, and the magnetic scattering length density; ρ_{M}, which is proportional to the in-plane magnetization, M, for thin films and multilayers [55]. We conducted PNR measurements using the Polarized Beam Reflectometer at the NIST Center for Neutron Research. An incident 0.475 nm neutron beam was polarized with magnetic moment parallel (+) or antiparallel (-) to a magnetic field, H, applied along the plane of the sample. We measured the spin analyzed non spin-flip specular reflectivities $--$ and $++$ as functions of wavevector transfer Q along the sample growth axis. We collected data both as a function of varying T and H as described below.

We reduced the PNR data using Reductus [56], and performed model fitting using Refl1D [57]. We simultaneously fit data for all T and H conditions to a single universal model with a fixed nuclear profile and condition-dependent magnetic profiles. As described in more detail below, the data could not be represented with a simple model corresponding to a single YIG layer on a GGG substrate. The data are well-fit with a model featuring a magnetically distinct sub-layer at the YIG / GGG interface, similar to previous reports [41, 42, 44, 58]. We calculated the GGG and non-interfacial YIG layer ρ_{N} values using bulk density values and the wavelength-dependent scattering lengths of the constituent isotopes [59,60], which we treated as fixed parameters. We note that Gd is the only element in the sample with an appreciable imaginary ρ_{N} component. The magnetically distinct region at the GGG/YIG interface is likely a result of diffusion of chemical species. For our

model, we approximate this phenomenon using a single layer with fitted and rough interfaces [61]. As GGG is essentially paramagnetic at the temperatures measured, the magnetization of the GGG substrate was constrained to be parallel to the applied field direction (i.e. $\rho_{\mathrm{N}} > 0$). This constraint is consistent with SQUID measurements, and lifting it does not appreciably affect the fit quality. We determined fitting parameter uncertainties using a Markov chain Monte Carlo algorithm [62] packaged with Refl1D. The average two standard deviation uncertainty for PNR-determined magnetization values is approximately 5 $\mathrm{kA/m}$. It is important to note that these uncertainties are based on known statistical uncertainty in the data, and do not account for potential systematic error in the measurements, or uncertainty associated with choice of model. All uncertainties given for fitting parameters correspond to two standard deviations, while uncertainties shown for scattering data correspond to one standard deviation.

We performed SQUID magnetometry in a commercial system equipped with integral magnetic shielding, with magnet reset capabilities and a 7 T magnet, with automated temperature control from 2 K $-$400 K using a reciprocating sample method to increase the signal-to-noise ratio [1]. The YIG/GGG sample and the companion substrate were nearly equal size, and mounted in the magnetometer using the same techniques. Samples were mounted in a laminar flow hood using dedicated non-metallic tools and clean gloves to minimize contamination from dust and other potential sources of magnetic contamination. We took care to replicate both temperature and magnetic histories by using identical measurement sequences on substrate and sample, and the magnet was reset before each measurement to minimize trapped flux.

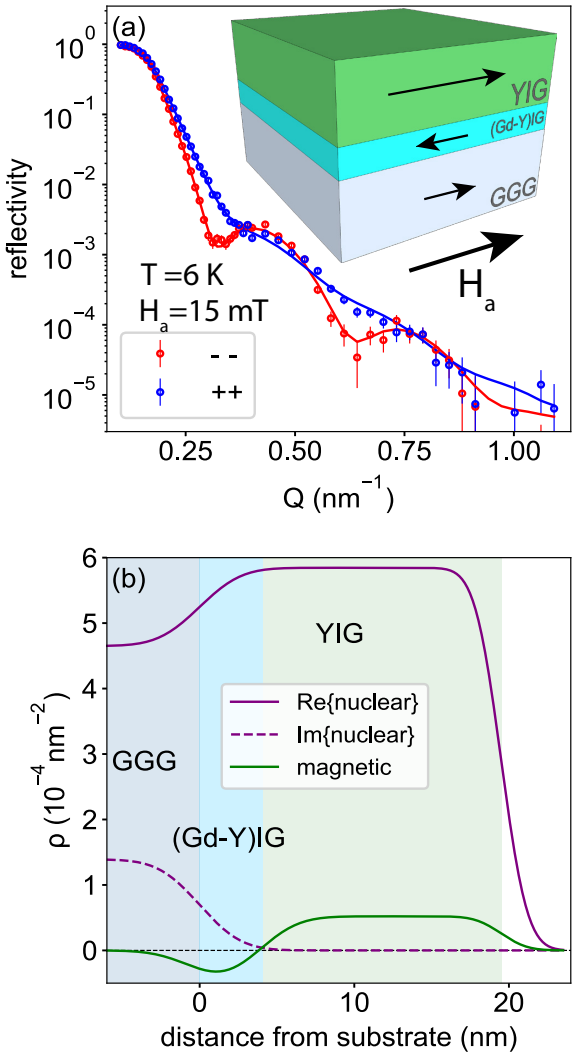

Figure 3.1: **a)** Polarized neutron reflectivity data measured at 6 K and 15 mT for both spin analyzed non spin-flip specular reflectivities, $++$ (blue symbols), and $--$ (red symbols), with fits shown as solid lines. **Inset:** Schematic view of the sample showing GGG substrate, (Gd-Y)IG interfacial region, and YIG film, with magnetization corresponding to conditions of this measurement shown schematically with black arrows. **b)** Nuclear, ρ_N, and magnetic, ρ_M, scattering length density profiles determined from fits to the data.

3.3 Results and Discussion

Fig. 3.1a shows example polarized neutron reflectivity data for the YIG/GGG sample at 6 K measured in an applied field of $\mu_o H = 15$ mT ($H = 150$ Oe). This field is much larger than the expected coercive field, H_c, of YIG. We plot reflectivity vs. neutron wavevector, Q, for both neutron spin polarizations. The fitted data features clear, well-represented, spin-dependent oscillations. Fig. 3.1b shows the corresponding nuclear (ρ_N) and magnetic (ρ_M) scattering length density vs. distance perpendicular to the substrate, z, where an additional (Gd-Y)IG layer between the GGG substrate and bulk-like YIG was necessary to adequately model the data. These three regions: the GGG substrate, the ≈ 4 nm (Gd-Y)IG, and the 15.9 nm YIG film, are indicated by background shading. Testing of different models showed that our sensitivity to the nuclear profile is insufficient to reliably characterize the chemical composition of the nominal (Gd-Y)IG layer. We can tell that the interfaces are rough, but cannot uniquely distinguish if the interfacial layer results from an off stochiometric Gd composition or Ga diffusion, both of which have been reported in the literature [41, 44, 49] While ρ_M is small compared to ρ_N, it gives rise to distinct spin-dependent features in the data that yield high confidence in ρ_M for the individual layers. Thus, we can conclude that at low T near the YIG remanence, the GGG is only weakly magnetized, while the YIG and (Gd-Y)IG layer magnetizations are oriented antiparallel to one another, with the YIG magnetization tracking the direction of H.

The depth sensitivity demonstrated in Fig. 3.1 allows for layer resolved magnetometry, as shown in Figure 3.2 with T-dependencies in 15 mT (left column) and 3 T (right column). The T-dependent fitted data are shown in panels (a-b) as

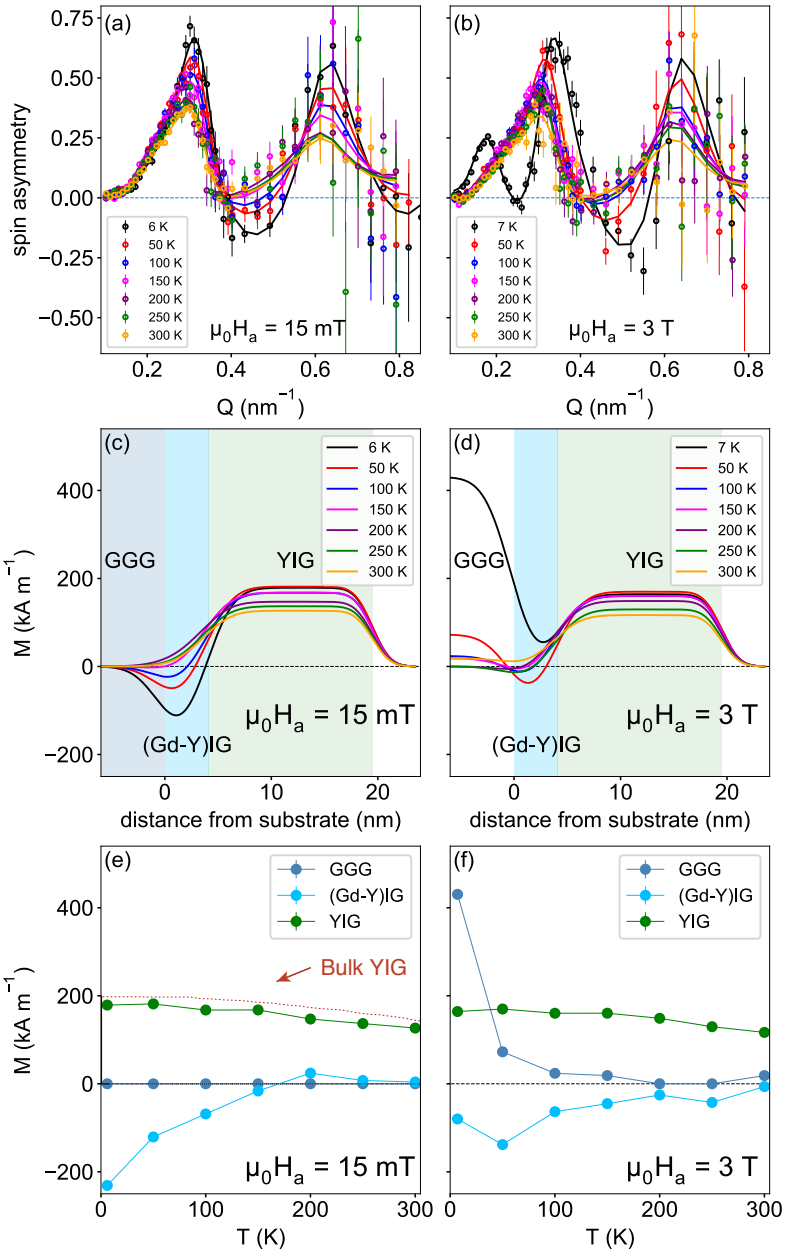

Figure 3.2: PNR spin asymmetry (**a-b**), magnetization profiles determined from model fitting (**c-d**), and resulting M vs. T measured for $\mu_0 H = 15$ mT (left) and $\mu_0 H = 3$ T (right). The three magnetic components of the sample are shown in background shading in panels (**c-d**), and their M separately plotted in (**e-f**). We provide bulk values of $M(T)$ for YIG for comparison in panel **e**.

spin asymmetry (difference in $++$ and $--$ divided by their sum), which is a useful quantity for visualizing changes in the magnetic scattering when the nuclear contribution to the scattering can be assumed to be static. The magnetic profiles are shown in panels (c-d), plotted in units of magnetization ($1\ \mathrm{kA/m} = 1\ \mathrm{emu/cc}$) vs z. Panels (e-f) summarize the profiles in a more familiar plot of $M(T)$ for each layer. The two sigma statistical uncertainties for these fitting parameter values are too small to be seen at this scale.

At 15 mT, a modest field but well above expected in-plane coercive field, H_c, for the YIG film, the YIG magnetization tracks very closely to the expected $M(T)$ for bulk YIG, shown as a dotted red line [50]. The interfacial (Gd-Y)IG layer magnetization stays antiparallel to H up to 150 K, where it crosses over to become weakly positively magnetized, suggesting that the interlayer antiferromagnetic coupling between the two layers weakens considerably over this temperature range. The 3 T $M(T)$ in Fig. 3.2f shows little change for the YIG magnetization, as expected given the material's low coercivity. The GGG $M(T)$ also behaves as expected, showing a roughly $1/T$ dependence, dominated by a very large low T magnetization induced by the very large field. This largely paramagnetic response at low T approaches zero above 50 K. Remarkably, the magnetization of the (Gd-Y)IG layer is negative at low T, and only approaches zero kA m^{-1} above 100 K. Note that the large paramagnetic contribution from the GGG at $T = 7$ K makes the very substantial negative peak from the interface layer somewhat less visually obvious. The fitting of the three components clearly identifies large negative contributions from the interface at low T. Thus, we see that even a 3 T applied field is insufficient to fully reverse the magnetization of the interfacial layer, demonstrating the strength of the antiferromagnetic interlayer exchange.

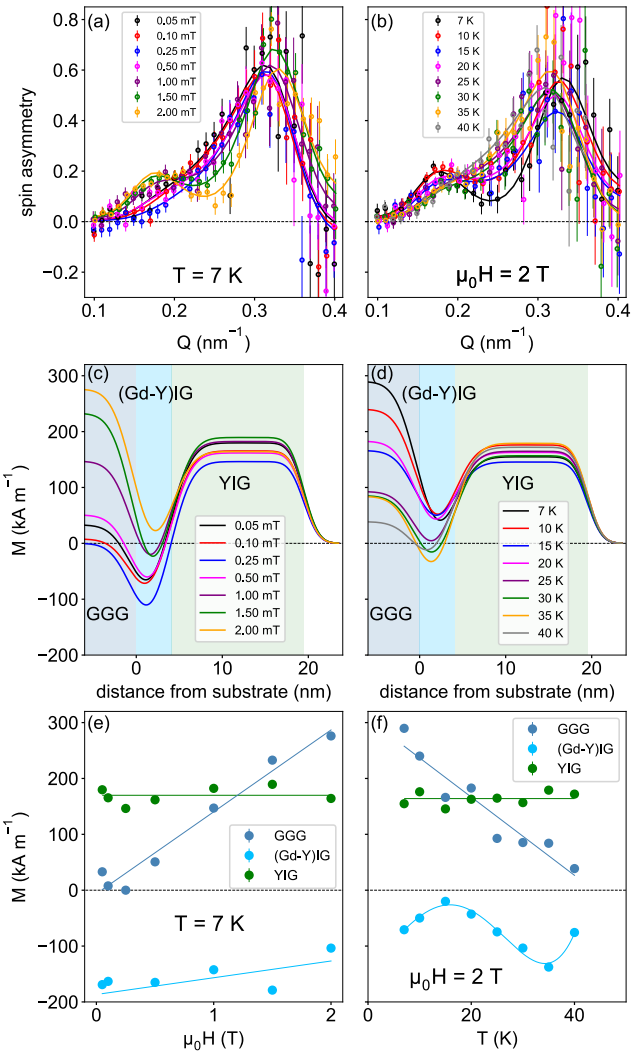

Figure 3.3: PNR spin asymmetry (**a-b**), modeled magnetization profiles (**c-d**), and resulting M vs. $\mu_0 H$ at fixed $T = 7$ K **(e)** and M vs. T at fixed $\mu_0 H = 2$ T **(f)**. Solid lines in **e)** and **f)** are guides to the eye. Possible non-monotonic behavior of the (Gd-Y)IG layer could result from frustrated domains in this interfacial layer. Note however, that the negative M at all $\mu_0 H$ for the (Gd-Y)IG indicates very strong antiferromagnetic exchange at the interface.

Figure 3.3 shows layer resolved $M(H)$ at 7 K (left column) and a small T-step $M(T)$ at 2 T. As in Fig. 3.2, panels (a-b) show spin asymmetry, panels (c-d) show the magnetization depth profiles determined from model fitting of the data,

and panels (e-f) show show the associated layer-resolved $M(H)$ and $M(T)$, respectively. Solid lines in (e-f) are guides to the eye. As expected for a ferromagnet well below T_c, the YIG magnetization is essentially constant with both field and temperature. The GGG also behaves intuitively, with linear field and temperature responses characteristic of a paramagnet. The (Gd-Y) magnetization shows a linear increase with H, as the Zeeman energy begins to overcome the antiferromagnetic interlayer exchange. The temperature dependence of the (Gd-Y)IG layer magnetization is more complex, deviating considerably from a monotonic response. This is suggestive of a frustrated domain state in the interfacial layer at low T. However, while the deviation is outside our statistical uncertainty (approximately 5 kA/m, error bars too small to be seen on this scale), we cannot rule out the possibility that this is an artifact associated with unaccounted uncertainty in the modeling. To wit, the YIG and GGG magnetizations in (e-f) also show much less pronounced but still statistically significant – and likely unphysical – degrees of non-monotonicity.

We note that the magnetization values shown in Fig. 3.2 (e-f) and Fig. 3.3(e-f) differ slightly from the corresponding profile values shown in Fig. 3.2 (c-d) and Fig. 3.3 (c-d). This is because the profiles show weighted averages of the (Gd-Y)IG layer with that of the neighboring GGG and YIG layers, while the $M(T)$ and $M(H)$ plots show parameter values corresponding to the inherent magnetization of the (Gd-Y)IG layer [63]. However, we emphasize that the qualitative conclusions drawn in this work are the same regardless of which values are considered.

Quantitative measurement and analysis of the magnetization of the same sample via SQUID magnetometry requires careful consideration of the large substrate background. Fig. 3.4a plots $\chi = M/H$ vs. T from 2 K -300 K measured in a single experimental run at fixed $\mu_0 H = 10$ mT (100 Oe). As expected for a para-

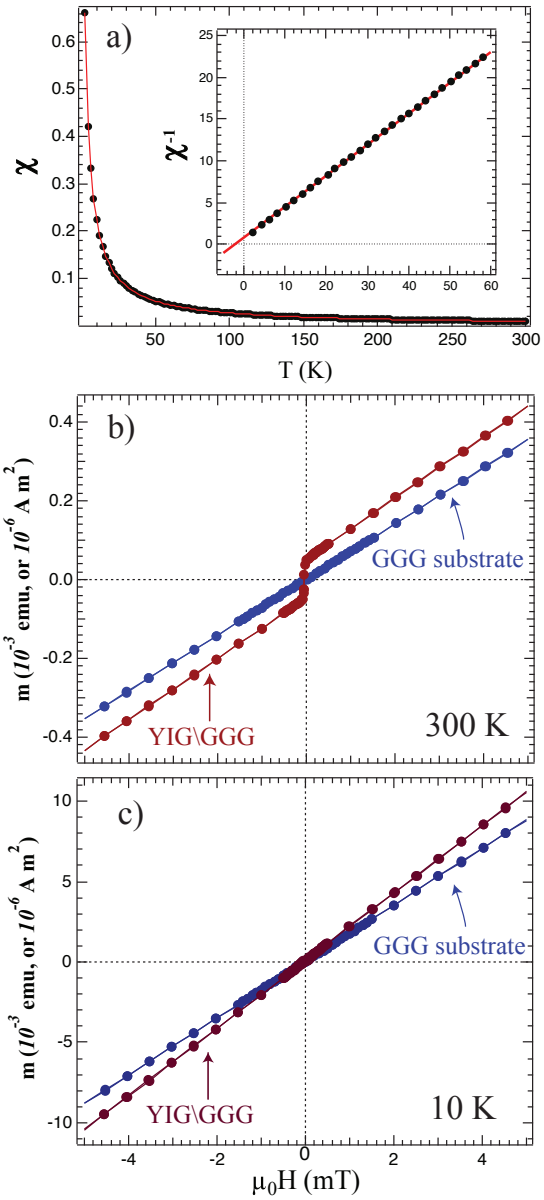

Figure 3.4: **a) a)** $\chi = M/H$ vs. T for the bare GGG substrate in $\mu_0 H = 10$ mT vs. T from 2-300K. **Inset:** $1/\chi$ vs. T. In both the red line is a fit to the Curie-Weiss law with a small negative θ, as expected for GGG. **b)** m vs. $\mu_0 H$ at 300 K for the GGG substrate and the YIG/(Gd-Y)IG/GGG sample. At this T both the large paramagnetic contribution from the GGG and the essentially ferromagnetic contribution from the YIG are obvious even without background subtraction. **c)** m vs. $\mu_0 H$ at 10 K, where the paramagnetic background dominates the ferromagnetic signal. The different slopes are due to a slight difference in the substrate volume.

magnet, $\chi \propto 1/T$. The red line is a fit to the Curie-Weiss law, $\chi = A/(T-\theta)$, with $\theta = -2.1$ K, which is in line with expectations for GGG. Fig. 3.4b) and c) compare the total moment m of the YIG/GGG and companion bare GGG substrates measured over a small H range at 300 K and 10 K, respectively. At 300 K, the GGG background is small enough to clearly resolve the YIG ferromagnetic contribution on this scale, while at 10 K, the background paramagnetic contribution is already large compared to the more weakly T-dependent YIG ferromagnetism. The slight difference in the total moment for the sample and background that is obvious at 10 K is caused by a small size difference between the two substrates, which we scale appropriately in the following comparisons. In these small H scans, the GGG appears mostly as a simple paramagnet. As we describe in more detail elsewhere [64], larger field M vs. H scans on GGG can cause measurement artifacts driven by trapped flux in the superconducting magnet used in the magnetometer. Here we avoid these artifacts by using this small field range and subtracting the GGG background measured under the same field and temperature sequences.

Figure 3.5 shows M vs. $\mu_0 H$ for the YIG/(Gd-Y)IG/GGG sample, where we have subtracted the background M measured on the companion GGG substrate using the same ± 5 mT field scan sequences for both, after scaling by the measured mass ratio of the two substrates to correct for the small volume mismatch. As seen in Fig. 3.5a), at 300 K this leaves the low coercivity ferromagnetic behavior of the YIG, with a symmetric saturation and slight shift on the $\mu_0 H$ axis that cannot be clearly separated from trapped flux in the magnet. As T drops, the loops all show the expected ferromagnetic hysteresis pattern, with clearly defined saturation, though with monotonically increasing coercive field. Some loops, most clearly the 10 K loop in panel h) that shifts almost entirely above $M = 0$, show an apparent vertical

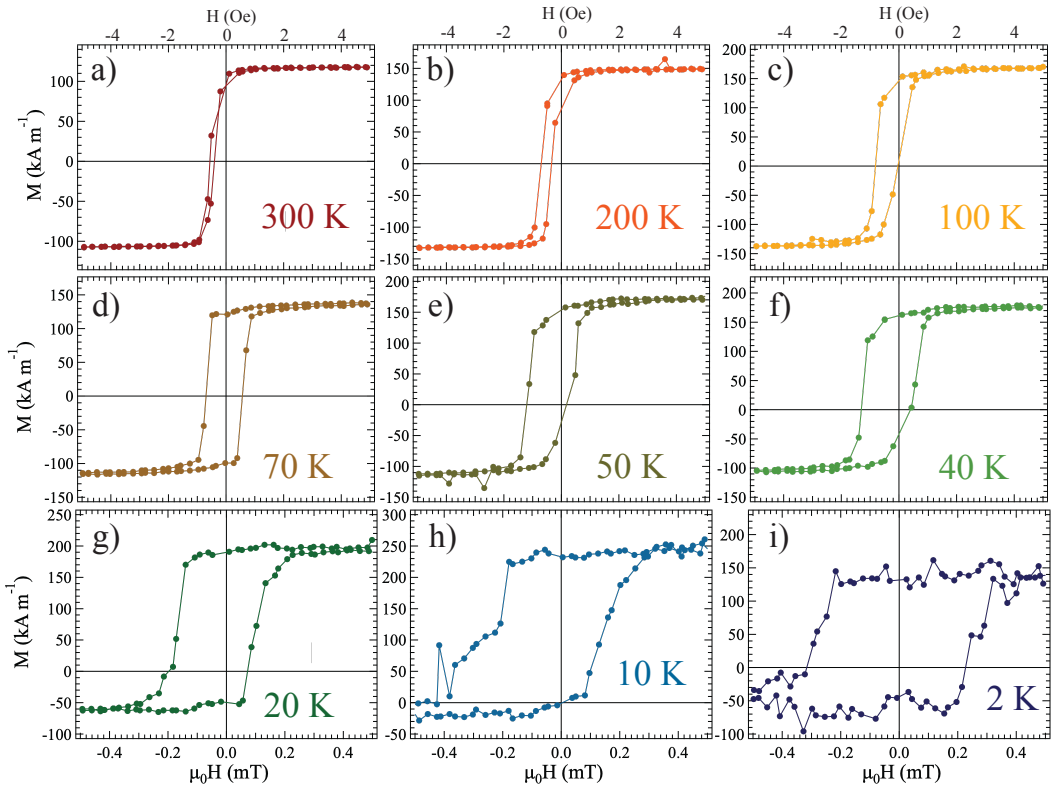

Figure 3.5: M vs. $\mu_0 H$ loops for the YIG/(Gd-Y)IG/GGG sample after subtraction of the matched GGG background for a series of temperatures: **a)** 300 K, **b)** 200 K, **c)** 100 K, **d)** 70 K, **e)** 50 K, **f)** 40 K, **g)** 20 K, **h)** 10 K, and **i)** 2 K. All loops show the expected FM hysteresis and positive remanence, with H_c growing as T drops. Neither the small shift on the $\mu_0 H$ axis nor the shift on the M axis can be clearly linked to the YIG/(Gd-Y)IG, as discussed in the main text.

shift, though this shift is not monotonic with T. Similar vertically shifted loops have been attributed to pinned moments in magnetic heterostructures involving antiferromagnetic exchange coupling [65–67]. However, considering the possible artifacts introduced by the large GGG paramagnetism interacting with trapped flux [64], we cannot attribute these shifts to the antiferromagnetic exchange coupling between the YIG and (Gd-Y)IG layers.

In Fig. 3.6a) we report saturation magnetization, M_s, vs. T, determined from M vs. H loops as shown in Fig. 3.5. To isolate the contribution of the thin film, we calculate M_s via:

$$M_s = \frac{M_{+,\text{avg}} - M_{-,\text{avg}}}{2}, \tag{3.3.1}$$

where $M_{+,\text{avg}}$ and $M_{-,\text{avg}}$ are averaged values of saturated M on the positive and negative field branches of the loops, respectively. This cancels the vertical shift apparent in some loops. In Fig. 3.6a, the blue symbols indicate this M_s, which is calculated using the entire volume of the deposited film, with its total nominal thickness of 20 nm. Data was taken in two separate runs in the magnetometer, indicated by circles and squares. These show slight deviations, though not outside the estimated error bars. We compare this to the M_s calculated using a very typical procedure for substrate background subtraction where a linear background is fit to the highest H data and subtracted. This is shown using grey data points, which underreports M_s compared to the more accurate procedure which uses carefully matched measurements of a companion GGG substrate. We also compare to M_s vs. T reported for bulk YIG (red line) [50]. The measured values fall below the bulk YIG expected values at all T, which is due at least in part to the interfacial layer with its antiferromagnetically aligned low T moment.

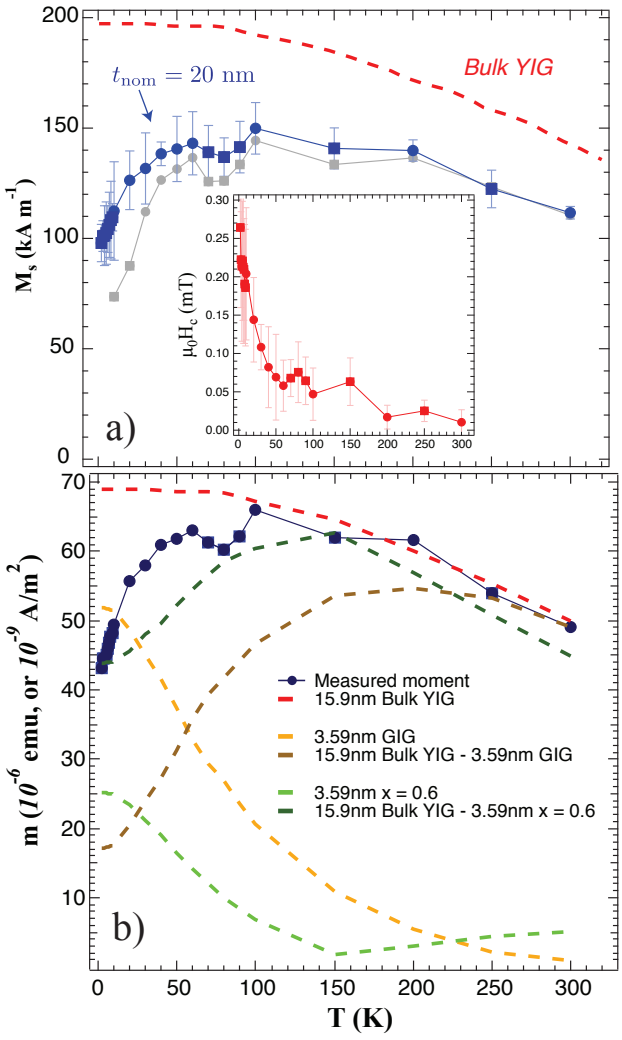

Figure 3.6: **a)** M_s vs. T for the YIG/(Gd-Y)IG films. The blue data points show M_s with volume calculated for the entire nominal film thickness, $t_{nom} = 20$ nm. M_s falls below bulk YIG values (dashed red line) at all T. The grey data points show M_s when a simple linear background is assumed, instead of using the measured GGG values. *Inset:* $\mu_0 H_c$ vs. T shows a monotonically decreasing trend. **b)** Measured moment m of the YIG/(Gd-Y)IG layer (blue) compared to calculated values for a 15.9 nm thick layer of bulk YIG (dashed red line), 3.6 nm thick layers of $(Y_{1-x}Gd_x)_3Fe_5O_{12}$ with $x = 1$ (GdIG, dark yellow line), and $x = 0.6$ (green line), and two models subtracting these two contributions to reflect the antiferromagnetic alignment (brown and darker green lines).

We report H_c vs. T determined from the same loops in the inset to Fig. 3.6a). H_c rises as T drops roughly following $1/T$, growing largest in the T regime where M_s drops sharply. An increase in H_c of this type can be driven by thermal fluctuations and also enhanced by exchange coupling with an antiferromagnetic layer [68–72]. Typically this AF/FM coupling also introduces exchange bias. Here we cannot identify a systematic shift of the loops, potentially again due to issues related to trapped flux. However, the lack of a well-defined exchange bias could indicate that the coercivity increase is dominated by decreasing thermally-driven depinning of domain walls rather than interfacial effects.

In Fig. 3.6 we explore a simple model of the YIG/(Y_xGd_{1-x})IG/GGG system. The blue data points plot total measured moment, m vs. T, and we compare this first to bulk YIG M_s values multiplied by the volume resulting from a 15.9 nm film thickness as determined by PNR (Figs. 3.1 and 3.2), indicated by the dashed red line. At the lowest T the total m falls far below the values for bulk YIG, where the interfacial moment is large and antiferromagnetically aligned with the YIG. As T grows, m approaches the bulk YIG values. As seen more clearly below, above $\sim 100-200$ K the measured moment rises slightly above the bulk YIG moment, which is in line with PNR measurements that indicate a crossover from AF to FM alignment of the interfacial layer with the YIG near this temperature at these modest applied H. We provide upper and lower estimates of the contribution of the 3.6 nm interface layer again by simple scaling of published bulk (Y_xGd_{1-x})IG values [50]. The dark yellow and green curves show the expected moment of 3.6 nm thick layers with $x = 1$ (pure GdIG) and $x = 0.6$, respectively. We show the resulting estimates of the total magnetization from subtracting the interface magnetization from the 15.9 nm bulk-like YIG layer in brown and dark green dashed lines. Though this

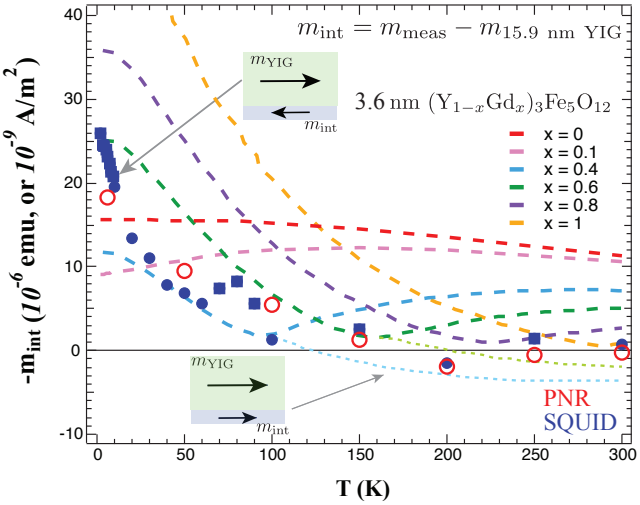

Figure 3.7: Estimated moment of the (Gd-Y)IG interface layer, $-m_{\text{int}}$ vs. T from SQUID magnetometry (blue symbols), and PNR (red circle) compared to bulk values of $(Y_xGd_{1-x})Fe_3O_{12}$ for various x (dashed lines). For the $x = 0.4$ and $x = 0.6$ mixed garnets we also show the moment with reversed sign above T_{comp}, which roughly brackets the measured $-m_{\text{int}}$ from both PNR and SQUID at high T. At low T, $-m_{\text{int}}$ again falls roughly between the values for $x = 0.4$ and $x = 0.6$, suggesting that the interface layer has a high Gd content, though is most likely not purely bulk-like GdIG.

modeling is only qualitative, we can argue that the interfacial layer is more likely to have a high concentration of Gd, since at low T the total moment falls near the modeled values for $x = 0.6$. Note that this model using $x = 0.6$, which always assumes antiferromagnetic coupling of the interface and YIG, does not explain the total m well above ~ 150 K.

We examine the issue of the T-driven change in interfacial alignment with a similar simple modeling approach in Fig. 3.7. Here we subtract the 15.9 nm thick bulk YIG moment from the measured total moment of the film to give an estimated contribution of the interface moment, m_{int}. Fig. 3.7 plots $-m_{\text{int}}$ determined from SQUID magnetometry (blue data points), along with the interfacial moment

determined from PNR (red circles). These agree well for all T, and both show a cross-over from AF to FM alignment (as indicated schematically) of the interfacial and YIG film moments. We again compare these moments with the published data for a range of (Y_xGd_{1-x})IG layers, again assuming 3.6 nm thickness to calculate total moment. As seen in Fig. 3.6, the estimated interfacial component, especially at low T, matches best with mixed garnets with fairly large x. However the measured $-m_{\text{int}}$ is never large enough to match expectations for a simple pure GdIG layer. The most likely scenario is a distribution of Gd composition through the 3.6 nm film, with the average composition approximately between $x = 0.4$ and $x = 0.6$. We note that mixed garnets with this composition have ferrimagnetic compensation points, T_{comp} near the T where the interfacial coupling of the interface and film reverse. The compensation point originates in the different T-dependence of the moment of the Gd and Fe sublattices in the (Gd-Y)IG, such that T_{comp} indicates where the Fe sublattice has a larger contribution to the total moment than the Gd sublattice. The Fe sublattice could in turn show a tendency toward ferromagnetic exchange coupling to the entirely Fe sublattices of the YIG. We can adapt our very simple model to this situation by reversing the moment of the interfacial contribution above T_{comp}, which we show with the dotted blue and green lines for $x = 0.4$ and $x = 0.6$, resepectively. The measured $-m_{\text{int}}$ from both SQUID and PNR falls between these lines.

If the crossover from AF to FM alignment of the interfacial layer and YIG in these heterostructures is indeed determined by the compensation point of the (Gd-Y)IG mixed garnet formed from interdiffusion at the interface, then one expects the T of the switch between AF and FM alignment of the two films to be strongly dependent on the details of the interdiffusion and the average composition of the re-

sulting mixed layer. In very high x interfacial layers, a reversal in coupling may not be observed until above 300 K, since T_{comp} for GIG falls near or above room T. It is also conceivable that heterogeneity of the composition of Gd in the interface layer could lead to a wide range of T_{comp} and competing interactions that could present as a non-magnetic interfacial layer. This could explain the variation in previous reports of the magnetic character and alignment of the interfacial layer between GGG and YIG. Note that this simple analysis assumes that the magnetization of both the 15.9 nm thick YIG and the 3.6 nm thick (Gd-Y)IG films are essentially the same as bulk.

3.4 Conclusions

In summary, we presented evidence for and characterization of a mixed Gd and Y garnet interface layer formed between an essentially bulk-like 15.9 nm thick epitaxial YIG film and a GGG substrate. Using PNR and SQUID magnetometry, we show that antiferromagnetic alignment between the YIG and the interfacial layer of (Gd-Y)IG persists to very large fields at low temperature. In small (or zero) applied field both probes show a crossover from antiferromagnetic to ferromagnetic alignment of the interfacial and film moments. We suggest a possible correlation of this cross-over with the ferrimagnetic compensation point in the (Gd-Y)IG mixed garnet that forms the interface, which in our case has a fairly high Gd content but is not entirely GIG. Variations in the interfacial layer composition will lead to variation in T_{comp} which could explain discrepancies in earlier studies of the YIG/GGG system. The magnetic properties of this interface layer has potential impact on a wide range of studies involving YIG grown on GGG, from fundamental magnetism to magnonics and spintronics.

Chapter 4

Magnetic Characterization of Thin Films by SQUID Magnetometry

4.1 Chromium

As direct probes of thin film antiferromagnetism are rare, the best available information on the nature of the spin density wave (SDW) state, the resulting T_n, and its dependence on thickness and strain come from measurements of exchange bias [73–76]. The shift in the hysteresis loop of the ferromagnetic film coupled at the interface to the AF Cr provides an important, if indirect and necessarily interface-sensitive, probe of the SDW in Cr. Measurements of exchange bias in epitaxial Fe/Cr [73] and permalloy/Cr [75] have shown suppression of T_n with thickness. Some authors have also shown that finite size effects on the SDW state and consequently on T_n occur at surprisingly large film thickness compared to typical metallic magnetically ordered systems [76], with very thick films showing T_n similar to bulk single-crystal Cr, but a strongly reduced $T_n = 130$ K seen even in 25 nm thick films, a thickness large compared to expectations of typical size effects in metals. This also showed the exchange bias was oscillatory with both temperature and thickness, since the nature of the electronic state at the interface changes due to the changing wavelength of the SDW. In support of work done by Sam Bleser *et al.*[[21]] on negative spin Hall angle and large spin-charge conversion in thermally

evaporated chromium thin films, we performed SQUID magnetometry attempts on Cr thin films grown via thermal evaporation on bulk YIG. After extensive measurements to verify T_n, we confirm that SQUID magnetometry cannot resolve the Neel temperature, nor exchange bias, on antiferromagnetic thin films of thickness less than 25 nm on ferrimagnetic bulk YIG subtrates.

4.2 Amorphous $Y_3Fe_5O_{12}$

The magnetic characterization of amorphous yttrium iron oxide thin films (*a*-Y-Fe-O) is presented here. Magnetic properties were measured with SQUID magnetometry and polarized neutron reflectometry. The results confirm that *a*-Y-Fe-O is a disordered magnetic material with strong predominantly antiferromagnetic exchange interactions and a high degree of frustration. This supports a comprehensive investigation of non-local resistance measurements done with Sam Bleser and Leo Hernandez on *a*-Y-Fe-O that shows no evidence of spin transport on micron length scales. [77]

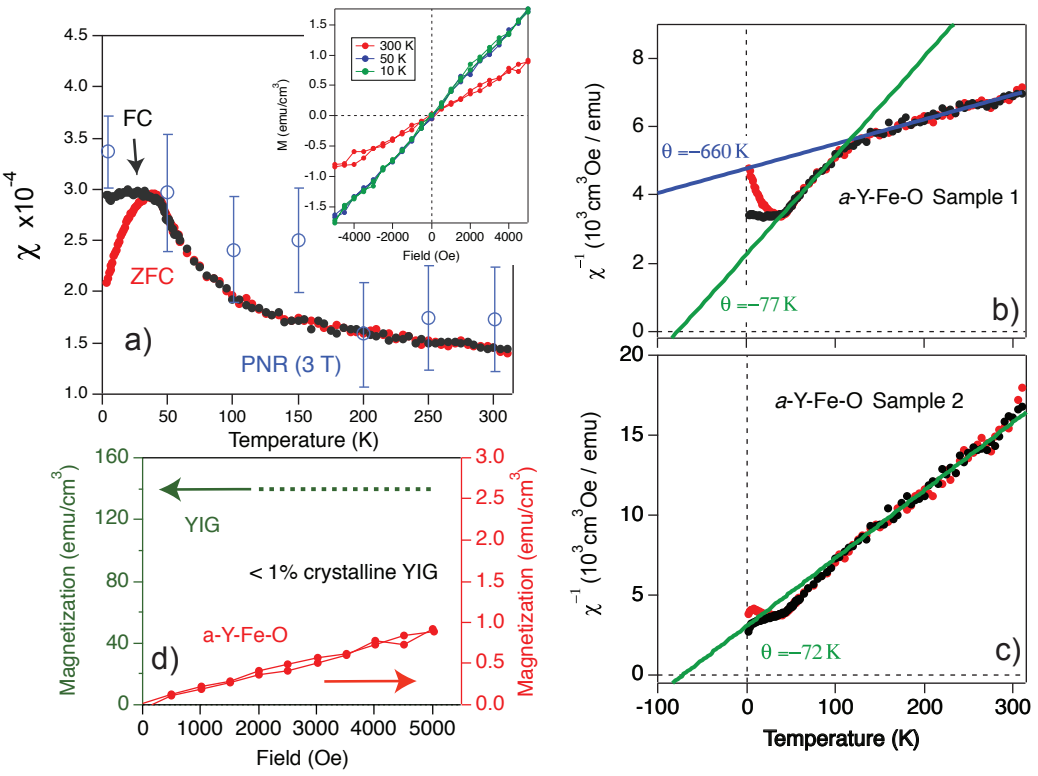

Figure 4.1: Magnetic characterization of *a*-Y-Fe-O with panels ordered clockwise from top left. **a)** χ vs. T for 200 nm thick *a*-Y-Fe-O measured via SQUID magnetometry at 5000 Oe in field cooled (black) and zero field cooled (red) states. The splitting between $40-50$ K indicates a spin freezing associated with the disordered magnetism in *a*-Y-Fe-O. Blue symbols with error bars were measured at $30,000$ Oe via polarized neutron reflectivity by collaborators at NIST. *Inset:* M vs. H at three temperatures shows predominantly linear behavior at modest fields. **b)** Inverse susceptibility, χ^{-1} vs. T for one *a*-Y-Fe-O sample shows two regions with different effective Curie-Weiss parameter, θ. **c)** χ^{-1} vs. T for a second sample grown via the same techniques at a later date shows different magnitude, with only the lower value of θ though with approximately the same spin freezing temperature. **d)** Comparison of M vs. H for *a*-Y-Fe-O (red symbols and right axis) with the saturation magnetization of bulk crystalline YIG (green dashed line and left axis) at 300 K. Even at large laboratory-scale applied field, the disordered system gains a tiny fraction of the moment seen in the ordered material.

4.3 CoGd

The use of current-induced magnetization switching in ferrimagnets near their compensation temperature has been recently explored for use in spintronic devices [78] for the purpose of temperature-driven memory devices. Bulk gadolinium (Gd) and cobalt (Co) are ferromagnets with $T_C = 292K$ and $T_C = 1394K$, respectively. In a CoGd alloy or bilayer, Gd's f electron spin creates a positive local d moment through $f-d$ exchange, which then directly interacts with the Co d moment [79]. This $d-d$ exchange is antiferromagnetic for elements on different halves of the transition series, and in CoGd bilayers creates a synthetic ferrimagnet with competing moment magnitude and direction [80]. At low temperatures the Gd dominates, aligning its moments ferromagnetically to an external field (H_{ext}) with relatively low coercivity and pushes the coupled Co to align antiparallel with H_{ext}. As temperature increases, the Gd's comparatively low T_C leads to a faster magnetization reduction until a compensation point is reached where the Co and Gd moments are equal and opposite. Around this compensation temperature (T_{comp}) the total magnetization reduces to zero and coercivity diverges, creating a stable anomalous Hall voltage state. At higher temperatures than T_{comp} the roles reverse and Co dominates up to Gd's T_C, where AF exchange ceases between the layers.

To probe this switching, synthetic ferrimagnet stacks consisting of the layers $Ta_{3nm}/Pt_{3nm}/Co_{0.5nm}/Gd_{1.8nm}/Pt_{3nm}$ were deposited on silicon in an ultra-high vacuum sputtering chamber for anomolous Hall voltage measurements. The Pt capping layer reduces oxidation and promotes perpendicular anisotropy to overcome thin film shape anisotropy. An initial sample was fabricated and characterized, here referred to as Sample 1, after which more samples were fabricated repeating the same

procedures with an attempt to mimic the exact stack dimensions. One of those samples, named FBL001 in lab data but labeled Sample 2 here for simplicity, was the closest to the original $Co_{0.5nm}/Gd_{1.8nm}$ bilayer thicknesses. To understand the magnetic properties of the stacks and verify T_{comp} for each, SQUID magnetometry was performed for in- and out-of-plane orientations.

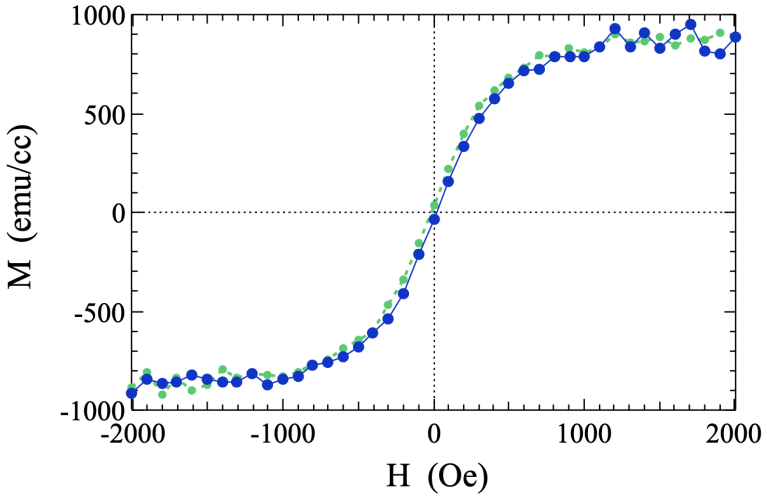

Figure 4.2: Out-of-plane M vs. H on CoGd synthetic ferrimagnet (Sample 1) at 300 K. At this temperature above Gd's T_C the signal is expected to be ferromagnetic cobalt on a diamagnetic silicon dominated background.

In Sample 1 hysteresis measurements show two magnetic contributions; a softer, possibly superparamagnetic component and ferrimagnetic component. At temperatures above the Gd transition temperature we expect to see a normal ferromagnetic Co signal. However, a volumetric calculation of the expected saturation magnetization reveals a lower than expected saturation magnetization, suggesting either a dead layer between Co and Gd or some other mechanism for reducing magnetization. Further, out-of-plane hysteresis (Fig. 4.2) shows a soft, near-zero coercive magnet that suggests mixed anisotropy instead of simple perpendicular anisotropy.

A Brillion function fit to the background converged well but resulted in nonsensical parameters. Regardless of the magnetic complexity, assuming the high-T curve as a background estimate to subtract isolates the synthetic ferrimagnet component around compensation (Fig. 4.3). Magnetometry shows coercivity vs T peaking at a $T_{\text{comp}} \sim 155$ K. This compensation temperature is in line with independent anomalous Hall voltage measurements reported elsewhere [81].

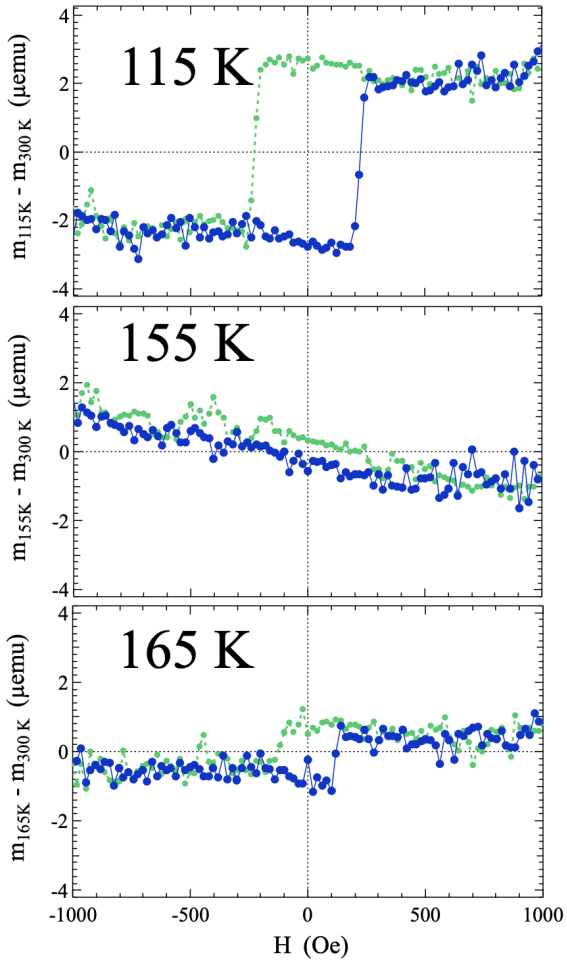

Figure 4.3: m vs. H on CoGd Sample 1 at 115 K, 155 K, and 165 K. Subtracting a high T as a background estimate isolates the synthetic ferrimagnet coercivity with $T_{\text{comp}} \sim 155$ K.

Attempting to recreate the growth conditions, Sample 2 was fabricated with a nominal thicknesses matching Sample 1. However, comparison of SQUID magnetometry reveals these stacks are highly influenced by small changes in growth parameters. A series of hysteresis loops taken at various temperatures reveals more about its magnetic structure (Fig. 4.4). Above Gd's T_C Sample 2 shows a similarly soft, possible superparamagnet with zero coercivity and more perpendicularly anisotropy. Cooling below Gd's T_C, a hysteretic loop grows in coercivity until a $T_{comp} \sim 120$ K, at which second slightly coercive background remains. Approaching this temperature from both directions (Fig. 4.5) reveals a diverging H_C and minimization of M_S, establishing a T_{comp} that again agrees with anomalous Hall voltage measurements performed on Sample 2 [81]. Temperature-dependent magnetization measurements taken with and without field cooling (Fig. 4.6) reveals complex compensation interactions. Two possible ferrimagnet Neel temperatures are present, one at Sample 2's T_{comp} and the other coinciding with Sample 1's T_{comp}.

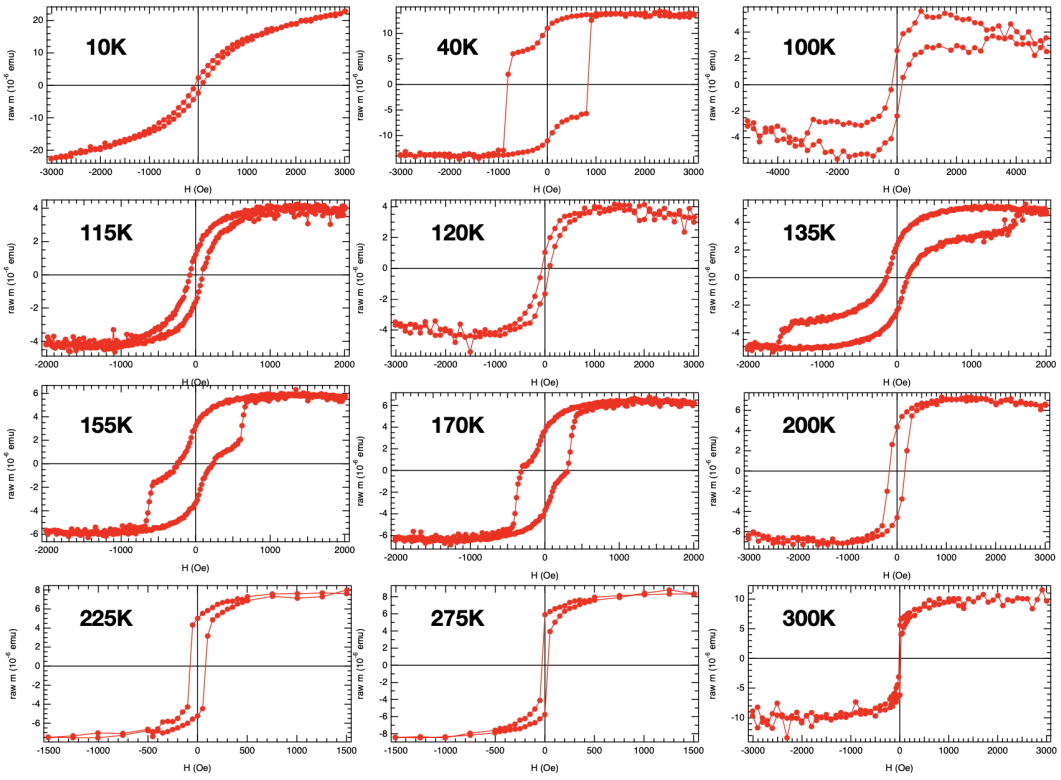

Figure 4.4: Raw m vs. H on CoGd Sample 2 (FBL001) from 10 K to 300 K. Coercivity increases and saturation decreases approaching $T_1 \sim 120$ K, this sample's compensation temperature. A complex background shifts from paramagnetic to diamagnetic around 40 K and a second saturating hysteresis around T_{comp}.

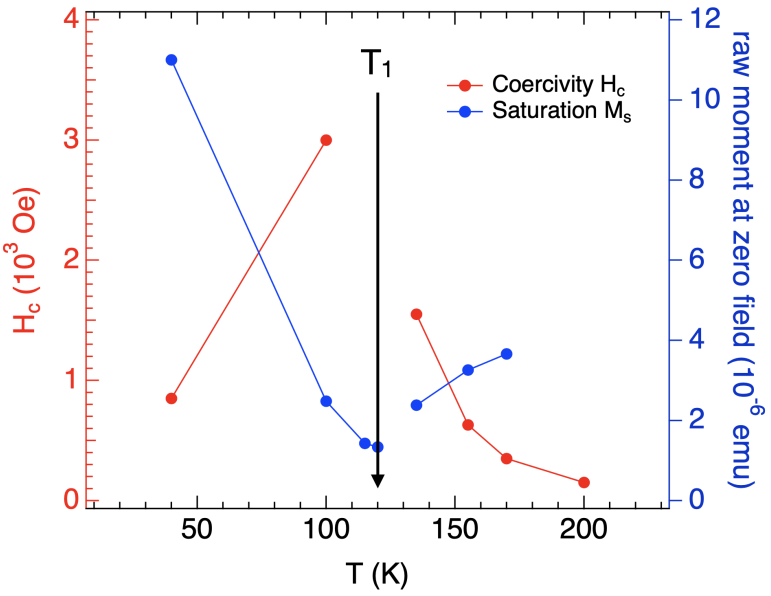

Figure 4.5: H_C (red) and M_S (blue) vs. T on CoGd Sample 2, from the hysteresis curves shown in Fig. 4.4. Coercivity trends towards divergence and saturation minimizes around T_1, this sample's T_{comp}.

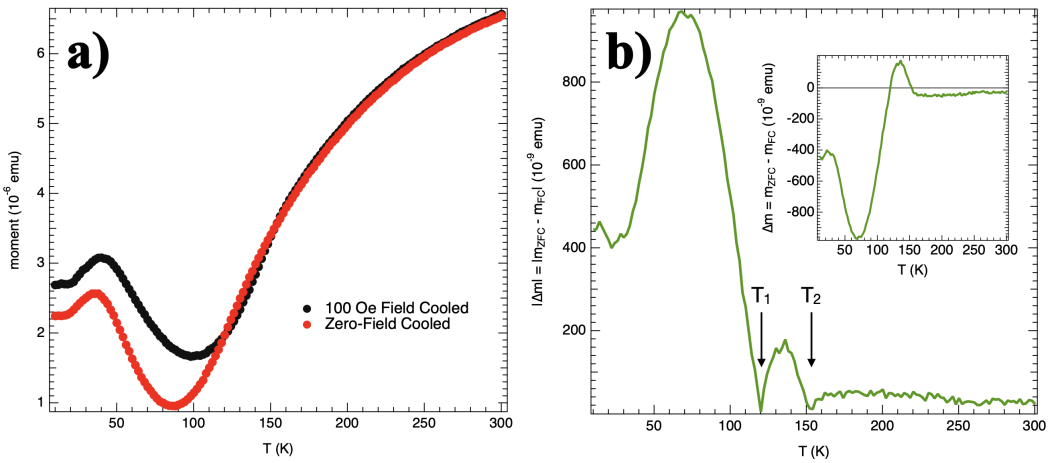

Figure 4.6: **a)** Raw m vs. T on CoGd Sample 2 from 10 K to 300 K. Splitting between field cooling in 100 Oe (black) and zero-field (red) reveals complex interactions including low temperature ferrimagnetic splitting, two transition temperatures. **b)** Magnitude of FC and ZFC splitting shows a single field dependence above $T_2 \sim 155$ K, the same temperature of T_{comp} for Sample 1. $T_1 \sim 120$ K aligns with the T_{comp} established by both the temperature dependent hysteresis and anomalous Hall voltage measurements. Below T_1 ferrimagnetic splitting occurs, complicated by a large changing background signal.

Chapter 5

Thermal, Electrical, and Thermoelectric Characterization of Carbon Nanotube Networks

5.1 Size- and Temperature-Dependent Suppression of Phonon Thermal Conductivity in Carbon Nanotube Thermoelectric Films

5.1.1 Introduction

Thermoelectric energy generation is the conversion of applied heat to useful electricity that occurs in properly engineered electronic materials. Continued improvement in these materials will lead to important applications for power generation and more efficient energy utilization, and could play a vital role in meeting our current global energy challenges [82–86]. The potential of a thermoelectric material is typically assessed using the dimensionless figure-of-merit, $ZT = \alpha^2 \sigma T/k$, where α is the Seebeck coefficient, σ is the electrical conductivity, k is the thermal conductivity, and T is temperature. ZT determines the overall efficiency of thermoelectric energy generation or cooling (via the Onsager reciprocal Peltier effect where current driven through the material generates a thermal gradient) with larger values of ZT resulting in better thermoelectric devices. Current thermoelectric devices are based on materials with $ZT \sim 1$. If this value could be increased to $3-4$, the resulting gains in the efficiency will allow broad application of thermoelectric

devices for energy generation and refrigeration [87], though low-cost, flexible materials could see important use in mobile and wearable device applications even at much lower ZT [88–91].

Regardless of the targeted application, the materials properties in ZT are usually determined by the same physics and difficult to separately optimize. Carbon nanomaterials have dramatic and often tunable thermal and electronic properties [92–94]. These range from some of the highest known thermal conductivities observed for individual single-walled carbon nanotubes (CNT) [95–99], or suspended single-layer graphene [100] to the recently observed unconventional superconducting phase of bilayer magic-angle twisted graphene [101]. Despite k reaching in excess of 3000 $\mathrm{W/mK}$ in single nanostructures, driven by the large contributions from phonons [93, 102], carbon nanotube films can introduce a range of phonon scattering mechanisms that strongly reduce thermal conductivity [103–105]. This allows consideration of such disordered CNT films or mats for thermoelectric energy harvesting applications, and indeed these materials have recently shown promising thermoelectric figure-of-merit [106, 107]. This is largely due to realization of theoretically-predicted large Seebeck coefficients and large in-plane electronic conductivity when doped, and to dramatic reduction of thermal conductivity. This reduction is caused not only by tube-tube junctions, but also by additional phonon scattering from the molecular counterions present to maintain charge neutrality after remote doping of the semiconducting CNT network in ultrasonically-sprayed films [108].

The ability to select specific size and chirality of the CNT is key to the tunability of the Seebeck coefficient and charge transport, and when cleavable polymers are used in this selection and removed completely from the resulting film, both n-

and p-type materials can be produced with very high thermoelectric power factor in the range $\alpha^2\sigma = 700\mu\mathrm{W/mK}^2$ for organic systems. It has been previously demonstrated that k near room temperature is also favorable for these CNT films [109] resulting in $ZT \approx 0.12$. This is among the highest observed for inexpensive, earth-abundant organic thermoelectric materials. This makes a detailed understanding of the contributions to thermal conductivity and the nature of phonon populations and scattering imperative to allow further reduction in k and increased ZT.

In this section measurements of k, α, and σ as a function of temperature from $\sim 77 - 350$ K for two types of semiconducting CNT films for various levels of doping is presented. These films are formed from tubes produced by the plasma torch (PT) method, and from high pressure disproportionation of carbon monoxide (HiPCO), as described further in the Experimental Section below. These very unique measurements of k for low thermal conductivity films of thickness < 100 nm are enabled by micromachined suspended Si-N membrane thermal isolation platforms optimized for thermoelectric characterization of very low thermal conductance nanoscale samples [110–112]. Since k and σ can both be measured on exactly the same sample using these platforms, as shown in Fig. 5.1a), a very accurate assessment of the predicted electronic thermal conductivity, k_e, can be made via the Wiedemann-Franz (WF) law. This shows that one of these films has a near total elimination of phonon contributions to k, and dramatically improved ZT. Improved understanding of this effect could lead to new tunability of phonon thermal conductivity in carbon nanotubes and further increases in thermoelectric performance of these systems.

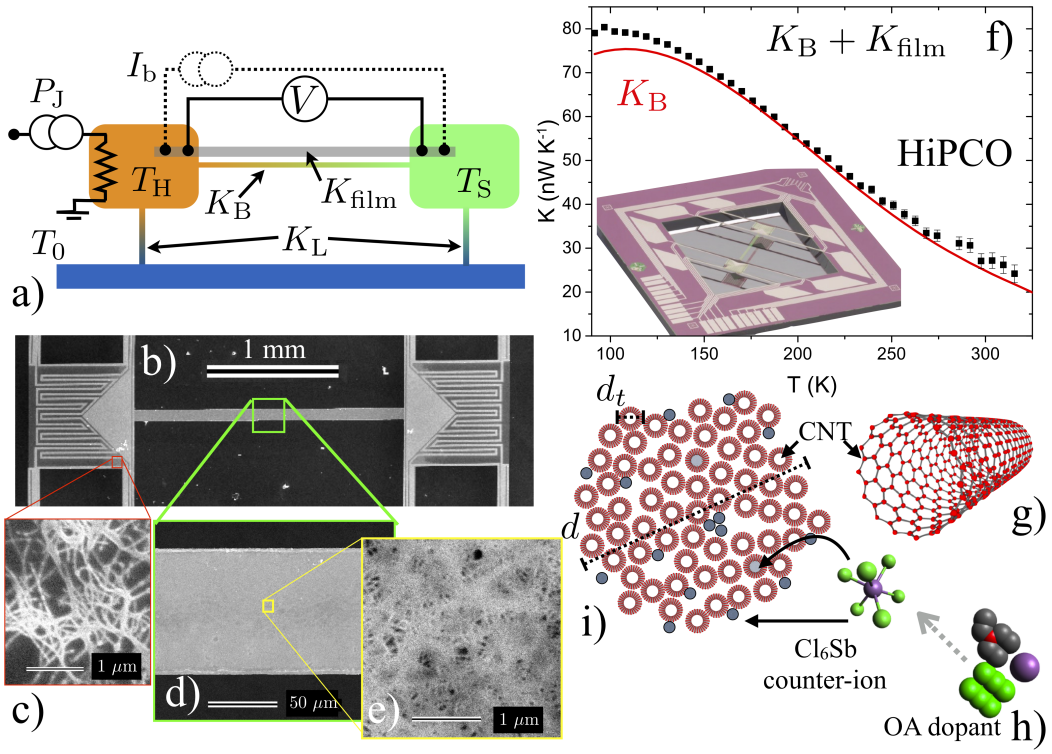

Figure 5.1: **a)** Simple thermal model and schematic of the thermal isolation platform used to characterize CNT thermoelectric films. **b)**Scanning electron micrographs of a platform with a CNT network film. Heaters, thermometers, and leads used to measure k, σ, and α are visible, and described in main text. **c-e)** Higher magnification views of the CNT film demonstrate the morphology of the tube bundles forming the network. **c)** shows the edge of the masked region, where the film is not fully dense. **d)** and **e)** show the dense middle of the sample in two magnifications. **f)** K_B vs. T for one platform before deposition of the film (red line) and after the addition of the HiPCO network demonstrates the small contribution of this film and the low k. *Inset* Optical image shows the full view of the micromachined Si-N platform. **g-i)** comparison of approximate size of a tube bundle, SWCNT, and the OA acid molecule and resulting Cl_6Sb dopant counter-ion, respectively. Panel **i)** also indicates the bundle diameter d , tube diameter d_t, and several possible locations for dopant molecules within the bundle and/or CNT.

5.1.2 Results and Discussion

The micromachined thermal isolation platforms are shown with a schematic heat flow model, Scanning Electron Microscope (SEM) micrographs, and example data in Fig. 5.1. The platforms consist of two Si-N membrane islands suspended by 4 narrow Si-N legs. These two islands are bridged by a narrow Si-N sample platform. Cr/Pt leads patterned on the Si-N provide resistive thermometers, heaters, leads, and four contacts for charge conductivity and thermopower measurements. Joule heating of one island's heater raises that island to T_{H} above the base temperature of the cryostat and Si frame supporting the platform, T_0. Heat flows down the sample bridge raising the second island to an intermediate temperature T_{S}. Four-wire measurement of the voltage drop on the heater in response to known current gives the measured Joule heat, P_{J}. Before a sample is deposited, heat flows only through the Si-N bridge, and the resulting thermal conductance K_B can be determined from the measured P_{J}, T_{H}, and T_{S} via the expression determined from a simple steady-state model of heat flow in the system shown in Fig. 5.1a:

$$K_{\mathrm{B}} = \frac{P_{\mathrm{J}}}{2\,(T_{\mathrm{H}} - T_{\mathrm{S}})} - \frac{P_{\mathrm{J}}}{2\,[(T_{\mathrm{H}} - T_0) + (T_{\mathrm{S}} - T_0)]}. \tag{5.1.1}$$

In practice, we typically use multiple measurements and determine K_{B} from the linear slope of T_{H} and T_{S} vs. P_{J} [110]. Deposition of a thin film, in this case by ultrasonic spray deposition using techniques detailed elsewhere [108, 109], adds a parallel heat conductance, K_{film}, which can be determined by subtracting the background K_{B}. k is then determined from K_{film} using the film geometry.

Fig. 5.1b-e shows Scanning electron micrographs of an example sprayed CNT film on a thermal platform. The overall Si-N structure of the platform, as well as

the lithographically patterned heaters, thermometers and four electrical leads that contact the sample are visible in b). Thermopower measurements use the voltage measured across these leads at each measured ΔT, and a plot of several of these values is linear with a slope that gives the relative Seebeck coefficient $\alpha_{\mathrm{rel}} = \Delta V/\Delta T$. This value inherently includes contributions from the Cr/Pt leads as well as the CNT film, though the contribution from the metal is $\lesssim 5\ \mu\mathrm{V/K}$ at all T, such that thermopowers presented here are dominated by the CNT film [113]. Fig. 5.1b) also indicates two locations where higher magnification shows the density and size of CNT bundles more clearly. Measurement of $K_{\mathrm{B}} + K_{\mathrm{film}}$ vs. T for the HiPCO film is compared in Fig. 5.1f) to the Si-N background K_{B} (shown as a red line). The low k is apparent from the small shift of the total K. We also compare the approximate relative sizes of: **g)** the bundles that form the network of the film, **h)** the nanotubes themselves, and **i)** the OA organic molecule and the resulting hexachloroantimonate (Cl_6Sb) counter-ion involved in the charge transfer required to p-dope the CNT tubes.

Open questions remain regarding the exact nature of the doping process and the location of the counter-ions after exposure of the film to the OA molecule in DCE solvent. The prevailing view is that after doping, the Cl_6Sb counter-ion remains adsorbed to the tube while the by-products are carried away with removal of the DCE solvent [114]. However, our earlier work raised the possibility that these counter-ions could further disassociate [108]. For simplicity, In Fig. 5.1g) we depict the size of the complete Cl_6Sb molecule distributed through the bundle in sites on the exterior, deeper into the bundle trapped between tubes, and also potentially inside the tubes themselves. The exact location of the counter-ions, which could also cluster on the surface of tubes or bundles, is still not entirely understood.

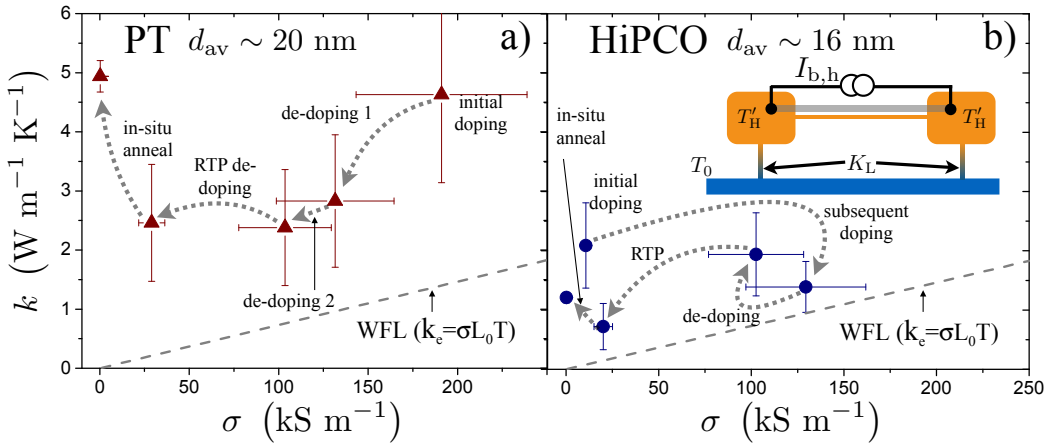

Figure 5.2: Near room-temperature k vs. σ for the **a)** PT and **b)** HiPCO CNT films. These were measured in five different states of doping indicated by the dashed arrows and described in the main text. Electronic contribution k_e predicted by the WF law is shown using the free-electron value of $L = L_0 = 2.45 \times 10^{-8}$ W$-\Omega$/K^2. k exceeding this value indicates phonon contributions, and all doping states of these two films show large k_{ph}. The inset to **b)** schematically shows the method used to anneal the films *in-situ* to achieve the $\sigma = 0$ state.

5.2 Thermal Conductivity as a Function of Doping

In Fig. 5.2 we present near-room temperature values of $k_{\text{tot}} = k_e + k_{ph}$ and σ for both PT (a) and HiPCO (b) films in five different states of doping. The dashed arrows show the evolution of k and σ as dopant is added or removed from the film. We also note the approximate size of CNT bundles that form the film in each figure determined from AFM [109], with the PT tubes forming 20% larger bundles than the HiPCO tubes. THe HiPCO tubes also have smaller tube diameter, $d_t = 1 \pm 0.2$ nm, than PT tubes, $d_t = 1.3 \pm 0.1$ nm. The grey dashed line shows the prediction of the WF law, $k_e = \sigma L_0 / T$, with $L_0 = 2.44 \times 10^{-8}$ WΩ/K^2 the free-electron Sommerfeld value. Though this law has not yet been clearly established for CNT and other organic semiconductor materials [115–119], here we follow convention and

take the WF law as an estimate of k_e. All these near-room T values are higher than WF predicts, indicating that phonons carry significant heat in these films, as expected. The initial doping state (neither film was measured in the undoped state, where earlier measurements suggest a relatively high k with zero σ [108]) for both PT and HiPCO films followed similar exposure to OA dopant.This resulted in much higher k and σ for the PT film, with σ reaching nearly 200 kS/m. We then removed dopant from the film in two different steps, first by a short soak in acetone (labeled "de-doping 1" in Fig. 5.2a), and then by keeping the CNT network in high vacuum for 7 days (labeled "de-doping 2"). At this point we stored the film at room temperature and pressure (RTP) for 412 days. After this long wait for the PT film, σ had dropped by more than 70%, indicating de-doping of the CNT network, while k was basically unchanged. This indicates that some population of dopant molecules had either been removed from the film, or were present but not causing the charge transfer required to dope the tube network. However, in the latter scenario, the molecules scatter phonons in a similar fashion as when they did cause charge transfer. Note that all doping states for the PT film with finite σ roughly follow the trend in k vs. σ expected from the WF law, suggesting a picture of charge and heat transport in the doped PT film where a constant k_{ph} is added to σ-dependent k_{e}.

In contrast, the HiPCO tube network's original doping state was much lower, with $\sigma < 10$ kS/m and $k \sim 2$ W/mK. In this case we performed a second exposure to OA, causing additional doping such that $\sigma > 100$ kS/m. As seen in our previous work on polymer-separated sSWCNT networks where the wrapping polymer remains bound to the CNTs in the network, [108] this doping, which increased σ by $> 10\times$, *dropped* k significantly. After this measurement, the HiPCO film was vacuum de-doped for four days and remeasured (labeled "de-doping" in Fig. 5.2b).

This gave a slightly higher k, though not outside of estimated experimental error, and lower σ. At this point we de-doped this film at RTP for a period of 423 days. This caused an expected drop in σ, but in this case the total k also dropped, to the lowest values measured in this study. Thus for the HiPCO film, all doping states with finite σ except the initial doping state roughly match the trend of the WF law, again suggesting that these values could be explained by a constant k_{ph} added to a σ-dependent k_{e}.

As a final step in the study of the evolution of k with doping, we performed high-temperature in-vacuum annealing by direct heating of the film on the suspended SiN platform. The extreme thermal isolation of the CNT film and its supporting Si-N platform afforded by the micromachined structure allows the sample to be raised well above room temperature either using the Pt heaters on each platform, or simply by driving current through the film itself. Here we chose the latter method, and applied $\sim 200-250\ \mu$A through the film for several seconds and repeated this until the resistance of the CNT network became unmeasurably large. We estimate this power dissipation raises the temperature of the platform to no more than $500-600$ K, which is sufficient to de-dope the film but most likely not large enough to damage the tubes or dramatically change their morphology. We then measured k in this state for each film, and these data points are indicated with the final arrow labeled “in-situ anneal." Here we see that both networks regain increased k, suggesting that driving dopant molecules out of the film or electrically de-coupling them from the tubes reduces phonon scattering. However, the larger tube, larger bundle PT network achieved its highest measured $k = 4.9$ W/mK, while the HiPCO network, with somewhat smaller tubes and bundles, shows only a slight increase to

$k = 1.2$ W/mK, remaining smaller than the initial measured state of this network with incomplete doping.

This apparently persistent change in k for the HiPCO network could have several possible physical explanations. One could imagine that the heating changed the bundle morphology for these smaller bundles such that the number of tube-tube junctions increased and these are the source of additional phonon scattering and reduced k. However, as the estimated maximum annealing temperatures of ~ 500 K are likely not large enough to overwhelm the van der Waals forces bundling the tubes, a change in morphology is unlikely. Another possibility is that the chemical process that causes charge transfer from the OA to the tube, which allows doping, introduces some damage or modified geometry to the tube. One could envision that the resulting (hypothetical) local defect could leave a persistent phonon scattering site. In this picture, the return to high k for the PT network after totally de-doping would seem unusual, but the larger bundle size for that film could prevent dopant molecules from reaching the tubes at the core of the bundle, such that when the dopant is driven off, the total k is dominated by the much higher values of these tubes that remained pristine.

5.3 Thermal Conductivity and Thermoelectric Properties as a Function of Temperature

In addition to the doping-dependence we also investigated T-dependence of k, σ and α from $78 - 325$ K for both films in the RTP de-doped state. We performed these longer data runs after the shorter runs near room temperature to determine the values shown in Fig. 5.2. Fig. 5.3a) compares total measured k vs. T for PT (maroon triangles) and HiPCO (navy circles) films, which show a striking difference in the

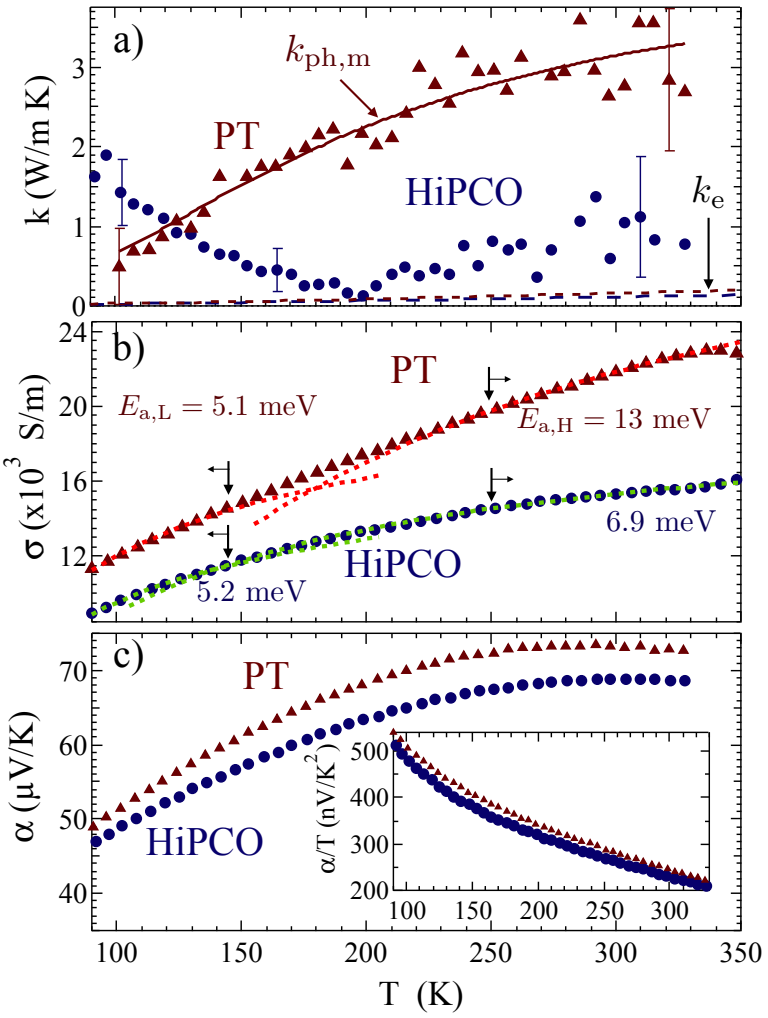

Figure 5.3: Comparison of the T-dependence of **a)** total thermal conductivity, k, **b)** charge conductivity, σ, and **c)** thermopower, α, for films prepared from PT (maroon) and HiPCO (navy) sSWCNT films. The solid line in **a)** is a fit to a simple model of k_{ph} where all T-dependence is driven by changes in c_{ph}. Dashed lines in **b)** are calculated using fit parameters from thermal activation at T ranges above and below the arrows shown. *Panel c) Inset:* α/T vs. T for both films continually decreases.

overall dependence on T. The dashed lines at the bottom of the plot show the prediction of the WF law, $k_{\mathrm{el}} = \sigma L_o T$, based on the measured σ shown in Fig. 5.3b). For the PT film, measured $k \gg k_{\mathrm{el}}$ for the entire measured T range, indicating as expected that phonons dominate k for this film. The trend with T is monotonically increasing and proportional to the dependence of the heat capacity C. The kinetic theory expression for thermal conductivity, $k = 1/3Cv\ell$, with v the average phonon velocity (speed of sound) and ℓ the phonon mean free path, therefore suggests that in this T regime, both v and ℓ are approximately constant. The solid line labeled $k_{\mathrm{ph,m}}$ is a fit of k for the PT film to the expression:

$$k_{\mathrm{ph,m}}(T) = A\left(\frac{T}{\theta}\right)^3 \int_0^{\theta/T} \frac{x^4 e^x}{(e^x-1)^2} dx, \tag{5.3.1}$$

where θ is the Debye temperature, $A = 3Nv\ell k_{\mathrm{b}}$, and the magnitude of the dimensionless integral at each value of $x = \theta/T$ is calculated numerically and used as a function in the fitting. This model cannot separately identify N, v, or ℓ, suggesting only that these are constant with T for this particular CNT network. The model does indicate a value for $\theta \simeq 770$ K. This is in line with expectations of high Debye temperatures similar to diamond and graphite, though the match to the 3D form for specific heat indicates that this disordered CNT network does not act as a lower dimensional system as is the case for single CNTs in certain regimes [93].

k vs. T for the HiPCO CNT network is, in contrast, non-monotonic with increasing T, with an initial drop as T rises from 100 K to $\sim$ 200 K, where the total measured thermal conductivity at 200 K is equal to the estimated electronic thermal conductivity. k then increases with T, though remains significantly lower than for the PT tubes, and also lower than values for previously reported polymer-wrapped

LV tubes at a similar σ. [108] The total k for this CNT network is very low across the entire measured range of T, but the $T-$dependent elimination of phonon k is unprecedented for carbon nanosystems. Again, simple consideration of the kinetic expression $k_{\mathrm{ph}} = (1/3)\, c_{\mathrm{ph}} v \ell$ indicates three potential sources for this drop in k. The first would be a $T-$dependent reduction of phonon modes causing a sharp drop in c_{ph}. As the Debye temperature for modes that could contribute to thermal transport should be much larger than 200 K, this origin seems unlikely. The high Debye temperature also argues against a T-dependent change in the related phonon velocity. We suggest that the most likely cause is a T-dependent phonon scattering mechanism. This could originate in a tube-tube interaction or tube-dopant interaction that develops this unusual T dependence due to thermal expansion of the CNT network, for example. Similarly, a soft inter-tube vibrational mode not capable of carrying heat could be thermally activated and scatter longer wavelength or higher velocity phonons traveling on the tubes.

It is also possible that solvent filling the interior of the tubes could introduce such a dramatic temperature dependence, as solvents such as the DCE used to disperse the OA dopant have freezing temperature near the 200 K inflection point in k. Endohedral solvent filling can dramatically affect thermal conductivity [120, 121] and these changes and related phase transitions are strongly tube-diameter dependent, which could explain the dramatic difference between the PT and HiPCO networks. This difference could also be indirect evidence that the HiPCO process results in a higher number of open-ended nanotubes than the PT process. Electron microscopy could potentially confirm and characterize endohedral solvent filling in our films, though reaching the temperature range of the dip in k_{phonon} could be necessary, requiring challenging and specialized TEM techniques.

Figure 5.3 also compares σ and α as a function of T for the same CNT films in panels **b)** and **c)**, respectively. These are generally in line with previous measurements [122–126], though the T-dependent data shown here was not taken at the optimal doping for peak thermoelectric power factor. As seen previously with tube networks prepared from laser vaporization (LV) tubes, but with similar subsequent processing, σ does not fit a simple thermal activation with a single activation energy across this range of T. Both films can be fit to thermal activation over smaller temperature range at high or low temperature, as previously seen [122]. Fits of this type to the expression:

$$\sigma_{\mathrm{L}} = \sigma_{\mathrm{o,L}} \exp\left\{\left(\frac{-E_{\mathrm{a,L}}}{k_{\mathrm{b}}T}\right)\right\}, \sigma_{\mathrm{H}} = \sigma_{\mathrm{o,H}} \exp\left\{\left(\frac{-E_{\mathrm{a,H}}}{k_{\mathrm{b}}T}\right)\right\} \tag{5.3.2}$$

are shown in Fig. 5.3b), as dashed lines, with the resulting activation energies given in the figure. The PT film has a large separation of $E_{\mathrm{a,L}}$ and $E_{\mathrm{a,H}}$, with values very much in line with previously reported LV tubes. The HiPCO film has a smaller separation, though still does not allow a good fit using a single activation energy. Neither film fits the T-dependence of variable range hopping.

The T-dependence of α is qualitatively similar to previous measurements [122, 124–126], with non-linear behavior across the entire range from $80-330$ K. Since the thermopower is typically assumed to be dominated by the ballistic term [108, 127], this suggests a temperature-dependent energy derivative of the density of states. Both experimental [125, 126] and theoretical studies [128–130] have also considered phonon drag contributions to thermopower in these systems. The clearest indication of the phonon drag contribution is a peak easily resolved by plotting either $d\alpha/dT$ or, as we show in the inset to Fig. 5.3c), α/T vs. T. For both films

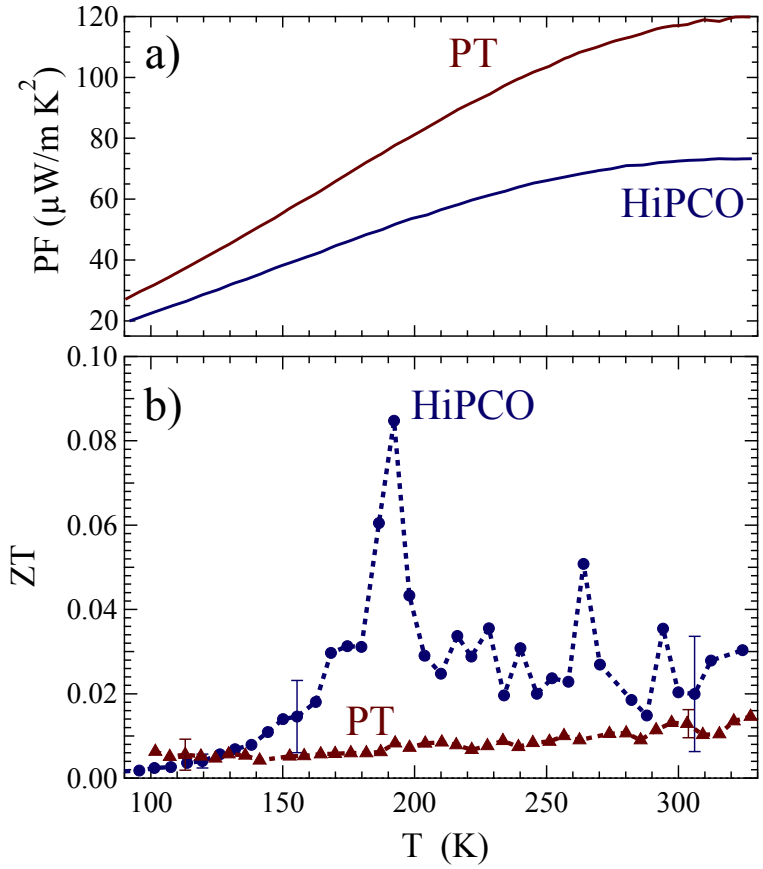

Figure 5.4: **a)** Thermoelectric power factor vs. T for PT and HiPCO films in the RTP de-doped state. **b)** ZT vs. T for PT and HiPCO films in the same doping state. The elimination of k_{ph} near 200 K drives a $>$ 4-fold increase in ZT near this temperature. The HiPCO film maintains higher ZT at all T due to its low k.

this plot decreases sharply at the bottom of our measured T range, leveling off at higher T. This is again qualitatively similar to reports of phonon drag, though measurements to lower T are needed to clearly identify presence of the tell-tale phonon drag peak.

Also presented are the thermoelectric properties resulting from the T-dependent measurements in Fig. 5.4. We compare power factor (PF $= \alpha^2\sigma$), for the two films in Fig. 5.4a). As we previously noted, the de-doped state used for the T-dependent

data on these films is not the optimal doping state for PF, and the values shown here are significantly below the maximum of $700-1000\ \mu\mathrm{W/mK^2}$ observed for these networks [109, 122], and also lower than the maximum observed for this study, where the PT film in the $130\ \mathrm{kS/m}$ doping state reached $\mathrm{PF} = 190\ \mu\mathrm{W/mK^2}$. The HiPCO network's lower α and σ obviously drive a lower PF, which is $\approx 30\%$ lower than for the PT network just below 200 K, and $\approx 50\%$ lower near 300 K. Despite this lower PF, Fig. 5.4b) shows large ZT for the HiPCO film, due to its smaller k at all T. Most striking is the peak in ZT near 200 K, where the phonon k was essentially eliminated as seen in Fig. 5.3a). This value reaches over $ZT = 0.08$, which approaches the current record value for such materials, despite the relatively poor PF. It is very clear that gaining a more complete understanding of the physics and materials issues that drive this T-dependent dip in k can allow further advances in thermoelectric performance for earth-abundant and simply-processed materials.

5.4 Carbon Nanotube Thin Film Preparation

The two films studied here were prepared using a cleavable polymer for separation of the semiconducting single-walled CNTs from two different raw soots: the first prepared using the plasma torch method (PT) purchased from NanoIntegris (RN-020), and the second prepared using high pressure disproportionation of carbon monoxide (HiPCO) originally synthesized at Rice University and provided by Stephen Doorn of Los Alamos National Laboratory. The raw soot is sonicated with the fluorene-based polymer solution, allowing the polymer to selectively wrap and individualize semiconducting tubes. In this study, both HiPCO and PT SWCNTs are initially wrapped with a cleavable H-bonded supramolecular polymer (SMP) named 1,1'-(((1E,1'E)-(9,9-didodecyl-9H-fluorene-2,7-diyl)bis(ethene-2,1-

diyl))bis(6-methyl-4-oxo-1,4-dihydropyrimidine-5,2-diyl))bis(3-dodecylurea). Ultracentrifugation allows removal of tubes with unwanted electronic properties. The enriched semiconducting tubes are ultrasonically sprayed, and the cleavable polymer is completely removed in the solid-state film by soaking the film in a solution of trifluoroacetic acid (TFA) in toluene (10 μL/mL), generating a 68 ± 15 nm thick HiPCO film and a 60 ± 15 nm thick PT film. Complete procedures for the polymer preparation, selection, and removal are presented in a prior publication where we reported σ, k and α only for high doping states near room temperature [109].

Since nanotube/film morphology may play a role in the measured thermoelectric properties, we can point out some of the key differences between the HiPCO and PT films. The HiPCO diameter distribution is centered around 1.0 nm and includes SWCNT diameters as small as 0.8 nm and as large as 1.25 nm. The PT diameter distribution is centered around 1.3 nm and includes SWCNT diameters as small as 1.15 nm and as large as 1.46 nm. Diameter distributions and associated error bars are given in MacLeod et al. [109] Both types of SWCNT films have the cleavable SMP polymer removed so that the dopant molecules adsorb directly to the SWCNT surface. The SWCNT bundle diameters, as measured by atomic force microscopy, are slightly different for the two types of films as indicated in Fig. 5.2.

5.4.1 Thermal Isolation Platform Fabrication and Measurements

Thermal isolation platforms are formed on 4" Silicon wafers coated with 500 nm thick amorphous silicon-nitride (Si-N). After deposition and patterning of Cr/Pt thin film leads, heaters, and thermometers and formation of windows in the Si-N via dry-etching, free standing Si-N structures are formed by removal of bulk Si with TMAH wet-etching. Sample films are selectively applied to the Si-N bridge

linking the two instrumented islands using a shadow mask. Background thermal conductance is measured either before sample deposition or on a witness thermal platform fabricated on the same wafer. Measurements are performed with the Si frame of the platform clamped to a radiation-shielded gold-coated copper sample mount bolted to a liquid nitrogen sample-in-vacuum cryostat. Estimated error as shown in Fig. 5.1f) is calculated on K values from uncertainty on thermometry calibration and fitting *vs.* applied heating power, and is typically on the order of 1%. The eventual estimated error on $k = K_{\text{film}}\ell/wt$ (where ℓ, w, and t are the sample length, width, and thickness, respectively) as shown in Figs. 5.2 and 5.3a) takes into account the subtraction of the two similar values $K_{\text{B}} + K_{\text{film}}$ and K_{B}, and the uncertainty in the sample geometry, which is the dominant contribution to estimated uncertainty on σ shown also in Fig. 5.2. Since our platform allows measurement of σ and k on exactly the same sample, the uncertainty in geometry does not propagate to ZT which depends only on measured film resistance, thermal conductance, and Seebeck coefficient. Estimated error on the relative Seebeck coefficient is of order 1% or better, and as a result the error bars shown in Fig. 5.4b) are dominated by the thermal conductance background subtraction. Further measurement details are available elsewhere [110–113].

5.4.2 Conclusion

In summary, we presented thermal conductivity, thermopower, and charge conductivity on two disordered films of semiconducting single-walled carbon nanotubes. Our techniques, focused on a suspended Si-N membrane thermal isolation platform, allow direct comparison of electrical and thermal contributions to thermal conductivity. Near-room-temperature values of k for a range of doping levels, in-

cluding the entirely de-doped state, are dominated by phonons as always previously observed for CNT systems, and the film formed from PT tubes shows T-dependence of k that matches a simple model with fixed phonon velocity and mean free path and a 3D Debye specific heat with $\theta = 770$ K. In contrast, the film produced from HiPCO tubes has a lower and non-monotonic k that approaches the estimated k_{el} near 200 K. This drop in k drives a large increase in ZT in a narrow temperature range, suggesting further dramatic advances in thermoelectric performance of CNT systems are possible if the mechanism of this reduced phonon transport can be understood and manipulated. Ongoing exploration of thermal properties of additional CNT networks using these techniques are key to these advances.

5.5 Thermal and Electric Conductivity Measurements of Freestanding Carbon Nanotubes

5.5.1 Freestanding CNT Methods

As explored in the previous section, carbon nanotube thin films show promise for organic thermoelectric regeneration applications. The introduction of phonon scattering sites has a large effect on the thermal conductivity, which we've shown can dominate the increase in effective zT [131]. Sample fabrication via ultrasonic deposition onto measurement platform surfaces innately creates an interfacial boundary layer that may impact its thermal properties and network morphology. Further, the promising application for these materials in form-fitting, low-cost thermoelectrics motivates an exploration into the development of free-standing, highly-enriched s-SWCNT thin films. As purifying selective chiralities of s-SWCNT (as detailed in 5.4) is time intensive and costly, pre-enriched CNT soot was used as a

foundation for the development of experimental processes. Without undergoing enrichment, this soot contains numerous styles of carbonaceous molecules including fullerenes, single-walled, and multi-walled CNT of both semiconducting and metallic species. Collaborators at NREL developed a method for drawing the CNT-rich solution against a removable filter, producing freestanding CNT (f-CNT) networks less than 10 μm thick. We investigated the possibility of isolating these freestanding semi-purified films on our suspended thermal isolation platforms. For standard measurements electrical and thermal contacts are made by directly depositing onto the platform's electrical leads, so measuring freestanding films introduced a new set of challenges that required an extensive iterative testing process.

Transport measurements were performed on modified membrane platforms specialized in the measurement of bulk sample properties, as there is no bridge between islands, and the amorphous silicon nitride thickness increased four-fold to 2000 nm to better handle the stresses involved during sample application. A number of methods, detailed in the following sections, were explored to electrically and thermally adhere the samples to the bulk devices while maintaining the electrical passivation necessary to accurately measure lead thermometry. In addition, methods for optimizing the sample geometry were developed and provided a cursory view of the electric, thermal, and thermoelectric properties of these highly-disordered, carbon-rich films. These intriguing results enhance this proof-of-concept that such an endeavor would be feasible on our devices.

5.5.2 Experiment

Purified buckypaper consists of a $2/3$ to $1/3$ ratio of semiconducting and metallic SWCNTs. After a long acid-based purification, the SWCNTs are filtered and

washed thoroughly to produce a paper that peels off of the polytetrafluoroethylene (PTFE) filter. The resulting buckypaper at this stage is estimated to be 50% SWCNTs and 50% amorphous carbon, with potentially some residual Ni/Co catalyst of up to $1-2\%$. The paper is then flash annealed to rapidly burn off the amorphous carbon, producing a buckypaper that is >90% SWCNTs, commonly in the range of 95% SWCNTs. The exact stage of the purification process the measured films had been taken through is unknown.

It is also unknown if this is a filtered paper or a filtered/annealed paper. Filtered papers are often in the range of $\sim 5-10$ μm thick, while the filtered/annealed papers are $\sim 2-5$ μm thick. Verification of the film thickness in its free standing form was difficult to measure. Results from attempts at atomic force microscopy (AFM) were inconclusive due to the magnitude of the step size and movement of the film during scanning. To image a cross-section of the film, scanning electron microscopy was performed on the buckypaper. A section was sandwiched between two silicon chips cleaved along a similar plane to allow edge-on imaging, producing a rough estimate of 3.6 μm $\pm$1.0 μm for the sample thickness (Fig. 5.5d). Three samples taken from different locations of the same buckypaper were measured, labeled F1-F3 (Fig. 5.5f-h).

The freestanding CNT film appeared brittle in multiple sections, each with the general shape and morphology of the filter used in fabrication. Samples with geometry suitable for mounting on the isolated islands of our bulk thermal chips were required. The distance between islands is 1000 μm and the islands dimensions are 800 μm $\times$800 μm. Samples measuring roughly 800 μm wide and 2000 μm long comfortably span both islands and the intervening distance. A few techniques were tested for generating the preferred sample shape. Ripping the films with tweez-

ers produced samples with inconsistent sizes and jagged edges, as seen on sample FC1 (Fig. 5.5f), and the metal in the tweezers could impregnate impurities into the film. Producing a rectangular sample geometry optimized to match the shape of the platforms is preferred for accurately measuring dimensions for conductance to conductivity calculations and reducing off-axis thermal gradients. This is achieved by cleaving portions of the bulk material. First, glass slides are cleaned with a solvent with decreasing molecular size (acetone, isopropyl alcohol, then methanol). The section of the film to be cleaved is flattened between the slides, and the top slide is positioned to the preferred distance such that the final width of the film is uncovered (Fig. 5.5e). The top slide is angled at 45 degrees to create a knife-like edge. Pressure is applied out-of-plane to the sample with the top slide, accompanied by a gentle side to side oscillation to promote separation, allowing the cleaved portion to be easily removable with a gentle tug. This method is repeated on each edge until the appropriate length and width geometry is generated for the sample. The final result is a general rectangular shape that fits perfectly on our devices (Figure 5.5g,h).

5.5.3 Application Methods

In order to achieve thermal and electrical connection with the measurement leads on the islands while not shorting to the thermometry and heating leads, we needed to electrically passivate certain portions of the islands. The passivation was achieved with $90-110$ nanometers of Al_20_3 deposited via electron beam physical vapor deposition using a current of $65-80$ mA across the tunsten fillament to maintain a growth rate of 1.0 Å/s. Vacuum pressure was steady $\sim 3\times10^{-7}$ Torr, and raster parameters set as follows: pattern PP03, gain 8, speed 54, spin2, and rate

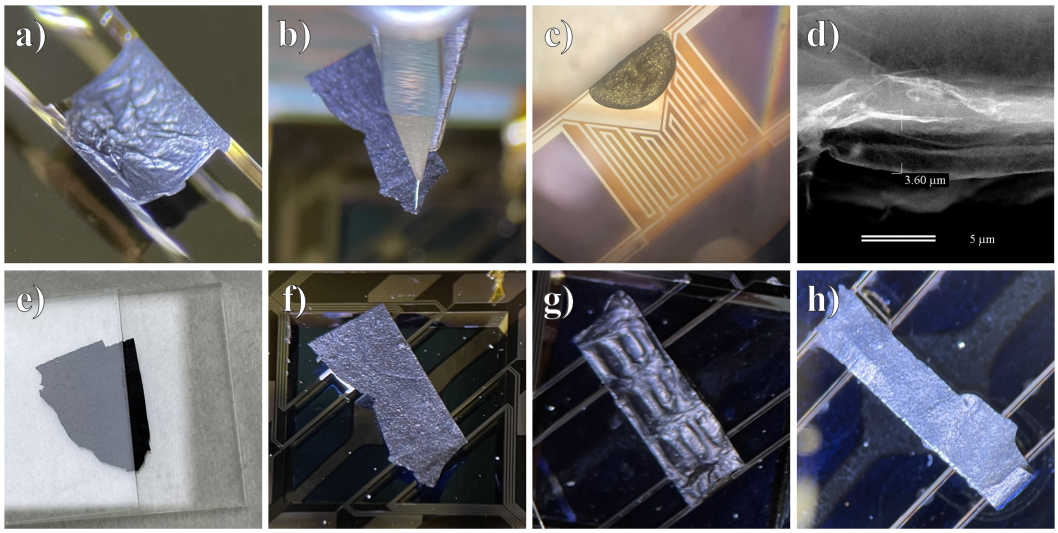

Figure 5.5: **a)** Rapid drying of conductive paints warps the suspended platform. **b)** Wire bonder 'crane' method for applying CNT film to wet adhesive. **c)** Silver paint on Al_2O_3 passivated island for solvent 'reactivation' method. **d)** Scanning electron microscope cross section of the CNT film. **e)** The glass slide cleaving method produces optimal sample geometries. Because FC1 **(f)** was torn from a corner section with tweezers the geometry requires assumptions in the thermal gradients and transport paths. FC2 **(g)** and FC3 **(h)** used the glass slide method.

gain. Once passivated, conductive paint could be applied to achieve thermal and electrical connections to the islands while electrically isolating the thermometer leads.

Various techniques were tested for carefully applying quick-dry silver paint to the islands. Small paintbrushes did not provide adequate levels of precision, and wire bonder wire with a small looped end proved too difficult and delicate to properly control. Instead, small-gauge copper wires separated from a braided electric cable and bent into a looped hook were found to have the appropriate mix of diameter, malleability and rigidity for precisely dripping paint onto the platform. Dipping the wire hook into the adhesive paint created a small ball around the tip. Using the microscope on a wire bonder and a steady hand, a droplet of adhesive could quickly

be applied to each island, coating them with flash silver paint. However, the small size of droplets on our devices meant that the paint dried extremely quickly, such that by the time the film was ready to be placed onto the adhesive, the top surface of the adhesive was already mostly set. By applying the film quickly enough, it was possible to adhere it, creating an electrical connection and full passivation of the islands. However, when set out overnight these devices would be broken by morning. We found that while the top layer of the silver paint dried quickly, the remainder would remain liquid, and as the solvent not exposed to air evaporated, it would warp the associated islands (Figure 5.5a). While the platform legs are structurally robust under strain, the sheer stresses experienced during warping eventually breaks one or more legs.

So while using quick-drying conductive paint allowed for rapid application and adhesion of the film, the warping of the islands results in breaks in the attached legs, severing electrical connections due to torsion and/or shear stresses in unexpected directions. Attempting this procedure with conductive copper paint yielded improved but similar results. It was eventually found that silver paint with a slow-drying solvent would set more uniformly, reducing structural stresses on the island legs, with the added benefit of additional time between the applications of silver paint and the f-CNT. It was seen in tests using the slow drying conductive paint that a liquid surface would last roughly ten seconds before adhesion issues began to occur. However, this was still too short of a time to reliably apply the paint and set down the f-CNT film in its proper position. With time and practice it may be possible to master the necessary sequence of events, but on devices with pre-measurements completed the failure rate is too high to claim real reproducibility. A separate wire bonder 'crane' method was developed to mitigate these application issues.

5.5.4 Wire Bonder 'Crane' Method

Sample FC1 was mounted via the crane method. In a test to determine the possibility of wire bonding directly to the f-CNT film, it was observed that the wire bonder would simply punch through the film and bond onto the surface below. Testing a number of surfaces revealed that a bond could not adhere to the green PCB polymer on the sides of a mounting board. Thus, by placing a CNT sample onto PCB in the exact orientation of its final position on the device and wire bonding it to one corner, the bond could go through the film and flatten against the PCB but not adhere to it. By carefully raising it back up, the wire bonder provided enough support to lift the entire sample (Figure 5.5b). Excess wire could then be pushed through the wire bonder to create a dangling CNT sample on a fine movement crane, not unlike an arcade claw game. Using the conductive paint wire loop method to apply slow-drying silver paint to the suspended membranes, the CNT film could then be lowered directly into its position within seconds with the aid of the wire bonder microscope. Letting the film down onto the paint and allowing sufficient time for the paint to solidify, then gently raising the wire bonder head allows the wire bonder head to move easily, without the moving the adhered film. Best results were achieved by first doing a trial application without paint to ensure perfect sample alignment on the islands, and taking great care when raising the wire bonder head after application. An alternative technique involves applying the film to the adhesives and then 'feeding' the wire out after a few seconds. It is also possible to use tweezers to gently apply pressure to both sides of the island to assist in complete adhesion.

5.5.5 Saturating in Solvent to Reactivate Paint Method

One of the ultimate goals of this experiment was to determine the thermal conductivity, electrical conductivity, thermopower and heat capacity of the thermal films *in-situ* during the same experimental run. To determine the heat capacity, the addenda background heat capacity of the device and the silver paint needed to be found. It was initially seen that the heat capacity of the silver paint was much greater than that of the freestanding film. Consequently, a new method of adhesion was developed to attempt to find the heat capacity of the entire addenda before applying the sample. Samples FC2 and FC2 were mounted via this solvent method. Full thermal measurements of the individual islands were taken before passivation, after passivation, and after application of dried silver paint blobs without carbon nanotubes applied. Because the silver paint heat capacity is so much higher than that of the nanotubes, and because the exact amount of silver paint used was not reproducible, the variance in the heat capacity between trials was too great. As such, it was necessary to use the exact same silver paint for each trial.

A number of experiments were done to determine the best solvent to reactivate the silver paint. The solvents experimented with were acetone, isopropyl alcohol, toluene, and a proprietary flash paint solvent. The solvent and acetone were the best at reactivating the top layer of the paint, however the paint near-instantaneously resolidified after their application. The isopropyl alcohol and toluene were slightly successful, but their effects were too localized. Thus, because the film application needs to be performed so quickly, the only effective method to get films onto the platforms was to soak a section of the film in solution (i.e. solvent or acetone, etc), and apply the saturated sample to the paint-covered islands. This worked re-

markably well with all of the solvents tested, however with the acetone and solvent, flecks of silver paint were scattered in the solution. Once dried, the paint flecks could be optically seen along the length of the device, and would short parts of the leads. This was not observed with isopropyl alcohol, which was the least effective at reactivating the adhesive. Modification of the thermal and electrical properties of the sample are therefore most likely attributable to the diffusion of these highly-conductive silver impurities. As discussed in the results section below, this method is no longer suggested due to these issues.

To reduce the ratio of heat capacities of the addenda to the small sample, methods for reducing the amount of silver paint on the islands were developed. With sufficient practice, the wire loop was able to adhere a minimal amount of silver paint to only the front leading edge of the triangular island lead (Figure 5.5c). Further, with enough accuracy and practice, one might be able to use the paint application and wire bonder crane method to adhere a CNT without first passivating the device with Al_2O_3. A transition to better understanding the efficacy of the heat capacity experiment itself means this was not attempted, and this method warrants further investigation.

5.5.6 Results

For each of the three samples, a complete temperature-dependent measurement of thermal conductance, electrical resistance, and thermopower was taken in vacuum from 80 K to 366 K in 2 K steps. While maintaining vacuum, a subsequent runs were performed over most of the same range with a larger step size. Fig. 5.6 shows the results of the initial and second run for the sample. For FC1, mounted via the wirebonder crane method, a large initial thermal conductance of ~ 20 nW/K

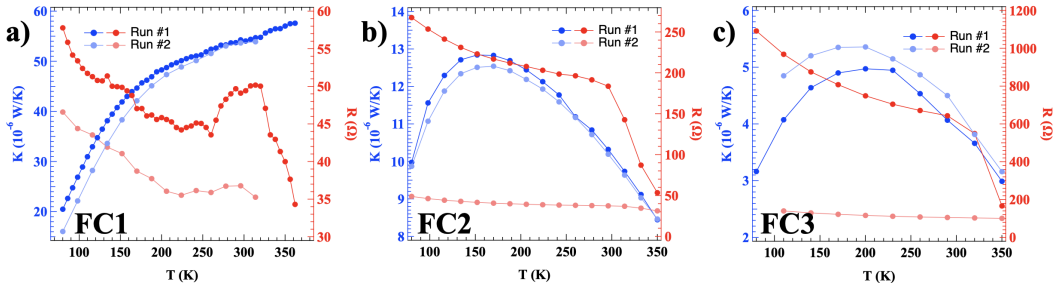

Figure 5.6: Thermal conductuctance (blue) and electrical resistance (red) for **a)** FC1, **b)** FC2, and **c)** FC3. For each sample, two measurement trials were repeated back-to-back (Run #1, Run #2). Each sample sees both a significant decrease and change in temperature dependence of the electrical resistance between trials. Changes in thermal conductance between trials is minimal.

increases across the entire temperature range tested to $\sim$ 57 nW/K, over which the electrical resistance decreased significantly, from 58 Ω to 34 Ω, and with large variability in temperature dependence. The second measurement sees a slight decrease in thermal conductance, most noticeably at lower temperatures. However, the film resistance decreased greatly over the entire temperature regime, while maintaining roughly the same trend, suggesting a significant electron transport carrier change between the two runs that minimally impacted the thermal conductance.

For FC2 and FC3, mounted by the solvent method, measurements were taken using the same conditions as FC1. FC3 has a significantly reduced amount of silver paint in an attempt reduce addenda heat capacity. Both FC2 and FC3 results are similar to each other, albeit with different magnitudes (Fig. 5.6 b,c). The thermal conductance for both are greatly reduced from FC1 values at all temperature ranges, and the temperature dependence highly modified. Instead of exhibiting a continual increase at all temperatures, the thermal conductance in FC2 peaked around 160 K and decreased as temperature increased further, down to a minimum thermal conductance of roughly 8.4 nW/K at 350 K. FC3 showed a similar trend, peaking at

a slightly higher temperature $\sim$ 200 K and even reduced conductance of $\sim$ 3 nw/K at the highest measured T. Similar to FC1, a subsequent second run showed the same temperature dependence to the first run, with only a slight shift in magnitude. The film electrical resistance of FC2's first run started roughly five-fold higher than FC1, at 267 Ω. The temperature dependence of the electrical resistance followed a similar trend to FC1, decreasing over the temperature range until 300 K, at which point the resistance decreased rapidly, going to 53 Ω at 350 K. The second run's electrical resistance then mapped nearly identically onto the second run of FC1. FC3's resistance follows an identical pattern as FC2, but with much higher values.

Notably, while all samples were from different regions of the initial film and received significantly different application methods, all second runs saw an increase in electrical conductivity to a nearly identical temperature dependence. However, the thermal conductance maintained a large difference in temperature dependence between the two methods. Because the shift in thermal conductance between runs was minimal for both, while the electrical resistance decreased greatly, thermal conductivity is expected to be largely phonon-driven. As seen in our previous work [131], the introduction of phonon scattering sites that do not contribute to the film's electrical profile may play a role in greatly decreasing the film's thermal conductivity. As an aside, the passivation layer appears to increase the thermal conductance of the membrane legs more than five-fold.

A large ejection of particles due to outgassing in vacuum or annealing during thermal cycling may contribute to the shifts between runs. While electrical conductivity measurements using the expected thickness of 3.6 μm gives large error, the values are nonetheless reasonable compared to other studies on buckeypaper. [132].

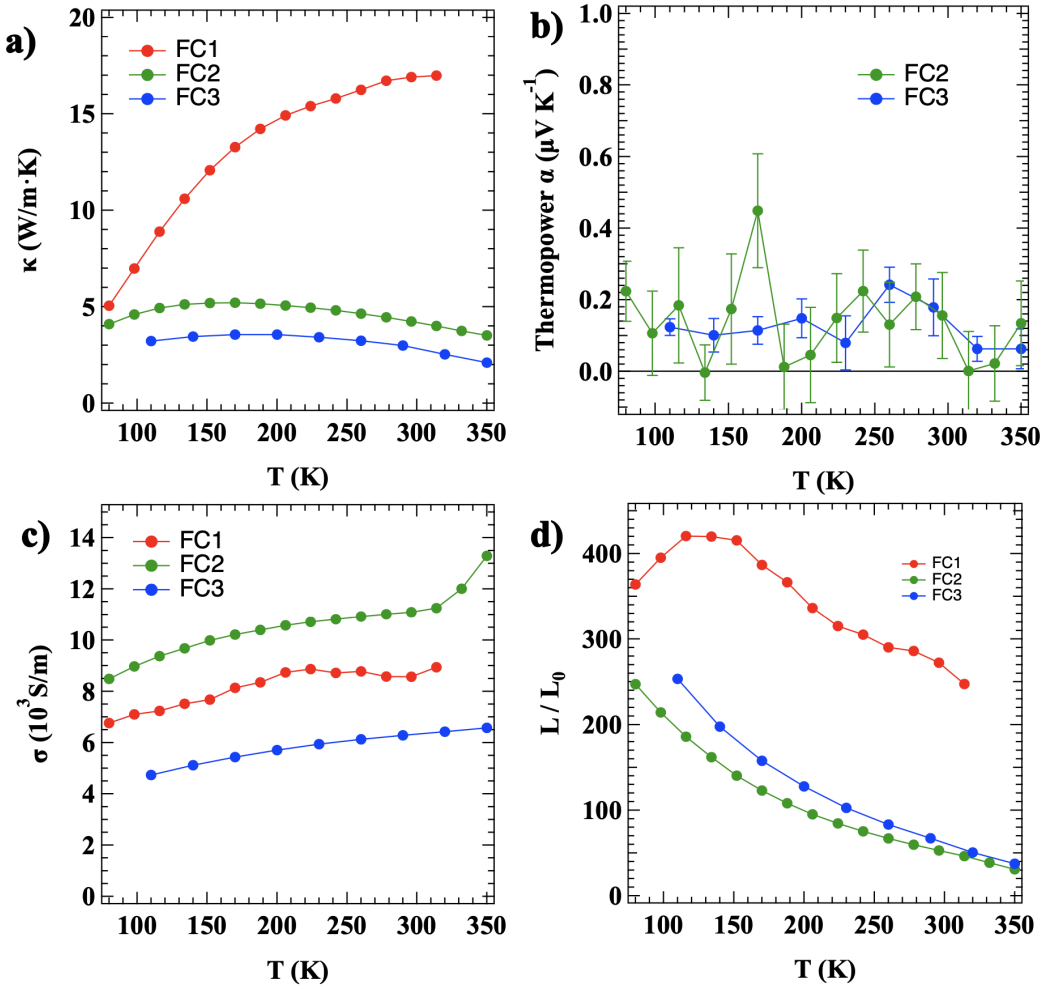

Figure 5.7: **a)** Thermal conductivity, **b)** thermopower, **c)** electrical conductivity, and **d)** Lorenz-Sommerfeld number ratio vs. T for the three freestanding CNT films. While each film has a massive phonon contribution to thermal transport, a discernible modification in κ can be seen between the two mounting methods. As expected, the solution method introduces scatter sites that decreases phonon contributions. FC1 thermoelectric voltage vs. ΔT data had no discernible slope and was omitted.

Finally, the conductivity decrease in vacuum does not necessarily indicate that the sample out-gassed impurities due to not being previously annealed. Adsorption of water and/or oxygen to the SWCNTs occurs for samples stored in air for any appreciable time. Those adsorbents make the SWCNTs p-type and will slowly

desorb in vacuum over time. A combination of these two potential dopants could result in the observed conductivity effects. While our samples were stored in a dehumidifying sample storage box to limit these effects, these effects cannot be discounted without the use of a nitrogen dry box.

Future work should focus on generating a 100% s-SWCNT film, preferably PT/PFPD samples, that gives us the highest TE power factor. Due to the high thermal conductivity seen in the samples, we would like to repeat these experiments on another buckypaper with known fabrication history and morphology. This will allow us to better characterize the geometry and density to obtain more accurate conductivity measurements.

Chapter 6

Micro- and Nanocalorimetry for Sensing and Materials Physics: Time-Dependent Measurements on Suspended Membranes

6.1 Microcalorimetry for Aerosolized Viral Detection

We explored the development of micromachined thermal detectors capable of detecting tiny depositions of energy from chemical reactions or physical processes in nanoscale systems. These detectors use a minuscule platform with integrated heaters and thermometers, which allows measurements of the temperature change when a droplet interacts with its surface. If an appropriate antibody or binding target is placed on the platform, the resulting exothermic reaction can indicate the presence of a given target. The preliminary work shown here focused on optimizing our thermal isolation platform, developing appropriate measurement techniques and software, and characterizing the thermal properties of these new tools. Later work with DU collaborators will focus on integrating antibodies and demonstrating viral detection.

6.1.1 Introduction

The recent global pandemic clarifies the pressing need for better tools to detect the presence of viruses, particularly those carried in aerosols or larger droplets, and

the environmental detection of such pathogens presents a set of challenges requiring interdisciplinary collaboration. Real-time detection of virus particles spreading in an environment could provide powerfully specific information that would supplement public health measures. The so called "lab-on-a-chip" approach to virus and pathogen detection, [133–135] where micro- and nanotechnology tools allow for fine-scale physical or chemical detection of threats, offers a range of potential routes toward this goal. Many of the existing efforts in the field focus on microfluidics, replicating larger scale wet chemistry on the small scale. Open-chamber micromachined suspended silicon nitride (Si-N) calorimetry sensors have been developed specifically for chemical and biochemical reaction measurements, and are able to resolve power dissipation in controlled conditions down to 28 pW [136], while sensors utilizing modern commercially-available thermistors can achieve resolution down to 270 pW, enough to study cellular metabolic activities. [137].

To this end, we capitalized upon our lab's expertise in micro- and nanocalorimetry sensing and materials characterization [138–140] to explore using micromachined thermal isolation platforms as an inexpensive, passive thermal sensor that could operate in ambient conditions. Direct methods of viral detection often require one or more chemically reactive processes, including viral DNA binding to target-specific fluorescent probes, dyes with highly optimized primers, or probing antigens blotted on membrane surfaces with a target-specific antibody [141]. An often overlooked byproduct of these binding reactions is the small release of exothermal energy. The heat released when an airborne virus binds to a target or antibody enables identification of the viral presence through sensitive calorimetry. Such a calorimeter in an open-chamber configuration would require the temporal resolution to detect fast-binding reactions, high thermal sensitivity to resolve the fewest concentration

of reactions, and the stability to differentiate between exothermic detection reactions from aqueous sample evaporation and environmental perturbations.

A micro- or nanocalorimeter consists of a sensitive thermometer fabricated on a platform with a small heat capacity C, and thermally anchored to a temperature bath at T_0 by a thermal conductance, K (Fig. 6.1a). Any energy, E, absorbed by the heat capacity causes the temperature to jump by $\Delta T = E/C$. With suitably small C and sensitive thermometry, detectors of this type can measure single photons and other tiny energy inputs [142–144]. We hypothesize that if a suitable artificial antibody or other binding target is plated on the calorimeter platform, a virus-carrying aerosol or droplet landing on the platform might bind and produce an exothermic heat release with a measurable temperature rise, indicating the presence of the virus.

An example thermal isolation platform is shown in Fig. 6.1c. Here two suspended Si-N structures with integrated micromachined thermometers and heaters (each essentially a calorimeter as shown in panel (a)) are connected by a narrow Si-N sample platform. Adding a thin film or nanostructure to this platform allows measurement of the heat flowing in the structure. These platforms have proven to be powerful tools to measure thermal and electrical conductivity, as well as various thermoelectric effects in thin films and nanostructures [108,110,112,131,145–148]. However, due mostly to a lack of instrumentation and software, heat capacity measurements have never been added to this suite of abilities.

While our group has extensive experience using modified calorimeters to measure nanoscale heat transport, our focus has been on the thermal conductance K shown in Fig. 6.1b, which is a steady-state measurement that does not require temporal resolution, as described in Appendix A. Nanocalorimetric virus detection therefore required the development of higher resolution time-dependent thermom-

etry. Furthermore, to be useful for detection applications, the thermometry must maintain time and temperature resolution even when the nanocalorimeter is held at ambient atmospheric conditions. This regime has never been explored, as high vacuum conditions are required to control and isolate the heat flow in the tiny structure and achieve cryogenic temperatures without condensation.

Thus there are two motivations for this experiment. The first, described here in Section 6.1, is to demonstrate a proof-of-concept of our thermal platforms as an aerosol exothermic reaction detection device in atmospheric conditions for future coupling with viral detection methods. The second, explored further in Section 6.2, is to gain more experience in time-dependent thermometry in the pursuit of adding the capability to measure heat capacity of nanoscale samples to our existing thermal measurement platforms and advancing an already highly unique capability not available anywhere else in the world.

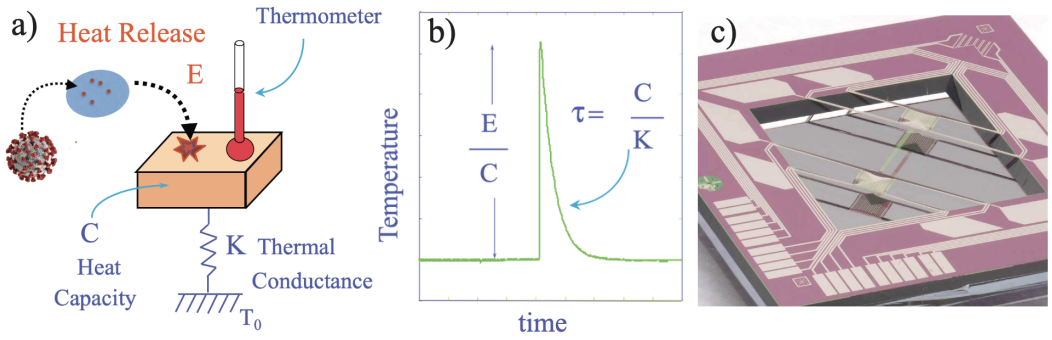

Figure 6.1: **a)** Schematic view of micro- or nanocalorimetric virus detection. Energy deposited by spike protein binding generates a temperature change, as shown in **b)** which is is measured with a sensitive thermometer integrated in the nanomachined structure. **c)** Example thermal isolation structure used to measure thermal properties of nanostructures.

6.1.2 Experiment

A SRS SIM900 Mainframe houses switching and resistance modules and acts as the hub for instrumentation and computer communication. SRS SIM 924 Octal Four-Wire Multiplexers are digital-to-analog switches, allowing us to link instrumentation to specific cryostat sample channels, such as individual 4-wire thermometer or heating element leads, and they are controlled by computer via remote GPIB interface. Each instrument is designated a GPIB channel to dictate computer communication priority, and the multiplexer port and channel switching creates the physical sample-to-instrument lead connections. Steady state resistance measurements are done by a SRS SIM921 AC Resistance Bridge, which functions similar to a lock-in amplifier resistance measurement as the low excitation power minimizes self-heating errors for accurate thermometry. A frequency-locked 1 mV AC excitation voltage dropped across a 2 kΩ resistor (chosen for being closest to the membrane Pt thermistor resistance values) provides an AC current with rms amplitude of 0.5 μA, and is held constant at all temperatures to keep ohmic dissipation proportional at low temperatures. The in-phase component of the measurement is recovered and filtered with a low-pass filter, and a running average is calculated over a set time constant of 1 second. While this works extraordinarily well for our steady state measurements, for time-dependent heat dissipation, temporal resolution down to the millisecond range is required.

For heat dissipation measurements, a Keithley 2182a Nanovoltmeter and Keithley 6220 Precision Current Source in a 4-wire configuration was used to measure the changing resistances. The 6220 applies a DC bias current to the chosen Pt thermometer on the suspended Si-N island (Fig. 6.2), where $I_{\text{bias}} = 1$ μA is often

used for the best balance of sensitivity and self-heating. The 2182a nanovoltmeter senses and records the voltage across the Pt resistor. Because the 4-wire I - V junction is located on the suspended island, sense lead current is negligibly small and not an accountable source of heating. To achieve the fastest temporal resolution, the 6220 and 2182a measurement parameters are set remotely using custom written NI Labview software and initiated such that I_{bias} heating equilibrates, followed by filling of the 2182a buffer. While the nanovoltmeter is capable of measurement speed down to 0.5 ms, optimizing parameters to balance noise to aperture time (the period during which voltage is read), is necessary for resolving the lowest power measurements. Turning off autozeroing, digital, and analog filtering increases speed and noise. Aperture time is set by the integration rate in power line cycles (PLC) from $0.01-60$ PLC. For 60 Hz main power a 0.01 PLC integration rate gives an aperture time of 0.167 ms. A voltage measurement trigger-reading cycle integrates over 3 conversion periods, giving a single measurement time using fastest parameters of ~ 0.5 ms. For this experiment, and in general, noise to speed optimization was found using 0.1 PLC and filtering on, giving a measurement time of ~ 16 ms. The nanovoltmeter buffer size is 1024, limiting the experiment length by the measurement timescale.

To simulate varying levels of localized heat release on the suspended membranes, after initialization of the nanovoltmeter buffer and a short wait time to acquire baseline resistance data, a Keithley 2400 Sourcemeter performs a current-biased 4-wire measurement on a separate thin Pt thermistor (Fig. 6.2). Power is released through ohmic dissipation as given by $P = RI^2$. Currents used range from 10 μA to 200 μA. After enough time passes to establish thermal equilibrium, the heater current is turned off, and an equivalent time is allowed to track the thermal

decay. The cycle is repeated such that 3 heat pulses are collected within the buffer size limit.

Thermal membrane chips are affixed to a gold-plated sample mount designed for the cold stage of a Janis Research custom cryostat for sample-in-vacuum liquid nitrogen cryogenic measurements to take advantage of its existing sample-to-instrumentation wiring. $Al_{0.99}$ - $Si_{0.01}$ alloy bond wire electrically connects the device to a custom PCB, to which all instrumentation is then wired.

6.1.3 Results and Discussion

Fig.6.2 shows the first steps toward understanding the temporal resolution, using existing thermal platforms with resistive thermometry. On the left, measured membrane T is plotted as a function of time while heat is added to the structure by flowing a fixed current in the platform heater. By applying a range of heater power, we can clearly resolve temperature change in air of 10 mK or better. This level of T resolution in a non-optimized structure was encouraging. Repeating this experiment in vacuum (shown at center) allows measurement of the exponential relaxation time, which as shown in Fig. 6.1 yields the heat capacity if K is known. Here we estimate C to be ~ 6 μJ/K, which suggests this non-optimal structure can resolve energy inputs on the order of 50 nJ, or 11.5×10^{11} kCal. If we assume a heat release between 1 and 6000 kCal/mol of virus [149], then this non-optimized device could detect binding from as little as 2×10^{15} mol of virus.

As virions are dispersed in aqueous drops with a wide range of sizes which can vary from virus-to-virus, it is important to understand how the Si-N platforms react to water. The right side of Fig. 6.2 shows the temperature response when a mist of H_2O droplets is introduced to the structure at ambient conditions. A measurable

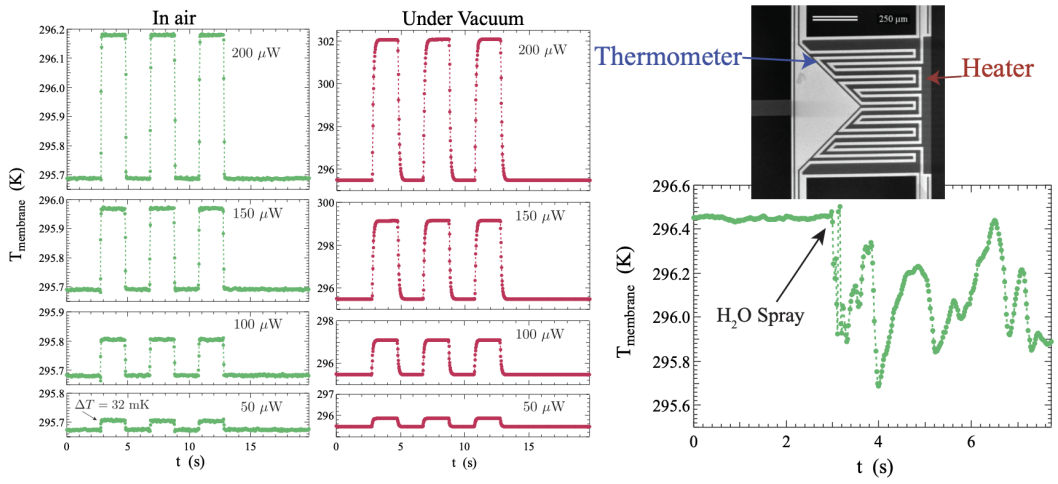

Figure 6.2: Time-dependent temperature measurements comparing response of microcalorimeters in air and in vacuum, for four different applied power levels. At lower right we show the result of a mist of water droplets striking the microcalorimeter in ambient conditions.

change in the T of the membrane is resolved as droplets adsorb and evaporate from the structure. The thermal response when adding a single large drop of water to the structure is measured in Fig. 6.3. In this case we also cycled the heater with power 200 μW to simulate chemical energy release while fully loaded with fluid. The results are consistent with T changes expected from the adsorption and eventual evaporation of the drop, and the smaller T excursions can be seen in all cases. Note also that interactions with water always remove energy from the nanocalorimeter, which helps to identify the energy deposition expected from virus binding or other chemical reactions.

6.1.4 Conclusion

We have demonstrated the temporal and thermal resolution of measurements on suspended thermal isolation platforms in the atmosphere. A significant portion

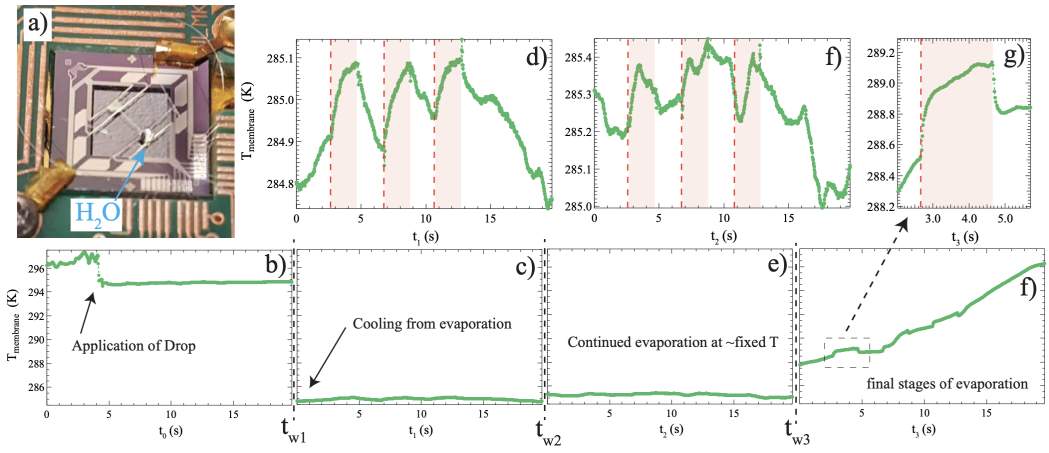

Figure 6.3: The long-term (several minutes) evolution of adsorption and evaporation of a large water droplet. This preliminary data indicates pure water likely always causes T reduction, allowing separation of heating events as modeled by the 200 μW heat pulses (duration shown with red shading). Each measured time window is separated by wait times (t_{w1}, t_{w2} and t_{w3}) of $\sim$ 100 s

of the power applied via ohmic dissipation in the membrane thermistors is dissipated through conduction with air, roughly $\sim$ 5x lower heating than under vacuum conditions. A ΔT below 32 mK can be resolved under these conditions.

Further work includes improving timing resolution, exploring the sensitivity of passive thermometers based on nanofabricated thermocouples, and ultimately designing and fabricating a dedicated calorimeter optimized for open-chamber measurements. Constructing a misting chamber will fine-tune our understanding of atmospheric conditions during viral application. It will also aid in providing a thermal baseline measurement for aerosolized solvents, improving reproducibility in the application process, and controlling exposure when working with viruses. While some of the the benefit of using our platforms is that they are readily available and integrate measurements into a single device, an aerosol detection specific device would be a significant improvement and easily included alongside our normal device fabri-

cation process. The reduction in the heat capacity of the structure by several orders of magnitude is possible by decreasing platform size and reducing the thermometry leads, while improvement in the thermometer sensitivity could also lower the detection limits. Finally, with the collaboration of biophysics and virus experts at the University of Denver whose facilities and expertise include virus growth and detection methods, the application of the reactive target to the thermal platforms and exposure to virus could be facilitated.

6.2 Heat Capacity Measurements on Suspended Si-N Membranes

The exploration of time-dependent measurements for virus detection opened the possibility of adding heat capacity measurement of nanoscale samples to the existing micromachined thermal isolation platforms. Already put to exceptional use for electrical, thermal, thermoelectric and spintronic measurements, the addition of heat capacity capabilities integrated into one single device for concurrent in-situ measurements would advance an already highly unique capability not available anywhere else in the world. Several recent studies have opened questions about what type of excitations carry heat in nanoscale systems ranging from carbon nanotube thermoelectric thin films [131] to carefully engineered ferromagnetic heterostructures [145]. Presented here is a brief introduction to the measurement model, the modification and development of the cryogenic measurement instrumentation, the development of a new measurement software, and the fabrication and results of copper thin films as reference standards. These results show the limitations of current thermal devices for heat capacity measurements, so that they can be addressed by the next generation of thermal platforms.

6.2.1 Introduction

The heat capacity measurement briefly introduced in Section 6.1 is expanded upon here in detail. Thermal relaxation methods determine heat capacity by applying heat ΔQ and measuring the temperature change ΔT, such that $C = \Delta Q/\Delta T$.

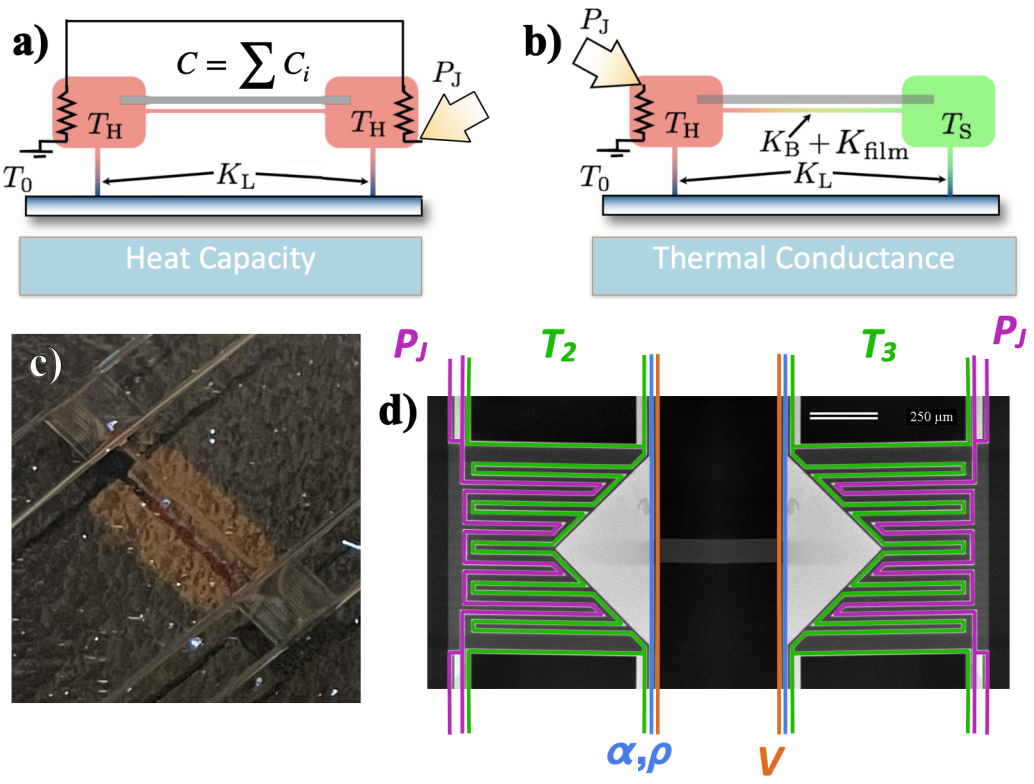

Figure 6.4: **a)** The thermal relaxation model for heat capacity adapted for our suspended Si-N isolation platforms. Heat is dissipated into the system by driving a current (P_J) in series across both island heaters to ensure the least thermal gradient across the bridge. The effective conductance out of the system is the thermal conductance of the legs, K_{Legs}. The heat capacity C is the sum capacities of the islands, bridge, and thin film to be measured. **b)** Thermal model for thermal conductance. **c)** Copper thin film deposited on the bridge. **d)** Wiring diagram for island heaters (P_J), thermometers (T_i), and connecting wires for in-situ electric, thermoelectric, or spintronic measurements (α, ρ, V).

Removing the heat source causes the temperature to decay via a thermal relaxation time constant

$$\tau = \frac{\sum C_i}{K_{\text{eff}}} \tag{6.2.1}$$

where $\sum C_i$ is the sum of all heat capacities in the system, and K_{eff} is the effective thermal conductance out of the system. The AC temperature method [150] isolated the sample relaxation time $\tau_1 = C/K_{\text{eff}}$ from an internal relaxation time $\tau_2 = C/K_{\text{int}}$, where K_{int} is the system's internal thermal conductance. If K_{int} is less than K_{eff} a temperature gradient is generated across the sample as it thermally relaxes, decreasing the accuracy of the measured τ_1. The steady state relaxation method [151] can detect and correct for τ_2 effects. Assuming $\tau_1 \ll \tau_2$, the heat balance equation can be reduced to a one dimensional model and integrated over the dimension of the K_{eff} path. Choosing an interval ΔT small enough such that all C and K remain constant, suddenly switching off heating power to the sample causes a single exponential temperature decay such that

$$\Delta T(t) = (T_1 - T_0)e^{-t/\tau_1} \tag{6.2.2}$$

and any τ_2 shows up as nonexponential in the data. Thus, an accurate measurement of $\tau_1 = C/K_{\text{eff}}$ and K_{eff} constitutes a measurement of the heat capacity of the system. Since the radiative component K_{rad} is proportional to the area and T^3, a small sample under vacuum with proper shielding and at lab temperatures reduces K_{eff} to K_{Legs}, the conductive thermal path from the suspended membrane platforms. As heat capacities are additive, $\sum C_i = C_{\text{sample}} + C_{\text{addenda}}$ and the sample heat capacity

is found by removing the addenda component from the total heat capacity C_{T}. Thus,

$$\begin{aligned} C_{\mathrm{S}} &= C_{\mathrm{T}} - C_{\mathrm{A}} \\ &= K_{\mathrm{Legs}}\tau_{\mathrm{1}} - K_{\mathrm{Legs,A}}\tau_{A} \end{aligned} \tag{6.2.3}$$

For samples where the thermal conductance of the platform legs does not change after thin film depositions, particularly when depositions are isolated to the platform bridge, the heat capacity reduces to

$$C_{\mathrm{S}} = K_{\mathrm{Legs}}(\tau_{\mathrm{1}} - \tau_{A}) \tag{6.2.4}$$

Thus, the requirements for a measurement of specific heat are accurate values of K_{Legs}, τ_{addenda}, τ_{1}, and sample geometry [138,152,153]. Specific heat is then calculated from the sample volume and the density, $c_{\mathbf{m}} = C/\rho \mathrm{V}$, where bulk density and molar mass is assumed, growth thickness is verified with atomic force microscopy, and area is deduced from optical microscopy images.

6.2.2 Experiment

Instrumentation described in Section 6.1.2 is used used, with modifications shown in Fig. 6.5. While the nanovoltmeter is capable of measurement speed down to 0.5 ms, the optimized parameters used for best noise to aperture time are as follows: autozeroing, digital, and analog filtering are off, and the integration rate set is set to 1 power line cycle (PLC), giving an aperture time of 16.7 ms for 60 Hz power. A voltage measurement trigger-reading cycle integrates over 3 conversion periods, giving a single measurement time using these parameters of $\sim$ 50 ms.

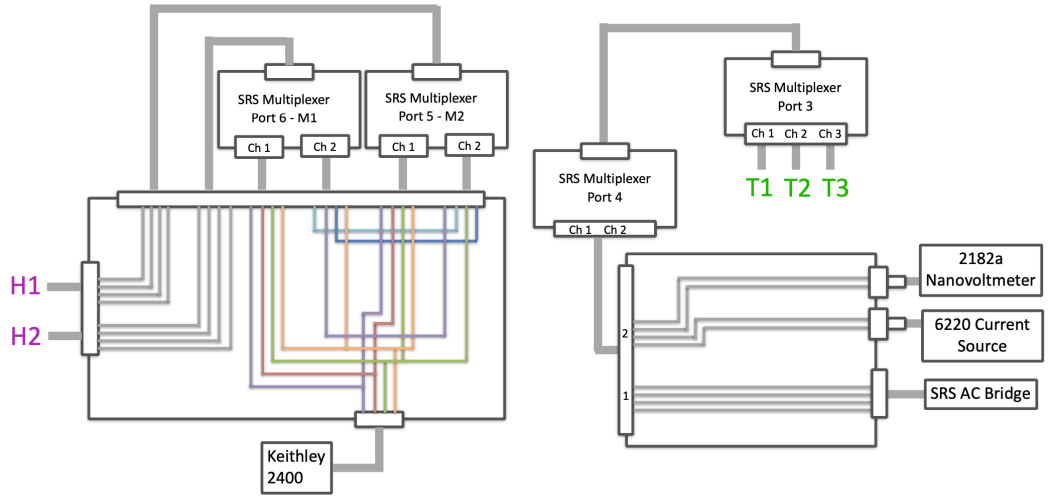

Figure 6.5: Wiring schematic for Pomona shielded split boxes. To preserve function of existing measurement capabilities, a system of wiring reroutes allows automated switching of the connections between the cryostat and instrumentation via SRS Multiplexers, with all appropriate port and channels given. **Left)** Heating elements for the right island R2 and left island R3 are labeled here as H1 and H2 to match labeling of Multiplexer M1 and M2. Heating current from a Keithley 2400 is switched from individual islands to in-series for measuring thermal relaxation to minimize internal thermal gradients (right). **Right)** Thermometers for the cold-bath chip thermistor R1, and islands R2 and R3 (green T1, T2, T3, respectively) are split to switch between the AC resistance bridge for steady-state thermometry and the 2181a/6220 Keithleys for time-dependent measurements.

For relaxation voltage measurements, a 1μA biased DC current is produced by the 6220 precision current source. Heating currents used are from $50-100$ μA, resulting in a power dissipation of $\sim 2.5-10$ μW. Temperature regulation is provided by the standard thermal conductivity measurement main VI and Lakeshore 331. Measurements are made in a liquid nitrogen cryostat.

Fabrication of copper thin films onto thermal isolation devices for specific heat referencing is described in Sec. 7.2. The devices are placed in a gold plated copper sample mount and wire bonded with $Al_{0.99}$-$Si_{0.01}$ alloy bond wire to make electrical

connection with room temperature electronics. The sample mount is capped with a radiation shield to prevent radiative heating and mounted to the cold stage of a sample-in-vacuum cryostat.

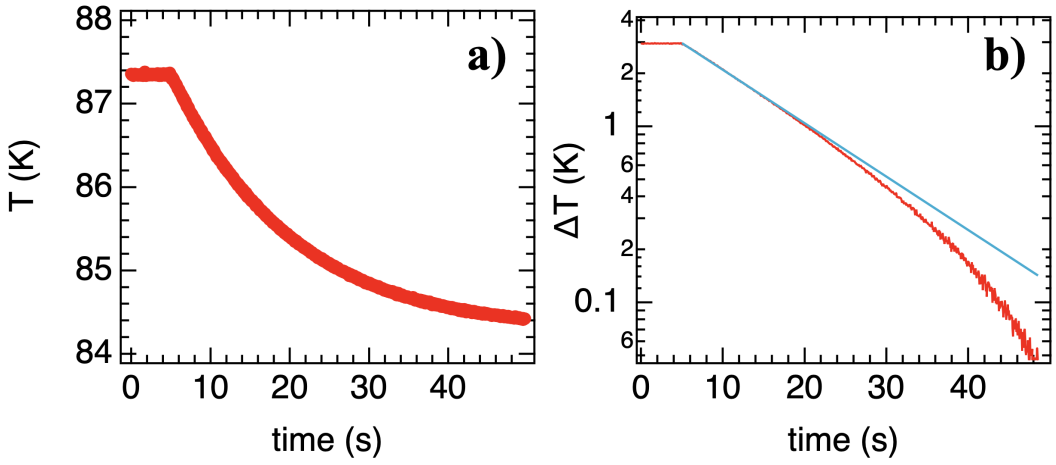

Figure 6.6: **a)** Example of a thermal relaxation after removal of heat source P_J from a bridge-less bulk platform coated in silver paint. At $t = 6$ s heat is removed and thermal energy dissipates out of the system via K_{Legs}. **b)** A log plot of ΔT during relaxation (red). A single decaying exponential is linear on log plots, as shown by the blue line. While τ on this plot seems initially linear, a second relaxation constant is revealed by the deviation from linearity. τ_1 is found by taking linear fits to such log plots when the decay stays linear for $> 3\tau$.

The data is cleaned and organized with custom MATLAB code, and the resulting output uploaded as waves for processing in the analysis program Igor. Each temperature set's relaxation voltages are divided by the bias current, and subsequent resistance values shifted such that it thermally relaxes to zero. The data is reshaped and bulk analysis performed by utilizing a batch curve fitting Igor package. The natural log of the zero-offset resistances are fit with a linear function beginning directly after time constant power was removed. The slope of this fit is the negative inverse thermal relaxation constant, $m = -1/\tau$ (Fig. 6.6). The range of data fit is optimally over multiple τ, however this is not always the case and is discussed later.

6.2.3 Results and Discussion

The heat capacity of copper thin films of down to 30 nm should align very closely to bulk values [153]. However, as seen in Fig. 6.7, our best specific heat measurements of a 75 nm and 300 nm Cu thin film deviates significantly from the expected bulk molar specific heat [154]. This is an unexpected measurement artifact and likely not attributable to real physical mechanisms.

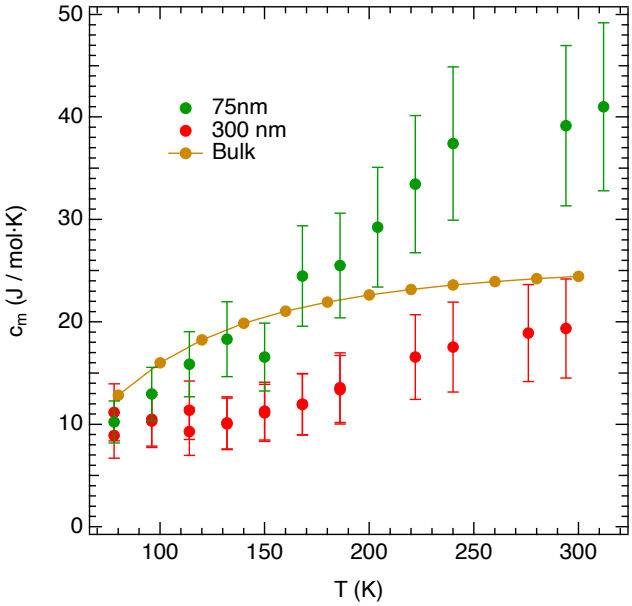

Figure 6.7: Specific heat c_{mol} vs T for 75 nm (green) and 300 nm (red) copper thin films. Cu thin films are expected to agree closely with bulk specific heat values (gold). Because $K_{\text{internal}} < K_{\text{Legs}}$ a thermal gradient forms across the bridge and sample causing a large internal relaxation. At low temperatures the difference in K_{internal} and K_{Legs} is small (Fig. 6.8b), and so c_{mol} has greater agreement with bulk. As $K_{\text{internal}} \ll K_{\text{Legs}}$ at higher temperatures the impact becomes more apparent. The larger K from the thicker 300 nm results in closer values, however the subtraction of the addenda over-corrects and remains the dominating source of error. Error bars are calculated from exponential fits, volume estimates, and K measurement error, and does not account for internal relaxation or represent validity of c_{mol}.

As discussed in the caption of Fig. 6.7, a lower internal conductance than the effective conductance out of the system, $K_{\text{internal}} \ll K_{\text{Legs}}$, is possible detriment to using the relaxation method on these versions of thermal isolation platforms. Multiple measurement methods and styles were attempted to reduce internal thermal gradients, however as seen in Fig. 6.8 an appreciable temperature difference was unavoidable. Another source of error comes from a large difference in individual island τ values for identical relaxation measurements. This is possibly from the development of an internal gradient, inhomogeneity of electrical leads between islands, and masking shifts resulting in different volumes of copper deposition on each island.

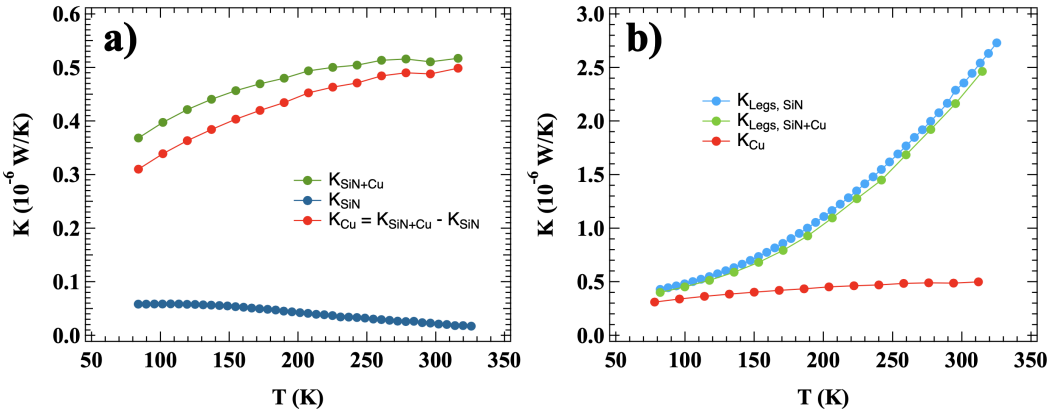

Figure 6.8: **a)** Thermal conductance K vs T for 75 nm copper thin film on SiN bridge (green), the SiN bridge addenda (blue), and an addenda-subtracted K_{Cu} (red). While a small thermal conductance across the bridge addenda is optimal for thermal conductivity measurements, during relaxation measurements if $K_{\text{internal}} < K_{\text{Legs}}$ a thermal gradient will develop when the islands cool quicker than the bridge. As seen in **b)**, the high thermal conductance of the Cu (red) is still less than K_{Legs} at all temperatures.

Whereas the dimensions of transport along the bridge is well known for thermal and electrical conductivity calculations, the total deposited volume of the sample

is required to precisely infer specific heat. By design the deposition mask allows sample growth on the island triangle leads for electrical contact which contributes to the total heat capacity. Significant errors can be introduced in this step from assuming sample dimensions, as the sample edge is sloped and not well defined. Deviations in the alignment of the deposition mask can lead to unequal sample volumes between the islands. This difference in individual island heat capacities causes an unequal increase in temperature from equal amounts of heating power, inducing a thermal gradient across the bridge.

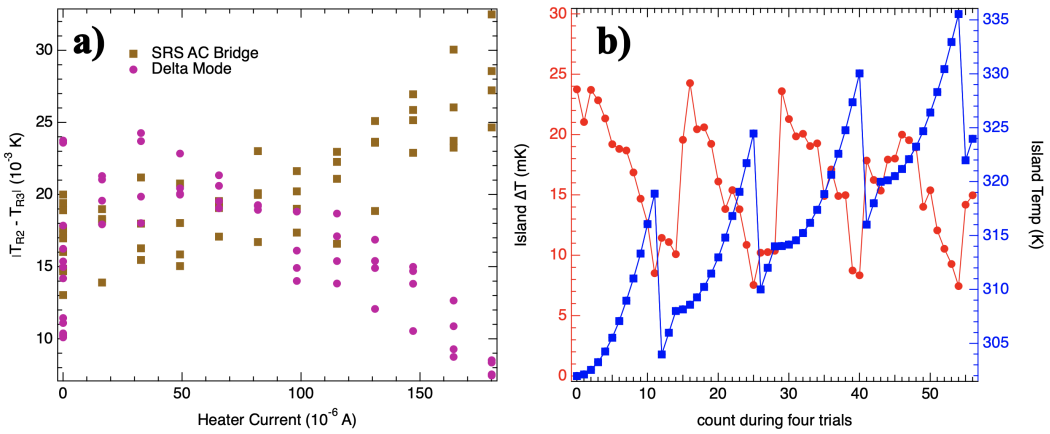

Figure 6.9: **a)** Current driven in series through both island heaters causes a small temperature difference between the islands of roughly 10 - 30 mK, likely due to defects or small deviations in fabrication uniformity between the island Pt thermistor heating elements. Two resistance measurement styles are compared, the SRS AC Resistance Bridge (gold) and Keithley 2181a/6220 delta mode (purple). **b)** The same purple delta mode data plotted sequentially during the measurement

6.2.4 Conclusion

These results reveal that while we might be able to use current generation platforms for open-chamber viral detection, they are insufficient for high preci-

sion cryogenic microcalorimetry. Isothermal conditions between the thermometer and sample could be achieved by adding a conduction layer before sample deposition. This would require two devices for each sample growth: one for conductivity and thermopower measurements, and another for heat capacity, adding significant measurement time. Another option would be by adding an electrically passivating Al_2O_3 layer to a bridge-less 'Bulk' chip before depositing the material to be measured on the entire island. While this would be an easy way to use existing devices, but the design and fabrication of standalone isolation platforms specialized for nanocalorimetry is the ultimate goal.

Chapter 7

Violation of Wiedemann-Franz Law in Copper Thin Films

7.1 Introduction

Electrons transport both charge and energy as heat. Whereas electrons bound to atoms by their nuclear potential contribute to heat transfer through their allowable vibrational modes (conduction). Free electrons posses an internal kinetic energy and momentum that is transported through a Fermi fluid. If this kinetic energy is higher than its surrounding average, it is can be thought of as convection of heat. Thermal resistance is due to scattering mechanisms that limit the electron and phonon contributions to thermal conductivity κ. In metals κ is normally dominated by the transport of heat by electrons. In the free electron approximation for pure metals, all thermal conductivity is mediated by electrons

$$\kappa_e = \frac{\pi^2}{3}\frac{nk_B^2\tau T}{m} \tag{7.1.1}$$

where τ is the relaxation time defined by the mean free path and carrier velocity $\tau = l/v$. The Drude model in a constant electric field gives the Lorentz-Sommerfeld

relation for electrical conductivity

$$\sigma = \frac{ne^2 l}{mv} \tag{7.1.2}$$

The Wiedemann-Franz Law (WF) provides information on what part of thermal transport is electron-mediated by providing a ratio of thermal to electric conductivities. The proportionality constant relating this ratio to its temperature is called the Lorenz number and is given by

$$\frac{\kappa}{\sigma} = LT \tag{7.1.3}$$

The Sommerfeld value L_0 provides the theoretical value for the Lorenz number if all thermal conductivity is provided by free electrons. Using Equ. 7.1.1 and 7.1.2, pure metals in the free electron approximation give the value

$$\frac{K_e}{\sigma T} = \frac{\pi^2 k_B^2}{3e^2} = L_0 = 2.45 \times 10^{-8} \mathrm{W\Omega/K^2} \tag{7.1.4}$$

"Violations" of the WF law are normal for real materials as disorder and impurities are common in even the best ordered crystal lattices. Measured Lorenz numbers greater than L_0 indicates non-electron contributions to κ such as phonon or magnon heat transportation. Small violations of WF leading to a slight reduction in L below L_0 are common at intermediate temperatures due to disorder and inelastic electron-phonon scattering, particularly in metals at or below its Debeye temperature [155].

This is expected in most simple metals, including in the thin film limit, as verified for a number of materials on our suspended thermal isolation platforms [112]. More recently, an unusually large violation showing significant reductions in L were reported for Au thin films [146]. In that work, thermal-evaporated Au was deposited

on amorphous silicon nitride thermal isolation platforms in much the same way as the copper thin films used as reference standards for heat capacity experiments outlined in Section 6.2. In this section we report the temperature dependent thermal and electrical conductivities of two copper thin films, and report a similar large violation of the Wiedemann-Franz law.

7.2 Experiment

Copper pellets were thermally evaporated by running 80 A of current across a tungsten boat. A 300 nm Cu sample was grown at a rate of 1.1 Å/s at a pressure of $7.1e^{-7}$ Torr, and a 75 nm Cu sample was grown at a rate of 1.0 Å/s at $7.1e^{-7}$ Torr. Both were grown on standard suspended membrane chips from wafer CINT15, and on separate *a*-SiN coated silicon 1cm $\times$ 1cm chips for later thickness and optical studies. Thermal conductance measurements were performed using the method outlined in Appendix A. Electrical resistance measurements were done *in-situ* by stepping through a series of Keithley 2400 sourcemeter current-biased voltage measurements on the island's 4-wire style Pt leads (ρ,V in Fig. 6.4d). A linear fit of the resulting I-V curves produces a film resistance free from wiring thermovoltage or other contributions.

Thickness values t are the reported thermal evaporation thicknesses provided by monitoring the growth chamber's thickness sensor crystal's oscillating frequency. While a secondary measurement of thicknesses by AFM is necessary future work, the Lorenz number can be calculated independent of film thickens from the thermal conductance K and electrical resistance R. Thermal conductivity is found by taking $\kappa = Kl/wt$ and electrical conductivity by $\sigma = 1/\rho = l/Rwt$, where $l = 2050$ μm is the bridge length, $w = 88$ μm is the bridge width. The WF law can then be reduced

by taking $\kappa/\sigma = KR$, leading to the form

$$L = \frac{K_{\text{film}} R_{\text{film}}}{T} \tag{7.2.1}$$

7.3 Results and Discussion

Electrical resistivity values are reported in Fig. 7.1. As expected, over the range measured the temperature dependence is uniformly increasing as a function of thickness, indicating the standard thin film enhancement of residual resistivity in the limit where charge carrier mean free paths become dimensionally constrained. The 300 nm (red) is slightly higher than bulk resistivity values (gold) [154], and 75

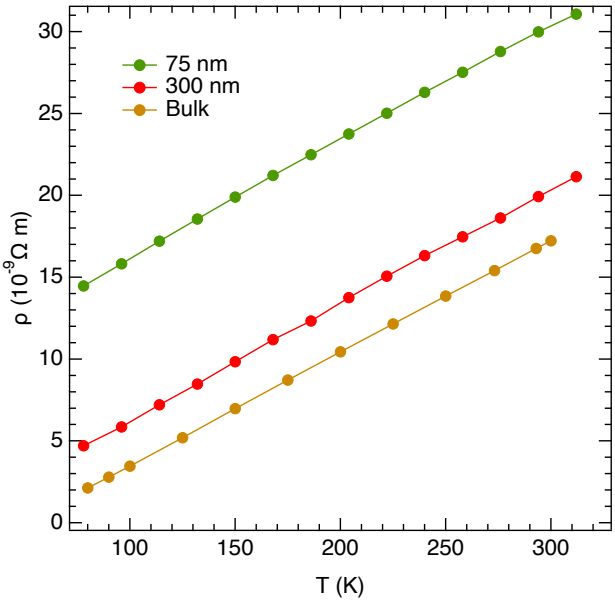

Figure 7.1: Electrical resistivity ρ vs T for 75 nm (green) and 300 nm (red) copper thin films, as compared to bulk (gold) values [154]. As expected, resistivity increases with decreasing thickness, and align with values from previous studies [156].

nm (green) is further increased. These values align well with previous resistivity measurements of Cu thin films of comparable thickness [156].

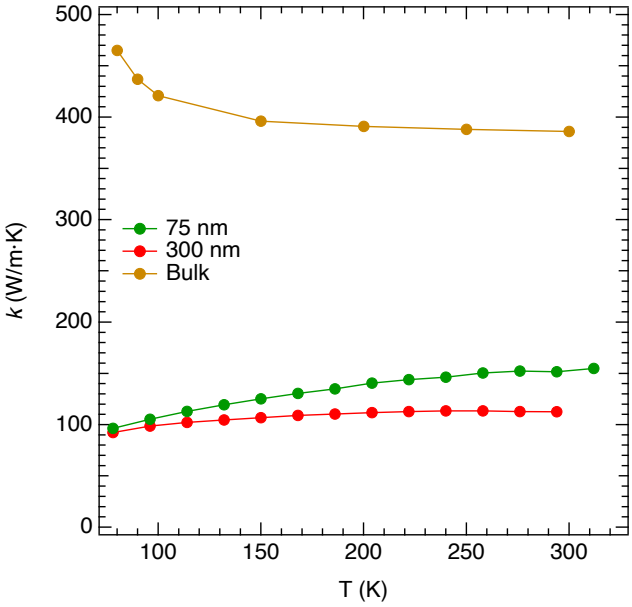

Figure 7.2: Thermal conductivity k vs T for 75 nm and 300 nm copper thin films

While the electrical profile of the copper thin films trend as expected, the thermal conductivity is unexpectedly massively reduced from bulk values (Fig. 7.2). The thermal conductivity for both 300 nm (red) and 75 nm (green) are greatly suppressed from bulk (gold) at all temperatures measured and their temperature dependence is reversed, particularly at low T. In bulk metals dominated by electron transportation of heat, reduction of allowable phonon modes at low temperatures reduces phonon-electron scattering, leading to a rise in κ. However, the thin films measured show a reversed trend, gently decreasing at lower temperatures to a seemingly common value of κ. The thickness-dependence of κ between the two samples studied deviates greatly from previous reports, from having similar low T values, to higher suppression in the thicker film. While it has been seen that the dependence

of defect contributions to thermal conductivity increases in thin film limits, leading to a thin film reversal in temperature dependence at low T [156], the magnitude of reduction in κ observed here is significantly greater and previously unreported.

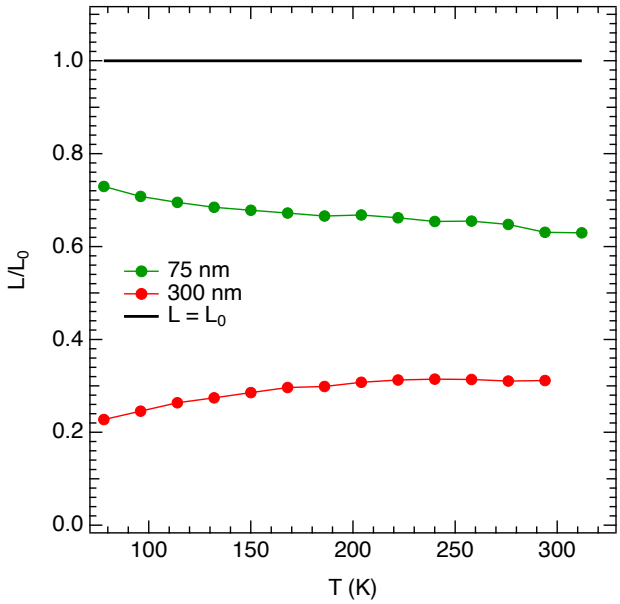

Figure 7.3: Lorentz ratio L/L_0 vs. T for 75 nm and 300 nm copper thin films

The large reduction in thermal conductivity contributes to a significant violation of the WF law as seen in Fig. 7.3. The Lorentz ratio for 75 nm is decreased to about $0.7-0.6$, and the 300 nm ratio sees massive reduction down to $L/L_0 \sim 0.2-0.3$ While electrical residual resistivity increases for thinner thicknesses, the κ reported has a significantly reduced size dependence. A similar reductions in L reported in Au thin films attributes the reduction in L to inelastic electron-phonon scattering [146]. In that study, large vertical pillars introduced grain boundaries that could potentially cause inelastic scattering that preserves electron transport in-plane across the film while reducing the magnitude of the total momentum.

7.4 Conclusions

We reported a large violation in the Weiddeman-Franz law in copper thin films. This violation is driven primarily by a reduction in thermal conductivity that preserves the electron density of states. Future work on these films should include atomic force microscopy to verify film thickness, grain size and structure, and film roughness. X-ray diffraction would reveal long-range crystalline ordering and the possible inclusion of impurities or defect sites.

Bibliography

[1] http://www.qdusa.com.

[2] D. P. Osterman and S. J. Williamson. Effect of sample and magnetometer dimensions on the flux detected by a SQUID magnetometer. *Review of Scientific Instruments*, 54(10):1380–1382, oct 1983.

[3] D.-X. Chen, J.A. Brug, and R.B. Goldfarb. Demagnetizing factors for cylinders. *IEEE Transactions on Magnetics*, 27(4):3601–3619, Jul 1991.

[4] Quantum Design Application Note 1070-207, Using PPMS Superconducting Magnets at Low Fields. Jun 2009.

[5] M Sawicki, W Stefanowicz, and A Ney. Sensitive SQUID magnetometry for studying nanomagnetism. *Semiconductor Science and Technology*, 26(6):064006, Apr 2011.

[6] M. Buchner, K. Höfler, B. Henne, V. Ney, and A. Ney. Tutorial: Basic principles, limits of detection, and pitfalls of highly sensitive SQUID magne-

tometry for nanomagnetism and spintronics. *Journal of Applied Physics*, 124(16):161101, oct 2018.

[7] A. Ney, T. Kammermeier, V. Ney, K. Ollefs, and S. Ye. Limitations of measuring small magnetic signals of samples deposited on a diamagnetic substrate. *Journal of Magnetism and Magnetic Materials*, 320(23):3341–3346, dec 2008.

[8] C.E. Gough. Flux quantisation and SQUID magnetometry using ceramic superconductors. *Physica C: Superconductivity*, 153-155:1567–1573, jun 1988.

[9] A A Serga, A V Chumak, and B Hillebrands. YIG magnonics. *Journal of Physics D: Applied Physics*, 43(26):264002, Jun 2010.

[10] A. V. Chumak, V. I. Vasyuchka, A. A. Serga, and B. Hillebrands. Magnon spintronics. *Nat Phys*, 11(6):453–461, Jun 2015.

[11] B. Heinrich, C. Burrowes, E. Montoya, B. Kardasz, E. Girt, Young-Yeal Song, Yiyan Sun, and Mingzhong Wu. Spin pumping at the magnetic insulator (yig)/normal metal (au) interfaces. *Phys. Rev. Lett.*, 107:066604, Aug 2011.

[12] Mathias Weiler, Matthias Althammer, Franz D. Czeschka, Hans Huebl, Martin S. Wagner, Matthias Opel, Inga-Mareen Imort, Günter Reiss, Andy

Thomas, Rudolf Gross, and Sebastian T. B. Goennenwein. Local charge and spin currents in magnetothermal landscapes. *Phys. Rev. Lett.*, 108:106602, Mar 2012.

[13] Mathias Weiler, Matthias Althammer, Michael Schreier, Johannes Lotze, Matthias Pernpeintner, Sibylle Meyer, Hans Huebl, Rudolf Gross, Akashdeep Kamra, Jiang Xiao, Yan-Ting Chen, HuJun Jiao, Gerrit Bauer, and Sebastian Goennenwein. Experimental test of the spin mixing interface conductivity concept. *Phys. Rev. Lett.*, 111:176601, Oct 2013.

[14] H. L. Wang, C. H. Du, Y. Pu, R. Adur, P. C. Hammel, and F. Y. Yang. Large spin pumping from epitaxial $Y_3Fe_5O_{12}$ thin films to Pt and W layers. *Phys. Rev. B*, 88:100406, Sep 2013.

[15] M. Haertinger, C. H. Back, J. Lotze, M. Weiler, S. Geprägs, H. Huebl, S. T. B. Goennenwein, and G. Woltersdorf. Spin pumping in YIG/Pt bilayers as a function of layer thickness. *Phys. Rev. B*, 92:054437, Aug 2015.

[16] Lin Liu, Yuehui Li, Yahui Liu, Tao Feng, Jun Xu, X. R. Wang, D. Wu, Peng Gao, and J. Li. Interfacial modulation of spin pumping in YIG/Pt. *Phys. Rev. B*, 102:014411, Jul 2020.

[17] Ken-ichi Uchida, Hiroto Adachi, Takeru Ota, Hiroyasu Nakayama, Sadamichi Maekawa, and Eiji Saitoh. Observation of longitudinal spin-Seebeck effect in magnetic insulators. *Applied Physics Letters*, 97(17), 2010.

[18] K Uchida, M Ishida, T Kikkawa, A Kirihara, T Murakami, and E Saitoh. Longitudinal spin Seebeck effect: from fundamentals to applications. *Journal of Physics: Condensed Matter*, 26(34):343202, 2014.

[19] D. Qu, S. Y. Huang, Jun Hu, Ruqian Wu, and C. L. Chien. Intrinsic spin Seebeck effect in Au/YIG. *Phys. Rev. Lett.*, 110:067206, Feb 2013.

[20] D. Qu, S. Y. Huang, B. F. Miao, S. X. Huang, and C. L. Chien. Self-consistent determination of spin Hall angles in selected 5*d* metals by thermal spin injection. *Phys. Rev. B*, 89:140407, Apr 2014.

[21] S. M. Bleser, R. M. Greening, M. J. Roos, L. A. Hernandez, X. Fan, and B. L. Zink. Negative spin hall angle and large spin-charge conversion in thermally evaporated chromium thin films. *Journal of Applied Physics*, 131(11):113904, Mar 2022.

[22] L. J. Cornelissen, J. Liu, R. A. Duine, J. Ben Youssef, and B. J. van Wees. Long-distance transport of magnon spin information in a magnetic insulator at room temperature. *Nat Phys*, 11(12):1022–1026, Sep 2015.

[23] Sebastian T. B. Goennenwein, Richard Schlitz, Matthias Pernpeintner, Kathrin Ganzhorn, Matthias Althammer, Rudolf Gross, and Hans Huebl. Non-local magnetoresistance in YIG/Pt nanostructures. *Appl. Phys. Lett.*, 107(17):172405, Oct 2015.

[24] L. J. Cornelissen and B. J. van Wees. Magnetic field dependence of the magnon spin diffusion length in the magnetic insulator yttrium iron garnet. *Phys. Rev. B*, 93:020403, Jan 2016.

[25] Juan Shan, Ludo J. Cornelissen, Nynke Vlietstra, Jamal Ben Youssef, Timo Kuschel, Rembert A. Duine, and Bart J. van Wees. Influence of yttrium iron garnet thickness and heater opacity on the nonlocal transport of electrically and thermally excited magnons. *Phys. Rev. B*, 94:174437, Nov 2016.

[26] L. J. Cornelissen, J. Liu, B. J. van Wees, and R. A. Duine. Spin-current-controlled modulation of the magnon spin conductance in a three-terminal magnon transistor. *Phys. Rev. Lett.*, 120:097702, Mar 2018.

[27] H. Wu, L. Huang, C. Fang, B. S. Yang, C. H. Wan, G. Q. Yu, J. F. Feng, H. X. Wei, and X. F. Han. Magnon valve effect between two magnetic insulators. *Phys. Rev. Lett.*, 120:097205, Mar 2018.

[28] T. Wimmer, M. Althammer, L. Liensberger, N. Vlietstra, S. Geprägs, M. Weiler, R. Gross, and H. Huebl. Spin transport in a magnetic insula-

tor with zero effective damping. *Physical Review Letters*, 123(25):257201, Dec 2019.

[29] Georg Schmidt, Christoph Hauser, Philip Trempler, Maximilian Paleschke, and Evangelos Th. Papaioannou. Ultra thin films of yttrium iron garnet with very low damping: A review. *physica status solidi (b)*, 257(7):1900644, Apr 2020.

[30] Yu.K. Fetisov, P. Kabos, and C.E. Patton. Active magnetostatic wave delay line. *IEEE Transactions on Magnetics*, 34(1):259–271, 1998.

[31] A. D. Karenowska, A. V. Chumak, A. A. Serga, J. F. Gregg, and B. Hillebrands. Magnonic crystal based forced dominant wavenumber selection in a spin-wave active ring. *Applied Physics Letters*, 96(8):082505, 2010.

[32] Elena Bankowski, Thomas Meitzler, Roman S. Khymyn, Vasil S. Tiberkevich, Andrei N. Slavin, and Hong X. Tang. Magnonic crystal as a delay line for low-noise auto-oscillators. *Applied Physics Letters*, 107(12):122409, 2015.

[33] A. D. Karenowska, J. F. Gregg, V. S. Tiberkevich, A. N. Slavin, A. V. Chumak, A. A. Serga, and B. Hillebrands. Oscillatory energy exchange between waves coupled by a dynamic artificial crystal. *Phys. Rev. Lett.*, 108:015505, Jan 2012.

[34] Lutong Sheng, Jilei Chen, Hanchen Wang, and Haiming Yu. Magnonics based on thin-film iron garnets. *Journal of the Physical Society of Japan*, 90(8):081005, 2021.

[35] P. Schiffer, A. P. Ramirez, D. A. Huse, P. L. Gammel, U. Yaron, D. J. Bishop, and A. J. Valentino. Frustration induced spin freezing in a site-ordered magnet: Gadolinium gallium garnet. *Phys. Rev. Lett.*, 74:2379–2382, Mar 1995.

[36] L M C Pereira, J P Araújo, M J Van Bael, K Temst, and A Vantomme. Practical limits for detection of ferromagnetism using highly sensitive magnetometry techniques. *Journal of Physics D: Applied Physics*, 44(21):215001, May 2011.

[37] http://www.crystal-gmbh.com.

[38] https://www.mtixtl.com.

[39] Eva Liskova Jakubisova, Stefan Visnovsky, Houchen Chang, and Mingzhong Wu. Interface effects in nanometer-thick yttrium iron garnet films studied by magneto-optical spectroscopy. *Applied Physics Letters*, 108(8):082403, Feb 2016.

[40] James C. Gallagher, Angela S. Yang, Jack T. Brangham, Bryan D. Esser, Shane P. White, Michael R. Page, Keng-Yuan Meng, Sisheng Yu, Rohan Adur, William Ruane, Sarah R. Dunsiger, David W. McComb, Fengyuan

Yang, and P. Chris Hammel. Exceptionally high magnetization of stoichiometric $Y_3Fe_5O_{12}$ epitaxial films grown on $Gd_3Ga_5O_{12}$. *Applied Physics Letters*, 109(7):072401, Aug 2016.

[41] A. Mitra, O. Cespedes, Q. Ramasse, M. Ali, S. Marmion, M. Ward, R. M. D. Brydson, C. J. Kinane, J. F. K. Cooper, S. Langridge, and B. J. Hickey. Interfacial origin of the magnetisation suppression of thin film yttrium iron garnet. *Scientific Reports*, 7(1):11774, Sep 2017.

[42] J. F. K. Cooper, C. J. Kinane, S. Langridge, M. Ali, B. J. Hickey, T. Niizeki, K. Uchida, E. Saitoh, H. Ambaye, and A. Glavic. Unexpected structural and magnetic depth dependence of YIG thin films. *Phys. Rev. B*, 96:104404, Sep 2017.

[43] Juan M. Gomez-Perez, Saül Vélez, Lauren McKenzie-Sell, Mario Amado, Javier Herrero-Martín, Josu López-López, S. Blanco-Canosa, Luis E. Hueso, Andrey Chuvilin, Jason W. A. Robinson, and Fèlix Casanova. Synthetic antiferromagnetic coupling between ultrathin insulating garnets. *Phys. Rev. Applied*, 10:044046, Oct 2018.

[44] S. M. Suturin, A. M. Korovin, V. E. Bursian, L. V. Lutsev, V. Bourobina, N. L. Yakovlev, M. Montecchi, L. Pasquali, V. Ukleev, A. Vorobiev, A. Devishvili, and N. S. Sokolov. Role of gallium diffusion in the formation of

a magnetically dead layer at the $Y_3Fe_5O_{12}/Gd_3Ga_5O_{12}$ epitaxial interface. *Phys. Rev. Materials*, 2:104404, Oct 2018.

[45] Josep Fontcuberta, Hari Babu Vasili, Jaume Gàzquez, and Fèlix Casanova. On the role of interfaces on spin transport in magnetic insulator/normal metal heterostructures. *Advanced Materials Interfaces*, 6(15):1900475, May 2019.

[46] Ledong Wang, Zhijian Lu, Xiaonan Zhao, Weizhen Zhang, Yanxue Chen, Yufeng Tian, Shishen Yan, Lihui Bai, and Michael Harder. Magnetization coupling in a YIG/GGG structure. *Physical Review B*, 102(14):144428, Oct 2020.

[47] Ravinder Kumar, S. N. Sarangi, D. Samal, and Z. Hossain. Positive exchange bias and inverted hysteresis loop in $Y_3Fe_5O_{12}/Gd_3Ga_5O_{12}$. *Phys. Rev. B*, 103:064421, Feb 2021.

[48] Frances Hellman, Axel Hoffmann, Yaroslav Tserkovnyak, Geoffrey S. D. Beach, Eric E. Fullerton, Chris Leighton, Allan H. MacDonald, Daniel C. Ralph, Dario A. Arena, Hermann A. Dürr, Peter Fischer, Julie Grollier, Joseph P. Heremans, Tomas Jungwirth, Alexey V. Kimel, Bert Koopmans, Ilya N. Krivorotov, Steven J. May, Amanda K. Petford-Long, James M. Rondinelli, Nitin Samarth, Ivan K. Schuller, Andrei N. Slavin, Mark D. Stiles, Oleg Tchernyshyov, André Thiaville, and Barry L. Zink. Interface-induced phenomena in magnetism. *Rev. Mod. Phys.*, 89:025006, Jun 2017.

[49] R. C. LeCraw, E. M. Gyorgy, and R. Wolfe. Suppression of hard bubbles in LPE garnet films by inert atmosphere annealing. *Applied Physics Letters*, 24(11):573–574, Jun 1974.

[50] Takumi Yamagishi, Junji Awaka, Yuusuke Kawashima, Masahiko Uemura, Shuji Ebisu, Susumu Chikazawa, and Shoichi Nagata. Ferrimagnetic order in the mixed garnet $(Y_{1-x}Gd_x)_3Fe_5O_{12}$. *Philosophical Magazine*, 85(17):1819–1833, Jun 2005.

[51] M. Haidar, M. Ranjbar, M. Balinsky, R. K. Dumas, S. Khartsev, and J. Åkerman. Thickness- and temperature-dependent magnetodynamic properties of yttrium iron garnet thin films. *Journal of Applied Physics*, 117(17):17D119, 2015.

[52] Houchen Chang, Peng Li, Wei Zhang, Tao Liu, Axel Hoffmann, Longjiang Deng, and Mingzhong Wu. Nanometer-thick yttrium iron garnet films with extremely low damping. *IEEE Magnetics Letters*, 5:1–4, 2014.

[53] Christoph Hauser, Tim Richter, Nico Homonnay, Christian Eisenschmidt, Mohammad Qaid, Hakan Deniz, Dietrich Hesse, Maciej Sawicki, Stefan G. Ebbinghaus, and Georg Schmidt. Yttrium iron garnet thin films with very low damping obtained by recrystallization of amorphous material. *Scientific Reports*, 6(1), Feb 2016.

[54] Jinjun Ding, Tao Liu, Houchen Chang, and Mingzhong Wu. Sputtering growth of low-damping yttrium-iron-garnet thin films. *IEEE Magnetics Letters*, 11:5502305, 2020.

[55] C.F. Majkrzak, K.V. O'Donovan, and N.F. Berk. Polarized neutron reflectometry. In *Neutron Scattering from Magnetic Materials*, pages 397–471. Elsevier, 2006.

[56] Brian Maranville, William Ratcliff II, and Paul Kienzle. Reductus: a stateless python data reduction service with a browser front end. *Journal of Applied Crystallography*, 51(5):1500–1506, Sep 2018.

[57] B.J. Kirby, P.A. Kienzle, B.B. Maranville, N.F. Berk, J. Krycka, F. Heinrich, and C.F. Majkrzak. Phase-sensitive specular neutron reflectometry for imaging the nanometer scale composition depth profile of thin-film materials. *Current Opinion in Colloid & Interface Science*, 17(1):44–53, Feb 2012.

[58] He Bai, X. Z. Zhan, Gang Li, Jian Su, Z. Z. Zhu, Ying Zhang, T. Zhu, and J. W. Cai. Characterization of YIG thin films and vacuum annealing effect by polarized neutron reflectometry and magnetotransport measurements. *Applied Physics Letters*, 115(18):182401, Oct 2019.

[59] I. S. Anderson, P. J. Brown, J. M. Carpenter, G. Lander, R. Pynn, J. M. Rowe, O. Schärpf, V. F. Sears, and B. T. M. Willis. Neutron techniques.

In *International Tables for Crystallography*, pages 430–487. International Union of Crystallography, Oct 2006.

[60] J.E. Lynn and P.A. Seeger. Resonance effects in neutron scattering lengths of rare-earth nuclides. *Atomic Data and Nuclear Data Tables*, 44(2):191–207, Mar 1990.

[61] Brian B. Maranville, Aaron Green, and Paul A. Kienzle. Distributed error-function roughness in refl1d reflectometry fitting program, 2018.

[62] J. A. Vrugt, C.J.F. ter Braak, C.G.H. Diks, B. A. Robinson, J. M. Hyman, and D. Higdon. Accelerating Markov chain monte carlo simulation by differential evolution with self-adaptive randomized subspace sampling. *International Journal of Nonlinear Sciences and Numerical Simulation*, 10(3), Jan 2009.

[63] B. J. Kirby, L. Fallarino, P. Riego, B. B. Maranville, Casey W. Miller, and A. Berger. Nanoscale magnetic localization in exchange strength modulated ferromagnets. *Physical Review B*, 98(6):064404, Aug 2018.

[64] M. J. Roos and B. L. Zink. Apparent non-linear negative magnetization and exchange bias in paramagnetic substrates driven by trapped flux. in preparation.

[65] J. de la Venta, M. Erekhinsky, Siming Wang, K. G. West, R. Morales, and Ivan K. Schuller. Exchange bias induced by the Fe_3O_4 Verwey transition. *Phys. Rev. B*, 85:134447, Apr 2012.

[66] S. J. Yuan, L. Li, T. F. Qi, L. E. DeLong, and G. Cao. Giant vertical magnetization shift induced by spin canting in a Co/$Ca_2Ru_{0.98}Fe_{0.02}FeO_4$ heterostructure. *Phys. Rev. B*, 88:024413, Jul 2013.

[67] Rakesh Rana, Parul Pandey, and D. S. Rana. Controlling the coexisting vertical magnetization shift and exchange bias in $La_{0.3}Sr_{0.7}FeO_3$/$SrRuO_3$ bilayers. *Applied Physics Letters*, 104(9):092413, Mar 2014.

[68] Michael J. Pechan, Douglas Bennett, Nienchtze Teng, C. Leighton, J. Nogués, and Ivan K. Schuller. Induced anisotropy and positive exchange bias: A temperature, angular, and cooling field study by ferromagnetic resonance. *Phys. Rev. B*, 65:064410, Jan 2002.

[69] C. Leighton, H. Suhl, Michael J. Pechan, R. Compton, J. Nogués, and Ivan K. Schuller. Coercivity enhancement above the Néel temperature of an antiferromagnet/ferromagnet bilayer. *Journal of Applied Physics*, 92(3):1483–1488, 2002.

[70] M. Grimsditch, A. Hoffmann, P. Vavassori, Hongtao Shi, and D. Lederman. Exchange-induced anisotropies at ferromagnetic-antiferromagnetic in-

terfaces above and below the Néel temperature. *Phys. Rev. Lett.*, 90:257201, Jun 2003.

[71] E. Shipton, K. Chan, T. Hauet, O. Hellwig, and E. E. Fullerton. Suppression of the perpendicular anisotropy at the CoO Néel temperature in exchange-biased CoO/[Co/Pt] multilayers. *Applied Physics Letters*, 95(13):–, 2009.

[72] B. L. Zink, M. Manno, L. O'Brien, J. Lotze, M. Weiler, D. Bassett, S. J. Mason, S. T. B. Goennenwein, M. Johnson, and C. Leighton. Efficient spin transport through native oxides of nickel and permalloy with platinum and gold overlayers. *Phys. Rev. B*, 93:184401, May 2016.

[73] Eric E. Fullerton, K. T. Riggs, C. H. Sowers, S. D. Bader, and A. Berger. Suppression of biquadratic coupling in Fe/Cr(001) superlattices below the Néel transition of Cr. *Phys. Rev. Lett.*, 75:330–333, Jul 1995.

[74] F. Y. Yang and C. L. Chien. Exchange coupling between Cr and ferromagnetic thin films. *Journal of Applied Physics*, 93(10):6829–6831, May 2003.

[75] F. Y. Yang and C. L. Chien. Oscillatory exchange bias due to an antiferromagnet with incommensurate spin-density waves. *Physical Review Letters*, 90(14), Apr 2003.

[76] J. S. Parker, L. Wang, K. A. Steiner, P. A. Crowell, and C Leighton. Exchange bias as a probe of the incommensurate spin-density wave in epitaxial Fe/Cr(001). *Phys. Rev. Lett.*, 97:227206, Dec 2006.

[77] M. J. Roos M, S. M. Bleser AND. L. Hernandez, T. Liu, M. Wu, G. Diederich, M. E. Seimens, and B. L. Zink. Electrical, optical, and magnetic properties of amorphous yttrium iron oxide thin films and consequences for non-local resistance measurements. (in preparation).

[78] Xin Jiang, Li Gao, Jonathan Z. Sun, and Stuart S. P. Parkin. Temperature dependence of current-induced magnetization switching in spin valves with a ferrimagnetic CoGd free layer. *Phys. Rev. Lett.*, 97:217202, Nov 2006.

[79] I A Campbell. Indirect exchange for rare earths in metals. *Journal of Physics F: Metal Physics*, 2(3):L47–L50, may 1972.

[80] P. Hansen, C. Clausen, G. Much, M. Rosenkranz, and K. Witter. Magnetic and magneto-optical properties of rare-earth transition-metal alloys containing Gd, Tb, Fe, Co. *Journal of Applied Physics*, 66(2):756–767, Jul 1989.

[81] L. A. Hernandez, R. W. Greening, M. J. Roos, X. Fan, and B. L. Zink. Temperature controlled anomalous hall voltage switching in co/gd ferrimagnet near compensation. in preparation.

[82] Alex Zevalkink, David M. Smiadak, Jeff L. Blackburn, Andrew J. Ferguson, Michael L. Chabinyc, Olivier Delaire, Jian Wang, Kirill Kovnir, Joshua Martin, Laura T. Schelhas, Taylor D. Sparks, Stephen D. Kang, Maxwell T. Dylla, G. Jeffrey Snyder, Brenden R. Ortiz, and Eric S. Toberer. A practical field guide to thermoelectrics: Fundamentals, synthesis, and characterization. *Applied Physics Reviews*, 5(2):021303, Jun 2018.

[83] Tiejun Zhu, Yintu Liu, Chenguang Fu, Joseph P. Heremans, Jeffrey G. Snyder, and Xinbing Zhao. Compromise and synergy in high-efficiency thermoelectric materials. *Advanced Materials*, 29(14):1605884, Mar 2017.

[84] Joseph P. Heremans, Mildred S. Dresselhaus, Lon E. Bell, and Donald T. Morelli. When thermoelectrics reached the nanoscale. *Nature Nanotechnology*, 8:471–473, 2013.

[85] Terry M. Tritt, Harald Böttner, and Lidong Chen. Thermoelectrics: Direct solar thermal energy conversion. *MRS Bulletin*, 33(4):366–368, Apr 2008.

[86] Terry M. Tritt, Harald Böttner, and Lidong Chen. Thermoelectric materials, phenomena, and applications: A bird's eye view. *MRS Bulletin*, 31(1):188–198, Mar 2006.

[87] Jian He and Terry M. Tritt. Advances in thermoelectric materials research: Looking back and moving forward. *Science*, 357(6358):eaak9997, Sep 2017.

[88] Sahngki Hong, Yue Gu, Joon Kyo Seo, Joseph Wang, Ping Liu, Y. Shirley Meng, Sheng Xu, and Renkun Chen. Wearable thermoelectrics for personalized thermoregulation. *Science Advances*, 5(5):eaaw0536, May 2019.

[89] Francisco Suarez, Amin Nozariasbmarz, Daryoosh Vashaee, and Mehmet C. Öztürk. Designing thermoelectric generators for self-powered wearable electronics. *Energy & Environmental Science*, 9(6):2099–2113, 2016.

[90] Je-Hyeong Bahk, Haiyu Fang, Kazuaki Yazawa, and Ali Shakouri. Flexible thermoelectric materials and device optimization for wearable energy harvesting. *Journal of Materials Chemistry C*, 3(40):10362–10374, 2015.

[91] Sun Jin Kim, Ju Hyung We, and Byung Jin Cho. A wearable thermoelectric generator fabricated on a glass fabric. *Energy & Environmental Science*, 7(6):1959, 2014.

[92] Xue-Kun Chen and Ke-Qiu Chen. Thermal transport of carbon nanomaterials. *Journal of Physics: Condensed Matter*, 32(15):153002, Jan 2020.

[93] Amy M. Marconnet, Matthew A. Panzer, and Kenneth E. Goodson. Thermal conduction phenomena in carbon nanotubes and related nanostructured materials. *Rev. Mod. Phys.*, 85:1295–1326, Aug 2013.

[94] Alexander A. Balandin. Thermal properties of graphene and nanostructured carbon materials. *Nature Materials*, 10(8):569–581, Jul 2011.

[95] Choongho Yu, Li Shi, Zhen Yao, Deyu Li, and Arunava Majumdar. Thermal conductance and thermopower of an individual single-wall carbon nanotube. *Nano Letters*, 5(9):1842–1846, Sep 2005.

[96] Jennifer R. Lukes and Hongliang Zhong. Thermal conductivity of individual single-wall carbon nanotubes. *Journal of Heat Transfer*, 129(6):705–716, Sep 2006.

[97] E. Pop, D. Mann, Q. Wang, K. Goodson, and H. Dai. Thermal conductance of an individual single-wall carbon nanotube above room temperature. *Nano Letters*, 6:96, 2006.

[98] Qingwei Li, Changhong Liu, Xueshen Wang, and Shoushan Fan. Measuring the thermal conductivity of individual carbon nanotubes by the raman shift method. *Nanotechnology*, 20(14):145702, Mar 2009.

[99] Michael T. Pettes and Li Shi. Thermal and structural characterizations of individual single-, double-, and multi-walled carbon nanotubes. *Advanced Functional Materials*, 19(24):3918–3925, Dec 2009.

[100] Alexander A. Balandin, Suchismita Ghosh, Wenzhong Bao, Irene Calizo, Desalegne Teweldebrhan, Feng Miao, and Chun Ning Lau. Superior thermal conductivity of single-layer graphene. *Nano Letters*, 8(3):902–907, 2008.

[101] Yuan Cao, Valla Fatemi, Shiang Fang, Kenji Watanabe, Takashi Taniguchi, Efthimios Kaxiras, and Pablo Jarillo-Herrero. Unconventional superconductivity in magic-angle graphene superlattices. *Nature*, 556(7699):43–50, Mar 2018.

[102] M. S. Dresselhaus and P. C. Eklund. Phonons in carbon nanotubes. *Advances in Physics*, 49(6):705–814, Sep 2000.

[103] Ravi S. Prasher, X. J. Hu, Y. Chalopin, Natalio Mingo, K. Lofgreen, S. Volz, F. Cleri, and Pawel Keblinski. Turning carbon nanotubes from exceptional heat conductors into insulators. *Phys. Rev. Lett.*, 102:105901, Mar 2009.

[104] Yann Chalopin, Sebastian Volz, and Natalio Mingo. Upper bound to the thermal conductivity of carbon nanotube pellets. *Journal of Applied Physics*, 105(8):084301, Apr 2009.

[105] Alexey N. Volkov and Leonid V. Zhigilei. Heat conduction in carbon nanotube materials: Strong effect of intrinsic thermal conductivity of carbon nanotubes. *Applied Physics Letters*, 101(4):043113, Jul 2012.

[106] Jeffrey L. Blackburn, Andrew J. Ferguson, Chungyeon Cho, and Jaime C. Grunlan. Carbon-nanotube-based thermoelectric materials and devices. *Advanced Materials*, 30(11):1704386, Jan 2018.

[107] Nguyen T. Hung, Ahmad R. T. Nugraha, and Riichiro Saito. Thermoelectric properties of carbon nanotubes. *Energies*, 12(23):4561, Nov 2019.

[108] Azure D. Avery, Ben H. Zhou, Jounghee Lee, Eui-Sup Lee, Elisa M. Miller, Rachelle Ihly, Devin Wesenberg, Kevin S. Mistry, Sarah L. Guillot, Barry L. Zink, Yong-Hyun Kim, Jeffrey L. Blackburn, and Andrew J. Ferguson. Tailored semiconducting carbon nanotube networks with enhanced thermoelectric properties. *Nature Energy*, 1(4):16033, Apr 2016.

[109] Bradley A. MacLeod, Noah J. Stanton, Isaac E. Gould, Devin Wesenberg, Rachelle Ihly, Zbyslaw R. Owczarczyk, Katherine E. Hurst, Christopher S. Fewox, Christopher N. Folmar, Katherine Holman Hughes, Barry L. Zink, Jeffrey L. Blackburn, and Andrew J. Ferguson. Large n- and p-type thermoelectric power factors from doped semiconducting single-walled carbon nanotube thin films. *Energy Environ. Sci.*, 10:2168–2179, 2017.

[110] R. Sultan, A. D. Avery, G. Stiehl, and B. L. Zink. Thermal conductivity of micromachined low-stress silicon-nitride beams from $77 - 325$ K. *Journal of Applied Physics*, 105:043501, 2009.

[111] Rubina Sultan, A. D. Avery, J. M. Underwood, S. J. Mason, D. Bassett, and B. L. Zink. Heat transport by long mean free path vibrations in amorphous silicon nitride near room temperature. *Phys. Rev. B*, 87:214305, Jun 2013.

[112] A. D. Avery, S. J. Mason, D. Bassett, D. Wesenberg, and B. L. Zink. Thermal and electrical conductivity of approximately 100-nm permalloy, Ni, Co, Al, and Cu films and examination of the Wiedemann-Franz law. *Phys. Rev. B*, 92:214410, Dec 2015.

[113] S. J. Mason, A. Hojem, D. J. Wesenberg, A. D. Avery, and B. L. Zink. Determining absolute Seebeck coefficients from relative thermopower measurements of thin films and nanostructures. *Journal of Applied Physics*, 127(8):085101, 2020.

[114] Bhupesh Chandra, Ali Afzali, Neeraj Khare, Mostafa M. El-Ashry, and George S. Tulevski. Stable charge-transfer doping of transparent single-walled carbon nanotube films. *Chemistry of Materials*, 22(18):5179–5183, Sep 2010.

[115] Dorothea Scheunemann and Martijn Kemerink. Non-wiedemann-franz behavior of the thermal conductivity of organic semiconductors. *Physical Review B*, 101(7), Feb 2020.

[116] Jun Liu, Xiaojia Wang, Dongyao Li, Nelson E. Coates, Rachel A. Segalman, and David G. Cahill. Thermal conductivity and elastic constants of PEDOT:PSS with high electrical conductivity. *Macromolecules*, 48(3):585–591, Feb 2015.

[117] Annie Weathers, Zia Ullah Khan, Robert Brooke, Drew Evans, Michael T. Pettes, Jens Wenzel Andreasen, Xavier Crispin, and Li Shi. Significant electronic thermal transport in the conducting polymer poly(3,4-ethylenedioxythiophene). *Adv. Mater.*, 27(12):2101–2106, Feb 2015.

[118] G-H. Kim, L. Shao, K. Zhang, and K. P. Pipe. Engineered doping of organic semiconductors for enhanced thermoelectric efficiency. *Nature Materials*, 12(8):719–723, May 2013.

[119] M. B. Salamon, J. W. Bray, G. DePasquali, R. A. Craven, G. Stucky, and A. Schultz. Thermal conductivity of tetrathiafulvalene-tetracyanoquinodimethane (ttf-tcnq) near the metal-insulator transition. *Phys. Rev. B*, 11:619–622, Jan 1975.

[120] Takashi Kodama, Masato Ohnishi, Woosung Park, Takuma Shiga, Joonsuk Park, Takashi Shimada, Hisanori Shinohara, Junichiro Shiomi, and Kenneth E. Goodson. Modulation of thermal and thermoelectric transport in individual carbon nanotubes by fullerene encapsulation. *Nature Materials*, 16(9):892–897, Jul 2017.

[121] Kumar Varoon Agrawal, Steven Shimizu, Lee W. Drahushuk, Daniel Kilcoyne, and Michael S. Strano. Observation of extreme phase transition temperatures of water confined inside isolated carbon nanotubes. *Nature Nanotechnology*, 12(3):267–273, Nov 2016.

[122] Jeffrey L. Blackburn, Stephen D. Kang, Michael J. Roos, Brenna Norton-Baker, Elisa M. Miller, and Andrew J. Ferguson. Intrinsic and extrinsically limited thermoelectric transport within semiconducting single-walled carbon nanotube networks. *Advanced Electronic Materials*, 5(11):1800910, Feb 2019.

[123] Brenna Norton-Baker, Rachelle Ihly, Isaac E. Gould, Azure D. Avery, Zbyslaw R. Owczarczyk, Andrew J. Ferguson, and Jeffrey L. Blackburn. Polymer-free carbon nanotube thermoelectrics with improved charge carrier transport and power factor. *ACS Energy Letters*, 1(6):1212–1220, Nov 2016.

[124] Yusuke Nakai, Kazuya Honda, Kazuhiro Yanagi, Hiromichi Kataura, Teppei Kato, Takahiro Yamamoto, and Yutaka Maniwa. Giant Seebeck coefficient in semiconducting single-wall carbon nanotube film. *Applied Physics Express*, 7(2):025103, 2014.

[125] W. Zhou, J. Vavro, N. M. Nemes, J. E. Fischer, F. Borondics, K. Kamarás, and D. B. Tanner. Charge transfer and fermi level shift in *p*-doped single-walled carbon nanotubes. *Phys. Rev. B*, 71:205423, May 2005.

[126] J. Vavro, M. C. Llaguno, J. E. Fischer, S. Ramesh, R. K. Saini, L. M. Ericson, V. A. Davis, R. H. Hauge, M. Pasquali, and R. E. Smalley. Thermoelectric power of *p*-doped single-wall carbon nanotubes and the role of phonon drag. *Phys. Rev. Lett.*, 90:065503, Feb 2003.

[127] Daisuke Hayashi, Yusuke Nakai, Haruka Kyakuno, Yasumitsu Miyata, Kazuhiro Yanagi, and Yutaka Maniwa. Temperature dependence of the seebeck coefficient for mixed semiconducting and metallic single-wall carbon nanotube bundles. *Applied Physics Express*, 13(1):015001, Nov 2019.

[128] M. Tsaousidou. Theory of phonon-drag thermopower of extrinsic semiconducting single-wall carbon nanotubes and comparison with previous experimental data. *Physical Review B*, 81(23), Jun 2010.

[129] M. Tsaousidou. Phonon-drag thermopower of ballistic semiconducting single-wall carbon nanotubes and comparison with the semiclassical result. *EPL (Europhysics Letters)*, 93(4):47010, Feb 2011.

[130] Margarita Tsaousidou. Enhanced phonon-drag thermopower of ballistic semiconducting single-walled carbon nanotubes near the second subband edge. *physica status solidi (b)*, 256(6):1800757, Apr 2019.

[131] Devin J. Wesenberg, Michael J. Roos, Azure D. Avery, Jeffrey L. Blackburn, Andrew J. Ferguson, and Barry L. Zink. Size- and temperature-dependent suppression of phonon thermal conductivity in carbon nanotube thermoelectric films. *Advanced Electronic Materials*, 6(11):2000746, Oct 2020.

[132] Shunsuke Sakurai, Fuminori Kamada, Don N Futaba, Motoo Yumura, and Kenji Hata. Influence of lengths of millimeter-scale single-walled carbon

nanotube on electrical and mechanical properties of buckypaper. *Nanoscale Research Letters*, 8(1), dec 2013.

[133] Hanliang Zhu, Zdenka Fohlerová, Jan Pekárek, Evgenia Basova, and Pavel Neužil. Recent advances in lab-on-a-chip technologies for viral diagnosis. *Biosensors and Bioelectronics*, 153:112041, Apr 2020.

[134] Jianjian Zhuang, Juxin Yin, Shaowu Lv, Ben Wang, and Ying Mu. Advanced "lab-on-a-chip" to detect viruses – current challenges and future perspectives. *Biosensors and Bioelectronics*, 163:112291, Sep 2020.

[135] Yi Sun, Raghuram Dhumpa, Dang Duong Bang, Jonas Høgberg, Kurt Handberg, and Anders Wolff. A lab-on-a-chip device for rapid identification of avian influenza viral RNA by solid-phase PCR. *Lab on a Chip*, 11(8):1457, 2011.

[136] Jinhye Bae, Juanjuan Zheng, Haitao Zhang, Peter J. Foster, Daniel J. Needleman, and Joost J. Vlassak. A micromachined picocalorimeter sensor for liquid samples with application to chemical reactions and biochemistry. *Advanced Science*, 8(5):2003415, Jan 2021.

[137] Sunghoon Hur, Rohith Mittapally, Swathi Yadlapalli, Pramod Reddy, and Edgar Meyhofer. Sub-nanowatt resolution direct calorimetry for probing

real-time metabolic activity of individual c. elegans worms. *Nature Communications*, 11(1), Jun 2020.

[138] B. Revaz, B. L. Zink, and F. Hellman. Si-N membrane-based microcalorimetry: heat capacity and thermal conductivity of thin films. *Thermochimica Acta*, 432:158–168, 2005.

[139] Rubina Sultan, B. L. Zink, K. D. Irwin, G. C. Hilton, J. N. Ullom, and L. R. Vale. Design, fabrication, and multiplexing of magnetic calorimeter x-ray detectors with high-efficiency squid readout. *Journal of Low Temperature Physics*, 151(1-2):363–368, 2008.

[140] B. L. Zink, R. Pietri, and F. Hellman. Specific heat and thermal conductivity of thin-film amorphous silicon. *Physical Review Letters*, 96:055902, 2006.

[141] A. Cassedy, A. Parle-McDermott, and R. O'Kennedy. Virus detection: A review of the current and emerging molecular and immunological methods. *Frontiers in Molecular Biosciences*, 8, apr 2021.

[142] Caroline Kilbourne Stahle, Dan McCammon, and Kent D. Irwin. Quantum calorimetry. *Physics Today*, 52(8):32–37, Aug 1999.

[143] Kelsey M. Morgan. Hot science with cool sensors. *Physics Today*, 71(8):28–34, Aug 2018.

[144] Bayan Karimi, Fredrik Brange, Peter Samuelsson, and Jukka P. Pekola. Reaching the ultimate energy resolution of a quantum detector. *Nature Communications*, 11(1), Jan 2020.

[145] M. R. Natale, D. J. Wesenberg, Eric R. J. Edwards, Hans T. Nembach, Justin M. Shaw, and B. L. Zink. Field-dependent nonelectronic contributions to thermal conductivity in a metallic ferromagnet with low Gilbert damping. *Phys. Rev. Materials*, 5:L111401, Nov 2021.

[146] S. J. Mason, D. J. Wesenberg, A. Hojem, M. Manno, C. Leighton, and B. L. Zink. Violation of the Wiedemann-Franz law through reduction of thermal conductivity in gold thin films. *Phys. Rev. Materials*, 4:065003, Jun 2020.

[147] A. D. Avery, M. R. Pufall, and B. L. Zink. Predicting the planar Nernst effect from magnetic-field-dependent thermopower and resistance in nickel and permalloy thin films. *Physical Review B*, 86:184408, 2012.

[148] A. D. Avery and B. L. Zink. Peltier cooling and Onsager reciprocity in ferromagnetic thin films. *Phys. Rev. Lett.*, 111:126602, Sep 2013.

[149] S. van Engelenburg. Private Communication.

[150] P. Sullivan and G. Seidel. *Phys. Rev.*, 173:679, 1968.

[151] R Bachmann, F. J. DiSalvo Jr., T. H. Geballe, R. L. Green, R. E. Howard, C. N. King, H. C. Kirsch, K. N. Lee, R. E. Schwall, H. U. Thomas, and R. B.

Zubeck. Heat capacity measurements on small samples at low temperatures. *Review of Scientific Instruments*, 43:205, 1972.

[152] D. W. Denlinger, E. N. Abarra, Kimberly Allen, P. W. Rooney, M. T. Messer, S. K. Watson, and F. Hellman. Thin-film microcalorimeter for heat-capacity measurements from 1.5 K to 800 K. *Review of Scientific Instruments*, 65:946, 1994.

[153] D. R. Queen and F. Hellman. Thin film nanocalorimeter for heat capacity measurements of 30 nm films. *Review of Scientific Instruments*, 80(6):063901, 2009.

[154] Material properties: Ofhc copper (uns c10100/c10200). https://trc.nist.gov/cryogenics/materials/OFHC

[155] J. M. Ziman. *Electrons and phonons : the theory of transport phenomena in solids.* Clarendon Press., Oxford, 1960.

[156] Prem Nath and K.L. Chopra. Thermal conductivity of copper films. *Thin Solid Films*, 20(1):53 – 62, 1974.

[157] R. Sultan. PhD thesis, University of Denver, 2010.

[158] A. D. Avery. *Thermal and Electrical Transport in Ferromagnetic Metal Thin Films*. PhD thesis, University of Denver, 2013.

[159] S. J. Mason. *Nanoscale Thermoelectrics: A Study of the Absolute Seebeck Coefficient of Thin Films*. PhD thesis, University of Denver, 2014.

[160] D. J. Wesenberg. PhD thesis, University of Denver, 2018.

[161] Noah de Leeuw. Matlab support.

Appendix A: Thermal Isolation Platform Fabrication and Technique

While the thermal isolation platform measurement technique and fabrication process is described in detail elsewhere [157–160] a brief overview is nonetheless provided here for referencing. As shown in Fig. 6.4, power P_{J} is dissipated through Joule heating in the resistive heating element of one island. Heat flows down the bridge between islands and legs connecting the islands to chip frame. The rate of heat from each island can be written as

$$C_{\mathrm{H}}\frac{\partial T_{\mathrm{H}}}{\partial t} = P_{\mathrm{J}} - K_{\mathrm{B}}(T_{\mathrm{H}} - T_{\mathrm{C}}) - K_{\mathrm{L}}(T_{\mathrm{H}} - T_0) \tag{A.1}$$

$$C_{\mathrm{C}}\frac{\partial T_{\mathrm{H}}}{\partial t} = P_{\mathrm{C}} - K_{\mathrm{B}}(T_{\mathrm{C}} - T_{\mathrm{H}}) - K_{\mathrm{L}}(T_{\mathrm{C}} - T_0) \tag{A.2}$$

where $C_{\mathrm{H/C}}$, $T_{\mathrm{H/C}}$, and $P_{\mathrm{J/C}}$, are the heat capacity, temperature, and power dissipated for the 'hot' and 'cold' islands, $K_{\mathrm{B/L}}$ are thermal conductances of the bridge and legs, and T_0 is the temperature of the chip frame acting as the system's thermal energy reservoir. After island temperatures reach equilibrium, the time-dependent components and cold island power terms can be set to zero:

$$0 = P_{\mathrm{J}} - K_{\mathrm{B}}(T_{\mathrm{H}} - T_{\mathrm{C}}) - K_{\mathrm{L}}(T_{\mathrm{H}} - T_0) \tag{A.3}$$

$$0 = -K_{\mathrm{B}}(T_{\mathrm{C}} - T_{\mathrm{H}}) - K_{\mathrm{L}}(T_{\mathrm{C}} - T_0) \tag{A.4}$$

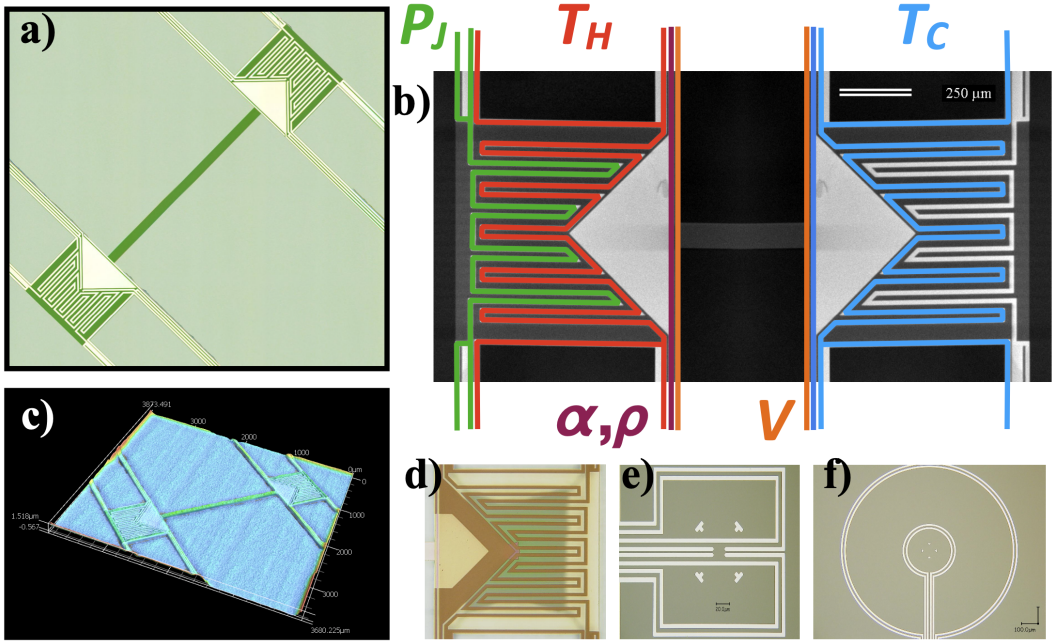

Figure A.1: **a)** Suspended Si-N thermal isolation platform during fabrication, after metal liftoff and before acid etching. A small break in thermometer lead in the center of each island will be used to deposit amorphous platinum for low temperature thermometry. **b)** Thermal leads showing locations of P_J, T_H, and T_C. T_0 is located on the surrounding chip frame. Connecting leads for *in-situ* 4-wire electric, thermoelectric, or spintronic measurements are α, ρ, and V. A few examples of platforms and patterned leads included **c)** an optical profile standard chip, **d)** electrically passivated islands showing an incomplete Si under-layer wet etch and island suspension, and **e,f)** non-local spin transport measurement geometries.

This system of equations can then be reduced to the set of linear equations

$$T_H = T_0 + \frac{K_B + K_L}{(2K_B + K_L)K_L} P_J \tag{A.5}$$

$$T_C = T_0 + \frac{K_B}{(2K_B + K_L)K_L} P_J \tag{A.6}$$

A series of increasing P_J is applied to the hot island thermistor, at which each T_H, T_C, and T_0 resistance values are taken by the SRS AC Resistance Bridge, and indi-

vidually calibrated to temperature for each experiment. Equations A.5 and A.6 are fit to the resulting T_H vs. P_J and T_C vs. P_J plots at every base temperature. K_L and K_L are then calculated by the slopes of the fits.

Appendix B: Heat Capacity Matlab Code

For time-dependent measurements done by filling the Keithley 2181a Nanovoltmeter buffer, special care is necessary when analysing large data sets. One temperature dependent heat capacity measurement might have tens of thousands of individual timestamped data. Measurements on one thermometer at one temperature may have small deviations in the length of data taken, starting points, or offsets. The following Matlab code takes the raw comma-separated data file, and outputs a cleaned file where every individual data set has been adjusted to one uniform format. [161] A second file is output that takes the resistance values and shifts them to a ΔR relaxing to zero.

Matlab Code: Formatting Heat Capacity Raw Data.

```
function [] = heatCapZeroOff();
% Discretizes Heat Capacity Data

% Import csv file
fname = uigetfile('*.csv');
fdat = csvread(fname);

% Delete bad values
fbad = find(fdat(:,1) ~= fdat(:,4));
fdat2 = fdat;
fdat2(fbad,:) = [];

funique = unique(fdat2(:,1));
for nn = 1:length(funique)
    fcount(nn,1) = nnz(fdat2(:,1)==funique(nn));
end
fmin = min(fcount);

% Delete too long entries
for nn = 1:length(fcount)
    if fcount(nn) > fmin
```

```
            ftemp = fdat2(:,1) == funique(nn);
            ftemp2 = fdat2(ftemp,:);
            ftemp3 = ftemp2((fmin+1):fcount(nn),:);
            [~,b,~] = intersect(fdat2,ftemp3,'rows');
            if exist('fbad2') ~= 1
                fbad2 = b;
            else
                fbad2(end+1,1) = b;
            end
        end
    end

    fdat3 = fdat2;
    fdat3(fbad2,:) = [];

    funique = unique(fdat3(:,1));
    for nn = 1:length(funique)
        fcount(nn,1) = nnz(fdat3(:,1)==funique(nn));
    end

    % Offset resistance values
    fdat4 = fdat3;
    for nn = 1:length(funique)
        ftemp = fdat4(:,1) == funique(nn);
        ftemp2 = fdat4(ftemp,:);
        ftemp2(:,2) = ftemp2(:,2) - min(ftemp2(:,2));
        ftemp2(:,5) = ftemp2(:,5) - min(ftemp2(:,5));
        fdat4(ftemp,:) = ftemp2;
    end

    % Save new csv files
    csvwrite(['final_',fname],fdat3);
    csvwrite(['final_zeroOff_',fname],fdat4);
    end
```